

©[2012]

Nara Lee

ALL RIGHTS RESERVED

**Strong Interplay between Ferroelectric and Magnetic Orders in Novel Complex  
Oxides**

by

Nara Lee

A Dissertation submitted to the  
Graduate School-New Brunswick  
Rutgers, The State University of New Jersey  
in partial fulfillment of the requirements

for the degree of

Doctor of Philosophy

Graduate Program in Physics

written under the direction of

Professor Sang-Wook Cheong

and approved by

---

---

---

---

---

New Brunswick, New Jersey

May, 2012

## **Abstract of the Dissertation**

Strong Interplay between Ferroelectric and Magnetic Orders in Novel Complex Oxides

by

Nara Lee

Dissertation Director :

Sang-Wook Cheong

Multiferroics, where ferroelectric and magnetic orders are concurrently present, reveal new physical properties due to the strong interplay between the dual order parameters. The emergence of the unprecedented cross-coupling effects in such materials has offered a new vein of essential understanding of correlated spin and lattice degrees of freedom and the related macroscopic phenomena, and has invigorated the application in future generations of novel devices. Recently, the enhanced coupling has been discovered in the new class of materials called spin-driven ferroelectrics in which ferroelectric order originates from the exchange striction of special types of magnetic orders with broken inversion symmetry. However, the driven ferroelectric polarization appears to be minuscule, compared with that of the typical ferroelectrics. Thus, one of the demanding challenges of the multiferroics research is finding systems or ways to escalate the magnitude of polarization. Herein, we present discoveries of new multiferroics which exhibit giant ferroelectricity due to the new exchange striction mechanism through rare-earth and transition-metal ions and their strong tunability of polarization by applying magnetic fields. (1) New multiferroic of single-crystalline orthorhombic  $\text{HoMnO}_3$  was, for the first time, grown by the flux method. The crystals with incommensurate E-type magnetic structure exhibit much large ferroelectric polarization with the direction along the  $c$ -axis, completely different from the

theoretical predictions. From the analysis, the polarization can be described by the new emerging mechanism of Ho-Mn exchange striction. (3) Tunable giant ferroelectric polarization in the multiferroic  $\text{GdMn}_2\text{O}_5$  has been demonstrated. The ferroelectric polarization in this compound is found to be the largest and be varied repeatedly with the largest change by applying external magnetic fields among the spin-driven ferroelectrics known to date. In addition, contrary to the known origin for ferroelectricity in  $\text{REMn}_2\text{O}_5$  (RE=rare earth ions), the Mn-Mn exchange striction mechanism, the complete magnetic structure constructed by the x-ray resonant scattering experiment clarify that the giant ferroelectricity in  $\text{GdMn}_2\text{O}_5$  results mainly from the Gd-Mn symmetric exchange striction.



## **Acknowledgements**

First of all, I thank God for guiding me throughout my entire life and showing me his will all the time. Professor Sang-Wook Cheong deserves my deepest appreciation for opening and broadening my views to research. He taught me how to enjoy my work, especially synthesizing new materials. I also appreciate Professor Weida Wu and Valery Kiryukhin for their kind advice and useful discussion. I have met lots of great colleagues whom I have worked with and interacted with during my Ph.D. I acknowledge Seungchul Chae, Yoon Seok Oh, Xueyun Wang, Bin Gao, Andrew Hogan, Yoichi Horibe and Hee Taek Yi for their warm support and help to get through difficult times. I also give my special thanks to passionate undergraduate students: Daniel Kwok, Sean Fackler, Matthew Vannucci, Abdullah Sandhu, Gary A. Kapilevich, Steven Rodan and Pranav Gupta. My sincere gratitude goes to my Ph.D. committee members: Professor Jane Hinch, Sean Oh, Emil Yuzbashyan and Andrei Sirenko for following my work during my research and valuable advice.

Finally, I express my appreciation to my parents and parents-in-law who always support my decision and pray for me. I gratefully acknowledge my sister and sister-in-law (and my future nephew). And most of all, I would like to thank my husband, Young Jai Choi who completes me. Everything I accomplished has no meaning without him.

## TABLE OF CONTENTS

Abstract of the Dissertation.....	ii
Acknowledgements.....	iv
Table of Contents.....	v
I. Latest Progress in Multiferroics Research.....	1
1. Introduction to Multiferroics.....	2
2. Antisymmetric Exchange Interaction–Spiral-magnetic Multiferroics....	3
3. Symmetric Exchange Interaction – Collinear-magnetic Multiferroics ....	7
4. Cross-control of Magnetization and Polarization by Applying Electric and Magnetic Fields .....	10
5. Imaging Multiferroic Vortices .....	15
6. REFERENCES.....	20
II. New exchange-striction mechanism of ferroelectricity in multiferroic orthorhombic $\text{HoMnO}_3$ .....	22
1. Introduction.....	23
2. Experimental Method.....	25
3. Result and Discussion.....	28
4. REFERENCES.....	40
III. Tunable Large Ferroelectric Polarization in a Magnetism-Driven Ferroelectric...	42
1. Introduction.....	43
2. Experimental Method.....	45
3. Result and Discussion.....	47

4. REFERENCES.....	60
V. Conclusion.....	61
Appendix I: Cross-Control of Magnetization and Polarization by Electric and Magnetic Fields with Competing Multiferroic and Weak-Ferromagnetic Phase ( <i>Phys. Rev. Lett.</i> , 2010).....	71
Appendix II: Mechanism of exchange striction of ferroelectricity in multiferroic orthorhombic HoMnO <sub>3</sub> single crystal ( <i>Phys. Rev. B, Rapid Communication</i> , 2011).....	75
Appendix III: Direct observation of the proliferation of ferroelectric dislocation loops and vortex-antivortex pairs ( <i>Submitted to Phys. Rev. Lett.</i> ).....	79
Appendix IV: Collective Magnetism at ferroelectric vortex domain walls ( <i>Submitted</i> )....	95
Appendix V: Magnetochromism in hematite : chamelonic rust ( <i>Submitted to Phys. Rev. Lett.</i> ).....	105
Curriculum Vitae.....	119

## **Chapter I**

### **Latest Progress in Multiferroics Research**

## 1. Introduction to Multiferroics

Ferroelectric and magnetic materials have been a time-honored subject of research and have led to some of the most important technological advances to date. Magnetism and ferroelectricity are involved with local spins and off-centered structural distortions, respectively. These two seemingly unrelated phenomena can indeed coexist in certain unusual materials, termed multiferroics, in which astonishing effects due to the cross-coupling between magnetic and dielectric properties have been recently observed [1, 2]. However, the understanding of this remarkable occurrence remains a scientific challenge. Among the several multiferroics newly-discovered in the past few years, a new class of multiferroics, where magnetic order itself generates ferroelectricity, has been of great recent interest. In these magnetism-driven ferroelectrics, magnetic order accompanied by the loss of inversion symmetry loses the lattice inversion symmetry through exchange striction, thus inducing ferroelectricity [3-10]. Moreover, external magnetic field which influences the spin configurations of magnetic order naturally results in changes in ferroelectric or dielectric properties. Highly tunable electric properties by applied magnetic fields have been observed in many materials categorized as this class [3-5]. The representative examples can be listed as  $\text{REMnO}_3$  (RE=rare earth ions),  $\text{REMn}_2\text{O}_5$ , orthorhombic  $\text{REMnO}_3$ , orthoferrites  $\text{REFeO}_3$ , langasite  $\text{Ba}_3\text{NbFe}_3\text{Si}_2\text{O}_{14}$ ,  $\text{LiCu}_2\text{O}_2$ ,  $\text{Ca}_3\text{CoMnO}_6$ , double perovskite  $\text{RE}_2\text{CoMnO}_6$ , delafossite  $\text{CuFeO}_2$ ,  $\text{ACrO}_2$  (A=Cu, Ag), and  $\text{CaMn}_7\text{O}_{12}$  [1-9]. The origin of the ferroelectricity turns out to be exchange **striction** possibly due to both symmetric and anti-symmetric parts of exchange couplings of

specific spin configurations. The anti-symmetric exchange coupling known as the Dzyaloshinski-Moriya (DM) interaction is activated for ferroelectricity in spiral-magnetic systems such as  $\text{TbMnO}_3$  and  $\text{LiCu}_2\text{O}_2$  [1, 5], while the symmetric exchange interaction is responsible for the multiferroicity in the collinear-magnetic systems such as  $\text{Ca}_3\text{CoMnO}_6$  and  $\text{TbMn}_2\text{O}_5$  [2, 6]. Due to the intrinsic magnetoelectric coupling in such materials, effective control of bulk magnetization by applied electric fields would be expected as well. However, the evidence for tunable bulk magnetization by electric fields has scarcely been presented so far [11].

Another interesting aspect of multiferroics is the observation of multiferroic domain and domain-wall structures. In multiferroic  $\text{h-REMnO}_3$ , an intriguing ‘cloverleaf’-like pattern which is composed of six ferroelectric domains merging at one point was observed. This pattern forms a vortex or an anti-vortex depending on the order of rotation of six domains and originates from a topological defect with interlocked ferroelectric and structural antiphase domain walls. The patterns appear to distribute over the crystal creating a complicated vortex-antivortex network [10, 11]. Moreover, very recently, an MFM (Magnetic Force Microscopy) study of  $\text{h-ErMnO}_3$  reveals that magnetic domains at low temperature follow the same cloverleaf-like patterns, thus proves that the patterns are the true multiferroic vortices and anti-vortices, i.e., magnetic-ferroelectric domains [12].

## **2. Antisymmetric Exchange Interaction – Spiral-magnetic Multiferroics**

The most common origin for magnetically-driven ferroelectrics is found in spiral-magnets where spins rotate while propagating perpendicular to the spin rotation axis (FIG. I. 1). The mechanism of ferroelectricity is known to be the antisymmetric exchange striction due to inverse effect of the Dzyaloshinskii–Moriya (DM) interaction among the non-collinear-type spin configuration [13]. A spiral-magnetic order can be stabilized in a typical condition that the ratio between  $J_{AF}$  and  $J_F$  is larger than 1/4, i.e.,  $|J_{AF}/J_F| > 1/4$  where nearest-neighbor ferromagnetic coupling ( $J_F$ ) and next-nearest-neighbor antiferromagnetic coupling ( $J_{AF}$ ) compete each other. Then every nearest-neighbor spin pair in the spiral modulation produces the same displacement of the mediated oxygen ion because of the inverse DM interaction, leading to the ferroelectric polarization with the direction perpendicular to the spin modulation vector. The so-called spin current model presents that the induced ferroelectric polarization is proportional to  $e_{ij} \times (S_i \times S_j)$ , where  $S_i$  and  $S_j$  are neighboring two magnetic spins and  $e_{ij}$  is the vector connecting the two spins.

An outstanding realization of a spiral magnet with ferroelectricity and pronounced magneto-electric coupling occurs in the one-dimensional quantum magnet of cuprate  $\text{LiCu}_2\text{O}_2$ . Note that cuprates have been known to exhibit various extraordinary quantum effects such as high- $T_c$  superconductivity and the Haldane state, and this discovery supplies the first example of a ferroelectric cuprate. In,  $\text{LiCu}_2\text{O}_2$ , the ferroelectric polarization along the  $c$ -axis emerges at the temperature where the spiral magnetic order sets in (FIG. I. 2(b)) [5]. With the application of magnetic field along the  $b$ -axis, the ferroelectric polarization flops to the  $a$ -axis because the spiral plane rotates from the  $bc$  to  $ab$  plane by  $90^\circ$  as represented in FIG. I. 2 (b) and (c).

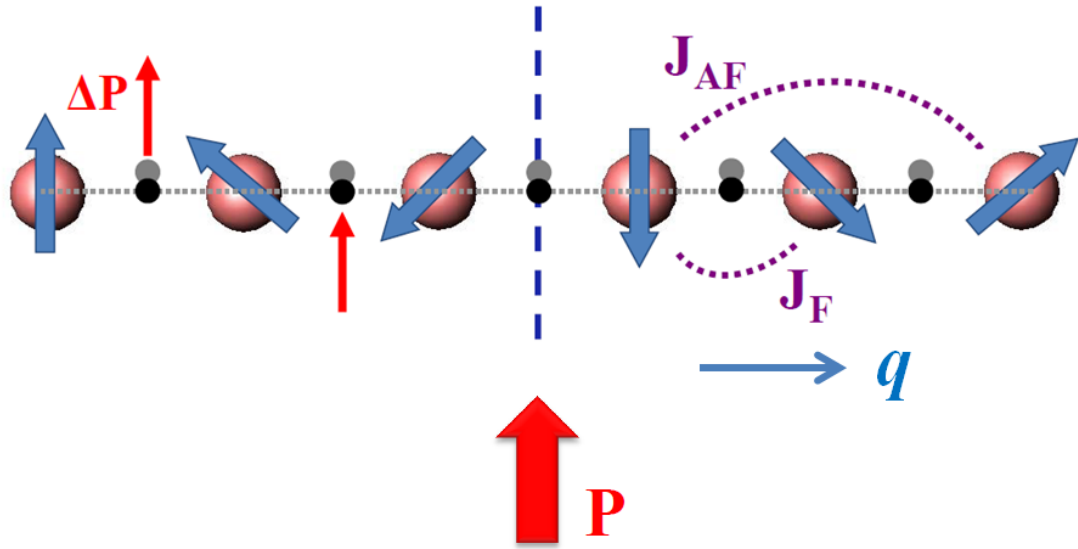


FIG. I. 1. The spiral spin structure. The mirror-plane (indicated by the blue dotted line) symmetry is lost generating the ferroelectric polarization along the direction perpendicular to the spiral modulation vector.



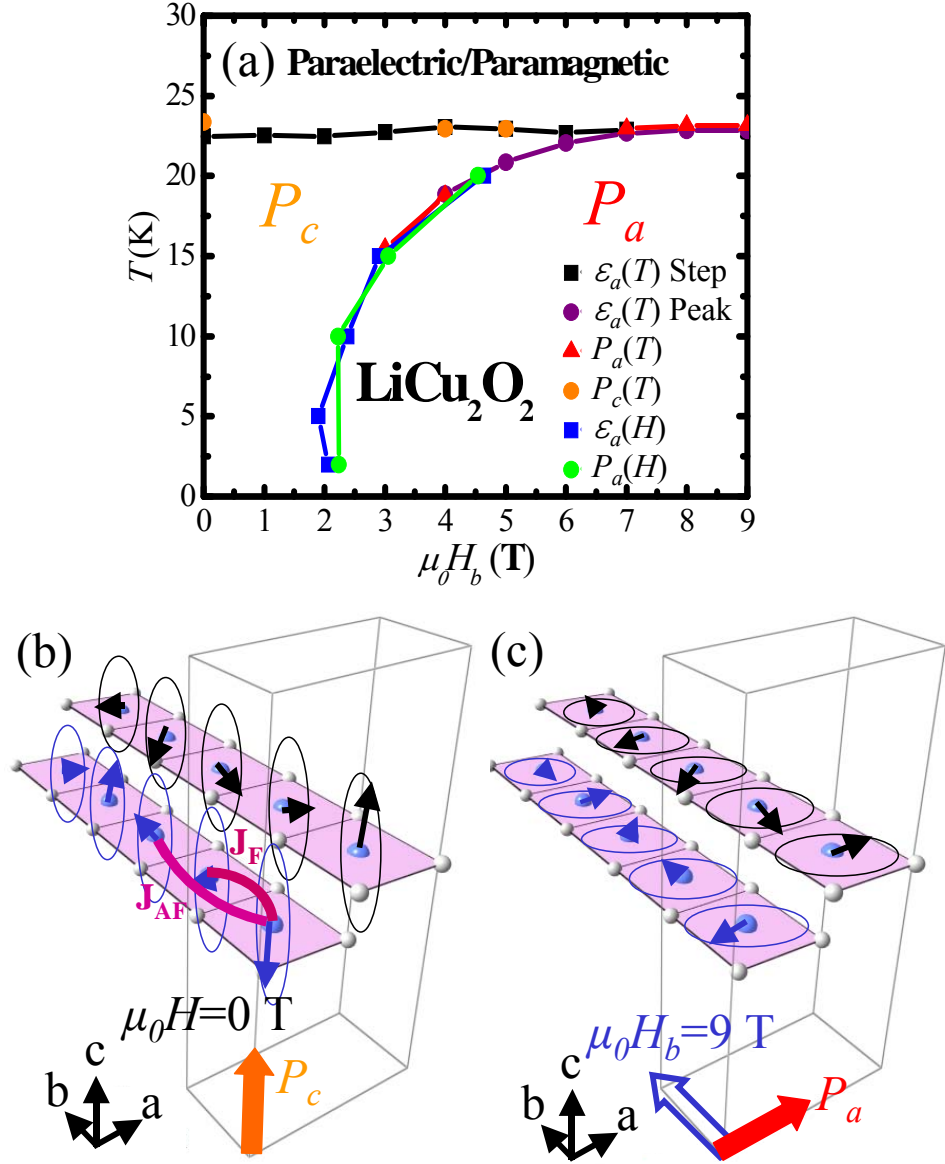


FIG. 1. 2. (a) Phase diagram of  $\text{LiCu}_2\text{O}_2$ , showing the presence of a paraelectric – paramagnetic state, a ferroelectric state with  $P_c$  and a ferroelectric state with  $P_a$  induced by  $H_b$ . (b) Proposed spiral spin structure in zero magnetic field, consistent with the presence of a finite electric polarization ( $P$ ) along the  $c$ -axis.  $\text{Cu}^{2+}$  ions (in blue) are coordinated by five oxygen atoms (in white) including one apical one. (c) Proposed spiral spin structure in  $H = 9 \text{ T}$  along the  $b$ -axis. In  $H_b$ ,  $P$  switches to the  $a$ -axis [5].

### 3. Symmetric Exchange Interaction – Collinear-magnetic Multiferroics

The other mechanism for spin-driven ferroelectricity is through symmetric exchange interaction. In an Ising chain magnet,  $\text{Ca}_3\text{CoMnO}_6$ , competition between nearest neighbor ferromagnetic ( $J_F$ ) and next-nearest-neighbor antiferromagnetic interactions ( $J_{AF}$ ) produces up-up-down-down ( $\uparrow\uparrow\downarrow\downarrow$ )-type spin order for  $|J_{AF}/J_F| > 1/2$  as shown in FIG. I. 3. If the charges of magnetic ions alternate along the chain, the system loses inversion symmetry resulting in ferroelectricity [6].

The routes to exchange interactions are a bit more complicated in orthorhombic  $\text{REMn}_2\text{O}_5$  (RE=rare earth ions, Tb-Lu). In  $\text{REMn}_2\text{O}_5$ ,  $\text{Mn}^{4+}$  ions occupy oxygen octahedra, whereas  $\text{Mn}^{3+}$  ions are in oxygen square-pyramids as shown in FIG. I. 4. These ions form zigzag antiferromagnetic chain modulating along the  $a$ -axis with the spins parallel within each chain and tilted by about  $15^\circ$  with respect to the  $a$  axis below commensurate antiferromagnetic ordering temperature. The electric polarization results from the symmetric exchange striction among nearly collinear Mn spins. The exchange striction is dominated by the spin-configuration of neighboring  $\text{Mn}^{3+}$ - $\text{Mn}^{4+}$  pair and generates an ionic ferroelectric polarization along the  $b$ -axis whose sign is dictated by the repulsion and attraction of pairs of ions bearing anti-parallel and parallel spin configurations, respectively [14]. More detailed explanation on the system will be discussed in Chapter 2.

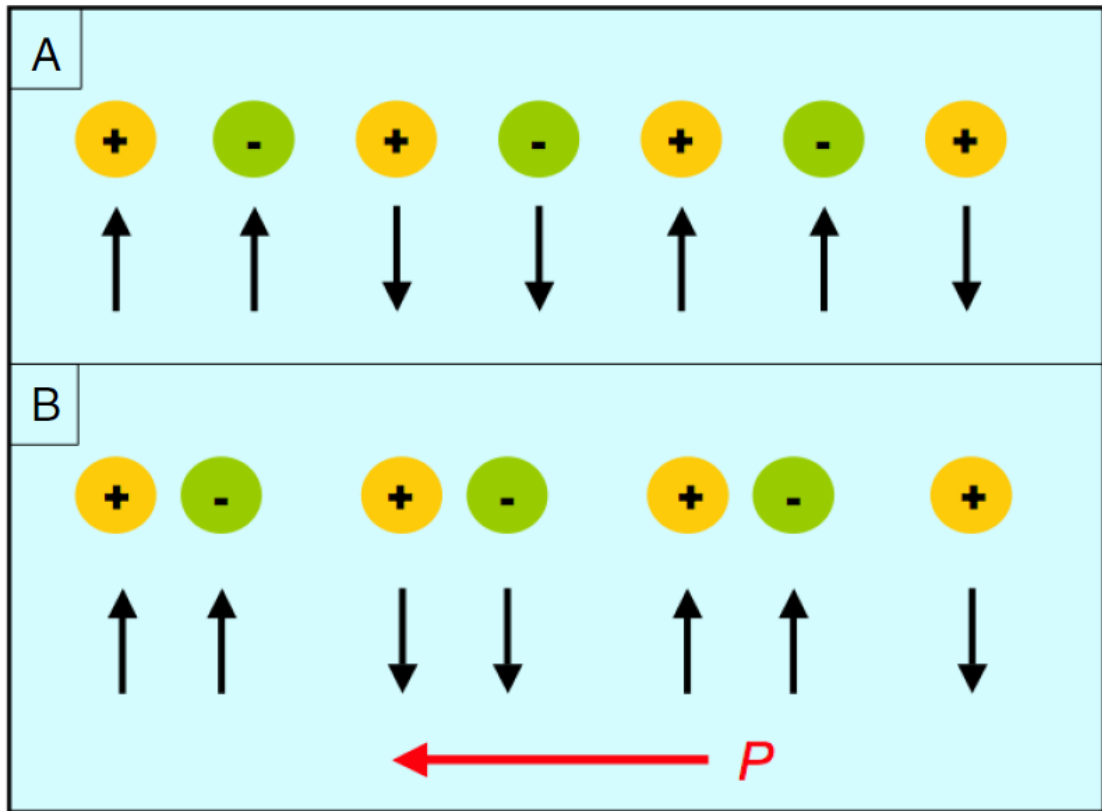


FIG. I. 3. (a) 1-dimensional chain with alternating charges and  $\uparrow\uparrow\downarrow\downarrow$ -type spin order. (b) Effect of exchange striction resulting in the displacements of ions and thus producing ferroelectric polarization (red arrow) [15].

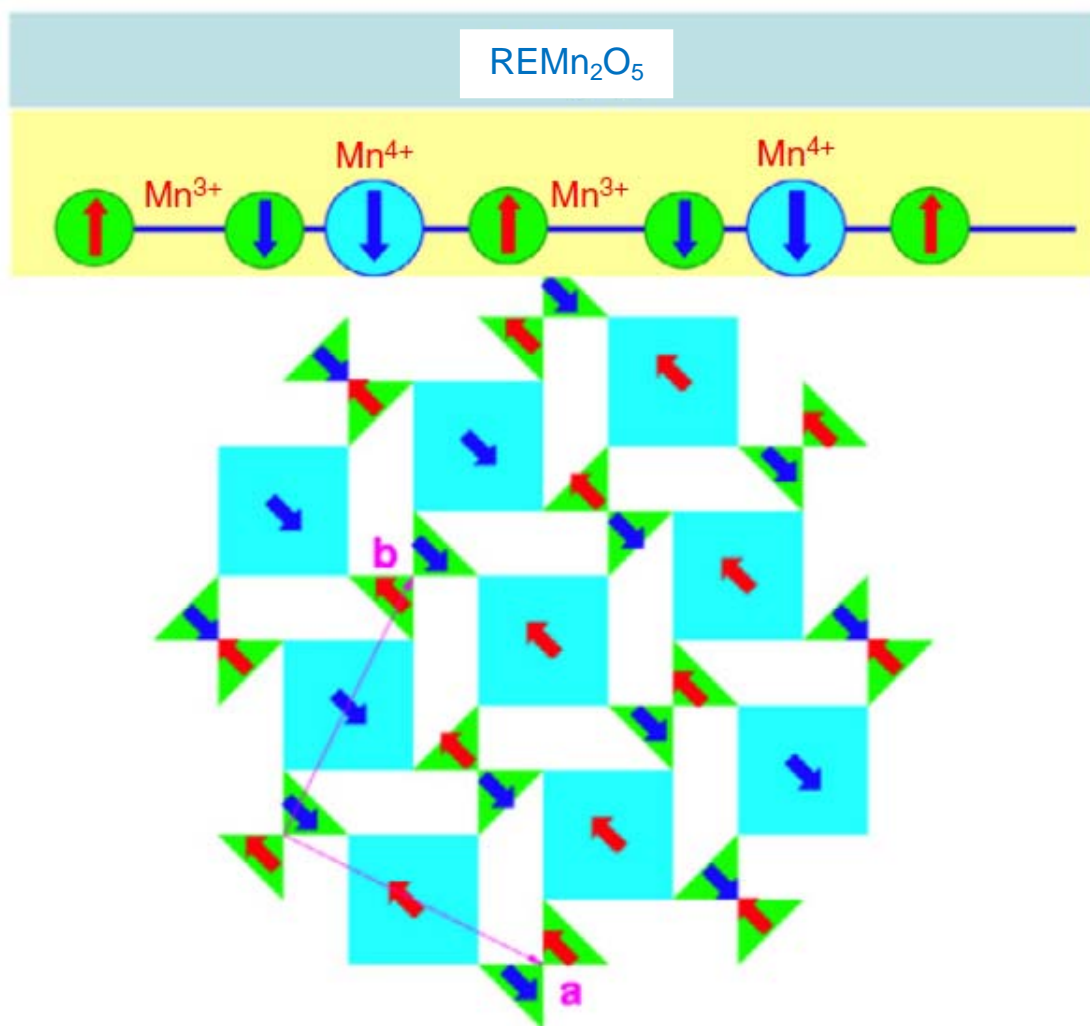


FIG. I. 4. Schematic view of the structure of  $\text{RE}\text{Mn}_2\text{O}_5$ . Blue squares and green triangles indicate  $\text{Mn}^{4+}\text{O}_6$  octahedra and  $\text{Mn}^{3+}\text{O}_5$  bypyramids, respectively [15].

E-type antiferromagnetic orthorhombic  $\text{REMnO}_3$  (o- $\text{REMnO}_3$ ) is also a multiferroic whose ferroelectric polarization is induced by symmetric exchange striction [16, 17]. o- $\text{REMnO}_3$  with small rare earth ions such as Ho and Y crystallizes in a distorted perovskite structure. The ferroelectricity in the E-type manganites is currently believed to be induced mainly by Mn-Mn symmetric exchange striction, i.e. repulsion of co-aligned Mn spins. This repulsion, together with the associated motion of the oxygen ions, leads to the appearance of ferroelectric polarization along the  $a$ -axis for the commensurate state, as illustrated in FIG. I. 5. Note that the theoretical estimation predicted that the ferroelectric polarization through symmetric exchange striction in E-type spin order can be larger than that in spiral magnets by up to two orders of magnitude [16].

#### **4. Cross-control of Magnetization and Polarization by Applying Electric and Magnetic Fields**

Controlling magnetism by an external electric field or ferroelectric polarization by applying magnetic field has been an important topic in multiferroic research. In a magnetism-driven ferroelectrics such as  $\text{REMn}_2\text{O}_5$ , application of sufficient magnetic field can bring drastic changes in ferroelectric and dielectric properties i.e. large magnetoelectric effects [2, 18]. FIG. 1.6.(c) demonstrates the highly reversible  $180^\circ$  flipping of electric polarization along the  $b$ -axis in  $\text{TbMn}_2\text{O}_5$  upon applying magnetic field along the  $a$ -axis. However, the demonstration of tunable magnetization by applying

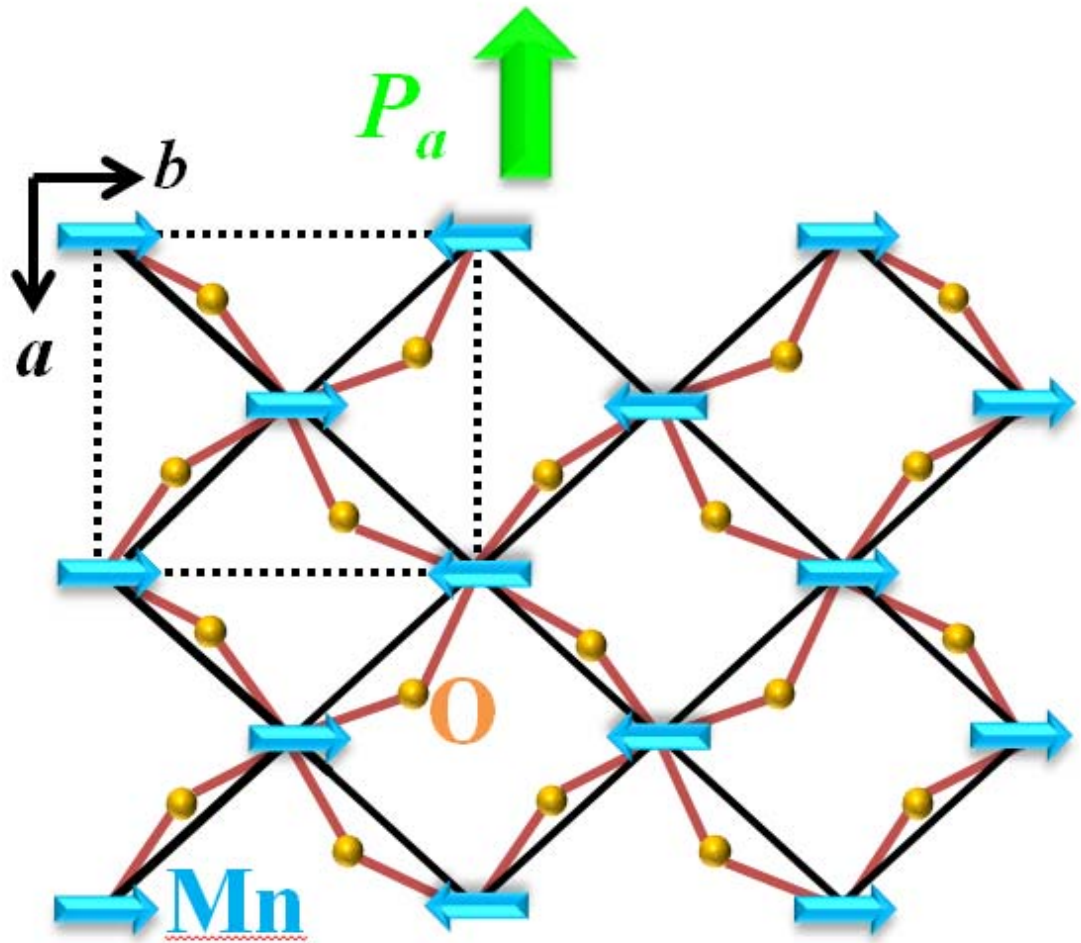


FIG. I. 5. Lattice and magnetic structure of E-type orthorhombic  $\text{REMnO}_3$ . RE atoms are not shown. Oxygen displacements reflect the effect of Mn-Mn exchange striction. Dashed line shows structural unit cell.

electric fields has rarely been presented so far.

Recently, a new way of achieving a giant magnetoelectric effect in a multiferroic was presented by utilizing the high sensitivity of the coexistence of competing magnetic phases to external perturbations such as electric and magnetic fields [19]. In  $\text{Eu}_{0.75}\text{Y}_{0.25}\text{MnO}_3$  with the presence of magnetic fields, a multiferroic phase with spiral magnetism intricately balances with an emergent weak ferromagnetic phase. Coexistence of competing two phases in a broad range of  $T$ - $H$  phase space results from kinetic arrest/de-arrest processes of the first order multiferroic to weak ferromagnetic phase transition [20, 21]. The resulting frozen/melted magnetoelectric glass states exhibit fascinating temperature dependent hysteretic behaviors of magnetic and ferroelectric properties with variation of temperature and magnetic field, in close analogy with the magnetic and transport behaviors of CMR (colossal magnetoresistance) manganites with a magnetic glass [22, 23]. It appears that coexistence of the competing phases can be significantly influenced by electric and magnetic fields, through changing the relative volume fraction of multiferroic and weak ferromagnetic phases. It leads to a remarkable control of magnetization and polarization with electric and magnetic fields. The magnitudes of magnetization and polarization are significantly reduced and promoted, respectively, by applying electric fields, and they behave in the opposite tendency under magnetic fields. FIG. I. 7. shows the demonstration of the repeatable variation of magnetization and polarization at some fixed temperatures by linearly-oscillating electric and magnetic fields, respectively.

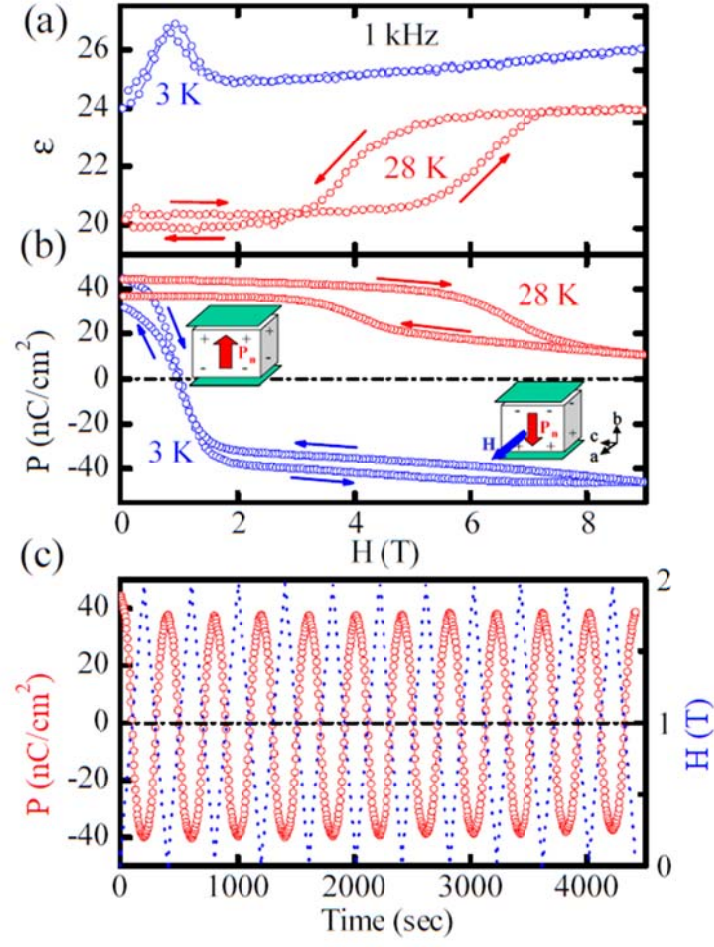


FIG. I. 6. Reproducible polarization reversal by magnetic fields in TbMn<sub>2</sub>O<sub>5</sub>. (a) Dielectric constant versus applied magnetic field at 3 and 28 K. (b) Change of total electric polarization by applied magnetic fields at 3 and 28 K. The cartoon shows the orientation of the net polarization in zero field and high fields  $> 2$  T. (c) Polarization flipping at 3 K by linearly varying magnetic field from 0 to 2 T. These results clearly display highly reproducible polarization switching by magnetic fields [2].



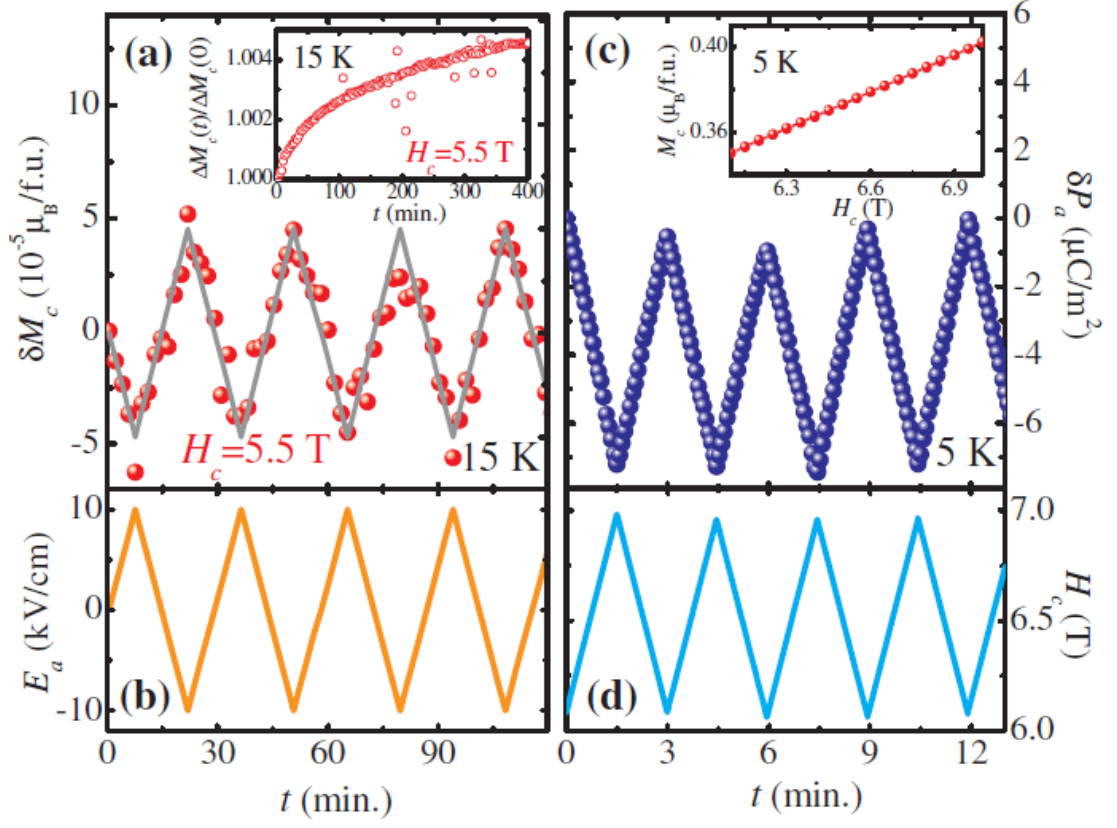


FIG. I. 7. (a), (b) Repeated variation of  $\Delta M_c$  ( $\delta M_c$ ) at 15 K in  $H_c = 5.5$  T by applying  $E_a$ , varied lineally with time between +10 and -10 kV/cm. The inset shows time-dependent  $\Delta M_c$  in  $H_c = 5.5$  T at 15 K without  $E_a$ . [19]

## 5. Imaging Multiferroic Vortices

Hexagonal  $\text{REMnO}_3$  (RE=Ho-Lu, Y and Sc) is a multiferroic which possesses both ferroelectricity ( $T_C \sim 1200 - 1500$  K) and antiferromagnetism ( $T_N \sim 70 - 120$  K) [24]. The structure comprises triangular lattice layers of  $\text{MnO}_5$  polyhedra which are tilted to form the trimerization of Mn ions in each layer (FIG. I. 8). Ferroelectric polarization emerging along the  $c$  axis originates from the trimer-induced opposite displacements of RE ions with non-equal portions, i.e., downward displacements of  $2/3$   $4b$ -site Re ions and upward displacements of  $1/3$   $2a$ -site RE ions [25]. Below  $T_N$ , the neighboring  $\text{Mn}^{3+}$  spins arrange antiferromagnetically with a relative angle of  $120^\circ$  in a triangular lattice in the  $ab$ -plane. A new trend in multiferroics research stems from the recent observation of vortex-antivortex domain structures found in hexagonal multiferroic  $\text{YMnO}_3$  by performing transmission electron microscopy (TEM) and conductive atomic force microscopy (CAFM) at room temperature [10] as shown in FIG. I. 9. The investigation reveals that six distinguishable domains are merged together at one point and those domains are composed of three types of antiphase domains ( $\alpha$ ,  $\beta$ , and  $\gamma$ ) and two ferroelectric domains (+ and -) resulting in the observed cloverleaf-like patterns with cyclic arrangement of 6 domain configurations ( $\alpha^+$ ,  $\beta^-$ ,  $\gamma^+$ ,  $\alpha^-$ ,  $\beta^+$ , and  $\gamma^-$ ). Interestingly, various configurations of topological vortices and antivortices result in a large-scale domain pattern in a way to form a self-organized network which can also be observed simply under an optical microscope [11]. Moreover, the network formation can be analyzed in terms of graph theory and can be properly colored, reflecting the nature of self-organized criticality.

Most recently, the study of h-ErMnO<sub>3</sub> by a magnetic force microscopy (MFM) at low temperature and a piezo-response force microscopy (PFM) at room temperature (FIG. I. 10) verified that the topological vortex-antivortex patterns are the true multiferroic domains in that the ferroelectric and antiferromagnetic domains are interlocked [reference]. The result shows that uncompensated magnetic moments at domain walls are present and alternate through the vortex-antivortex network, reflecting collective magnetism at ferroelectric domain walls. In addition, spin chirality in domains appears to be controllable by applying magnetic fields.

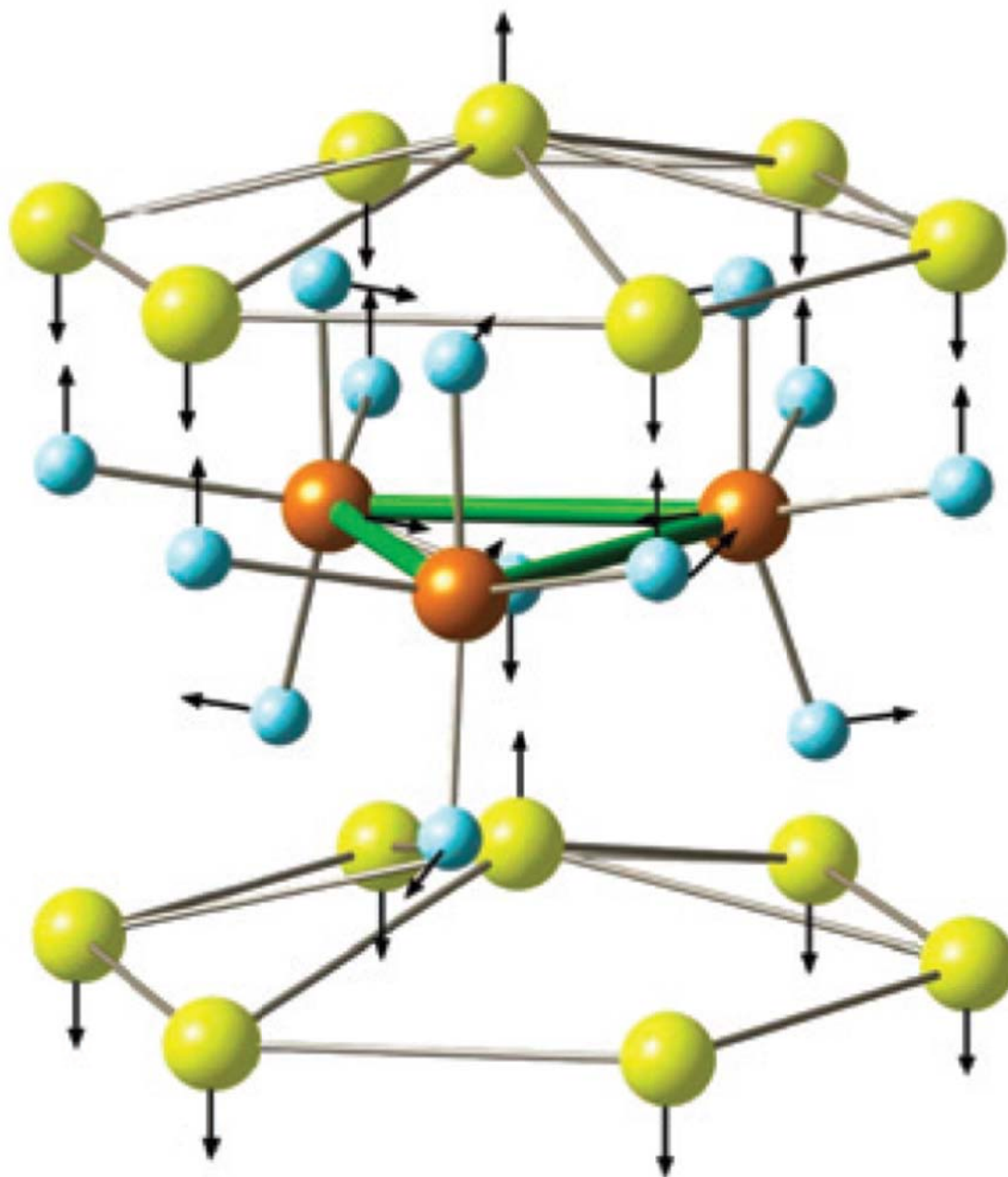


FIG. I. 8. A three dimensional structure of hexagonal  $\text{RE MnO}_3$ . The yellow, brown and light blue circles represent RE, Mn and O ions, respectively. The arrows show the direction of displacements. Green triangle represents the Mn trimer [10].

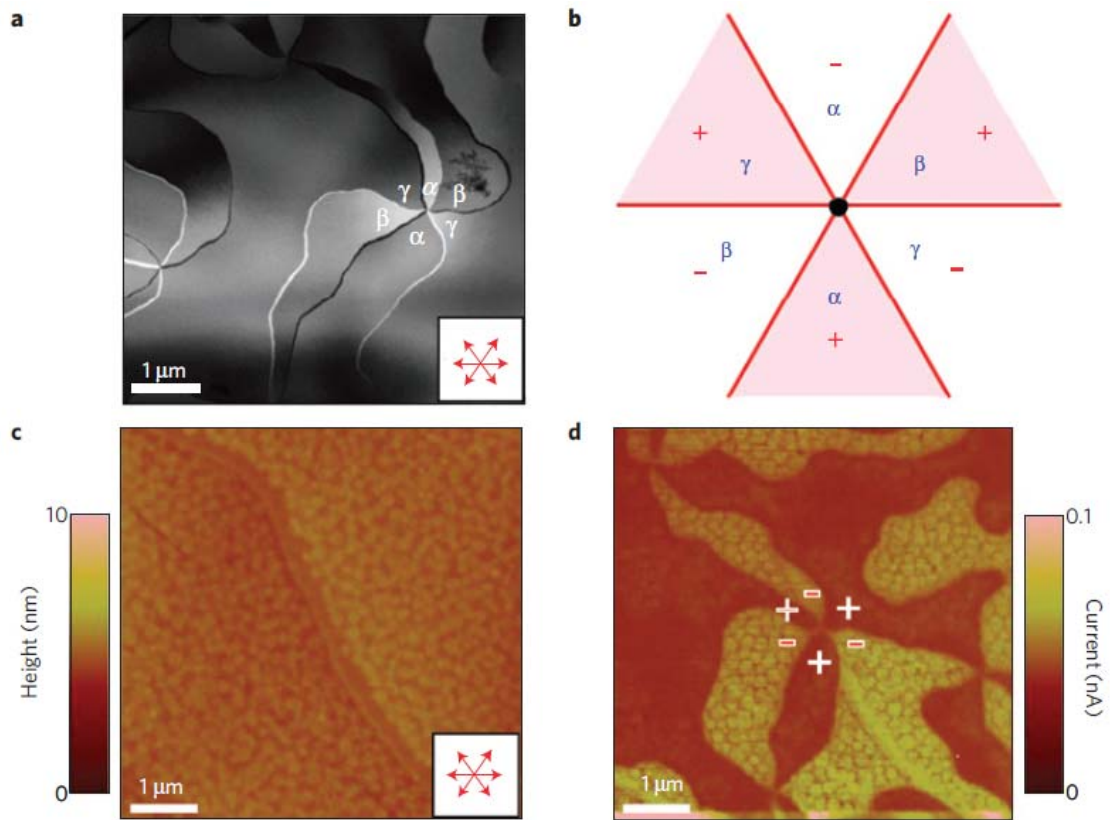


FIG. I. 9. (a) Transmission electron microscopy image showing six antiphase domains merging to one point. (b) Proposed cloverleaf configuration of six antiphase/ferroelectric domains. (c,d) Topography and conductive atomic force microscopy images obtained in contact mode [10].

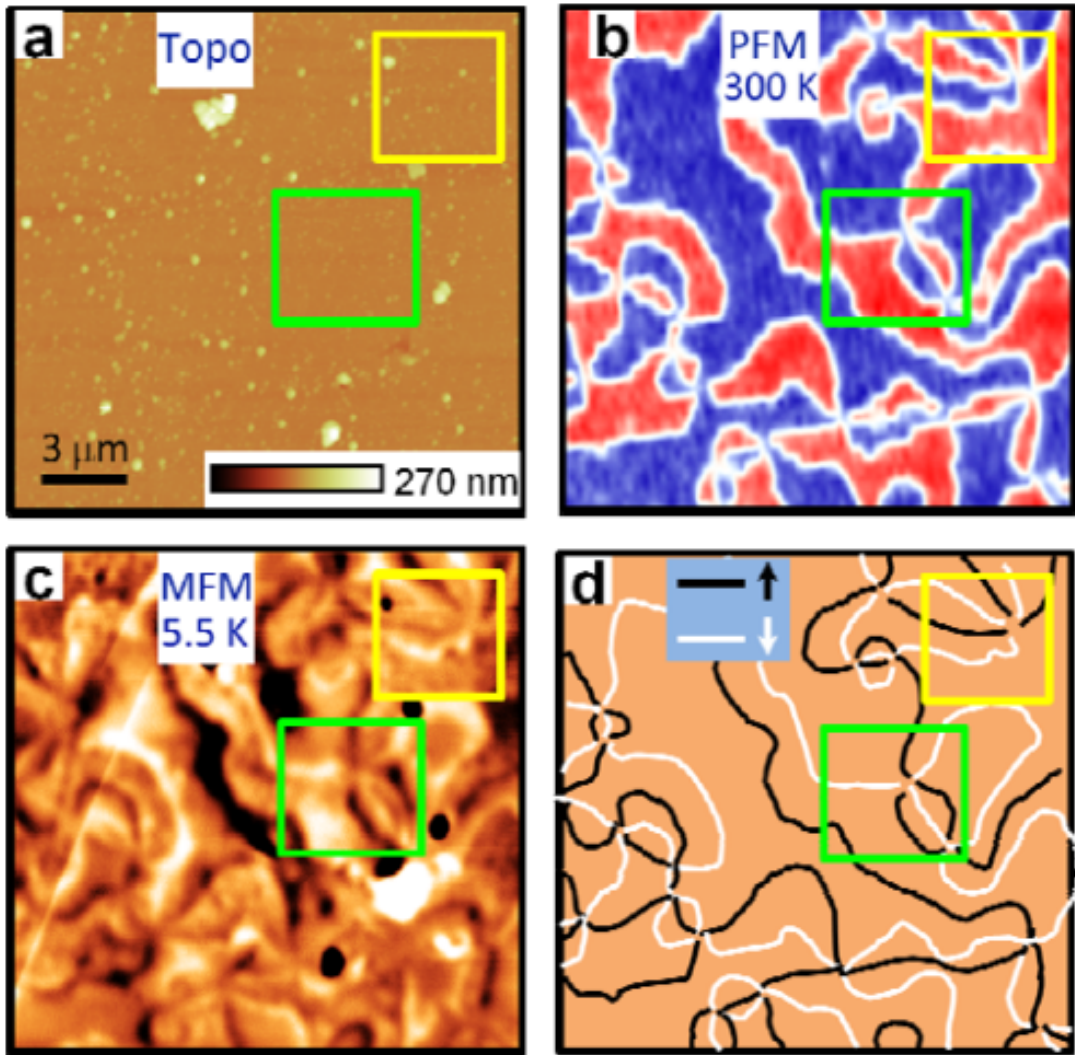


FIG. I. 10. Correlation of DW magnetism over the vortex network. a, topography b, room temperature PFM image, and c, MFM image (5.5 K, 0.2 T, lift height: 180 nm) taken at the same location on the (001) surface of a h-ErMnO<sub>3</sub> single crystal. The color scale for the topography and MFM ( $\Delta f$ ) are 270 nm and 0.4 Hz, respectively. The red and blue colors in the PFM image correspond to up and down ferroelectric domains, respectively. d, a cartoon sketch of the DW net moments over the entire field of view based on MFM data in fig. 1c (the same location as the green boxes) and the vortex connectivity in b (PFM). Black (white) lines represent up (down) net moments [12].

## 5. REFERENCES

- [1] T. Kimura, *et al.*, Nature **426**, 55 (2003).
- [2] N. Hur, *et al.*, Nature **429**, 392 (2004).
- [3] Y. Tokunaga, *et al.*, Nat. Mater. **8**, 558 (2009).
- [4] K. Marty, *et al.*, Phys. Rev. Lett. **101** (2008).
- [5] S. Park, *et al.*, Phys. Rev. Lett. **98**, 057601 (2007).
- [6] Y. J. Choi, *et al.*, Phys. Rev. Lett. **100**, 047601 (2008).
- [7] S. Yáñez-Vilar, *et al.*, Phys. Rev. B **84** (2011).
- [8] S. Seki, *et al.*, Phys. Rev. Lett. **101** (2008).
- [9] R. D. Johnson, *et al.*, arXiv:1110.4585v1 [cond-mat.str-el].
- [10] T. Choi, *et al.*, Nat. Mater. **9**, 253 (2010).
- [11] S. C. Chae, *et al.*, Proc. Natl Acad. Sci. U. S. A. **107**, 21366 (2010).
- [12] Y. Geng, *et al.*, arXiv:1201.0694v1 [cond-mat.str-el].
- [13] I. A. Sergienko, *et al.*, Phys. Rev. B **73**, 094434 (2006).
- [14] P. G. Radaelli, *et al.*, J. Phys. Condes. Matter **20** (2008).
- [15] J. van den Brink, *et al.*, J. Phys. Condens. Matter **20**, 434217 (2008).
- [16] I. Sergienko, *et al.*, Phys. Rev. Lett. **97** (2006).
- [17] S. Picozzi, *et al.*, Phys. Rev. Lett. **99** (2007).
- [18] N. Hur, *et al.*, Phys. Rev. Lett. **93**, 107207 (2004).
- [19] Y. Choi, *et al.*, Phys. Rev. Lett. **105** (2010).
- [20] P. Chaddah, *et al.*, Phys. Rev. B **77** (2008).
- [21] K. Kumar, *et al.*, Phys. Rev. B **73** (2006).

- [22] M. Uehara, *et al.*, Nature **399**, 560 (1999).
- [23] P. Schiffer, *et al.*, Phys. Rev. Lett. **75**, 3336 (1995).
- [24] X. Fabrèges, *et al.*, Phys. Rev. B **78** (2008).
- [25] B. B. Van Aken, *et al.*, Nat Mater **3**, 164 (2004).



## **Chapter II**

**New exchange-striction mechanism of ferroelectricity in  
multiferroic orthorhombic  $\text{HoMnO}_3$**

## 1. Introduction

Multiferroics attract significant attention because of cross-coupling between magnetism and ferroelectricity (FE), and the related possibility of controlling magnetism with an electric field (and vice versa) [1, 2]. FE induced by magnetic order is especially interesting because of the strong effect of a magnetic field ( $H$ ) on the ferroelectric order. Exchange striction is a major mechanism producing FE in magnetically ordered systems [2]. Both symmetric and antisymmetric parts of the exchange coupling can drive FE. The latter case is known to occur in spiral magnets, such as  $\text{TbMnO}_3$  [2]. These systems exhibit small electric polarizations ( $\mathbf{P}$ ) of the order of  $10^{-1} \mu\text{C}/\text{cm}^2$  – three orders of magnitude smaller than in proper ferroelectrics. Symmetric exchange is expected to produce much larger  $\mathbf{P}$ . However, the corresponding materials identified so far show similarly small values of  $\mathbf{P}$  [3, 4]. Theoretical predictions [5, 6] of a 100 times larger  $\mathbf{P}$  in the magnetic  $E$ -phase of orthorhombic perovskite manganites  $\text{o-}R\text{MnO}_3$  ( $R=\text{Ho-Lu}$ , and  $\text{Y}$ ) induced by Mn-Mn exchange striction has, therefore, attracted a lot of interest [7-10]. Unfortunately, these compounds exhibit [9, 10] maximum  $\mathbf{P}$  values of only  $\sim 10^{-1} \mu\text{C}/\text{cm}^2$ . In many cases (*e.g.* for  $R=\text{Ho}$ ), any significant  $\mathbf{P}$  is achieved only below the rare earth magnetic ordering temperature ( $T$ ) [9]. This indicates an essential role of the rare earth magnetism, which is unaccounted for in the extant models. Importantly, all the  $E$ -type manganites studied so far have been only synthesized in the polycrystalline form, preventing characterization of many of their intrinsic properties.

In this paper, we report the first studies on single crystals of orthorhombic  $\text{HoMnO}_3$  ( $\text{o-HoMnO}_3$ ). Unexpectedly, we find that  $\mathbf{P}$  is pointing along crystallographic

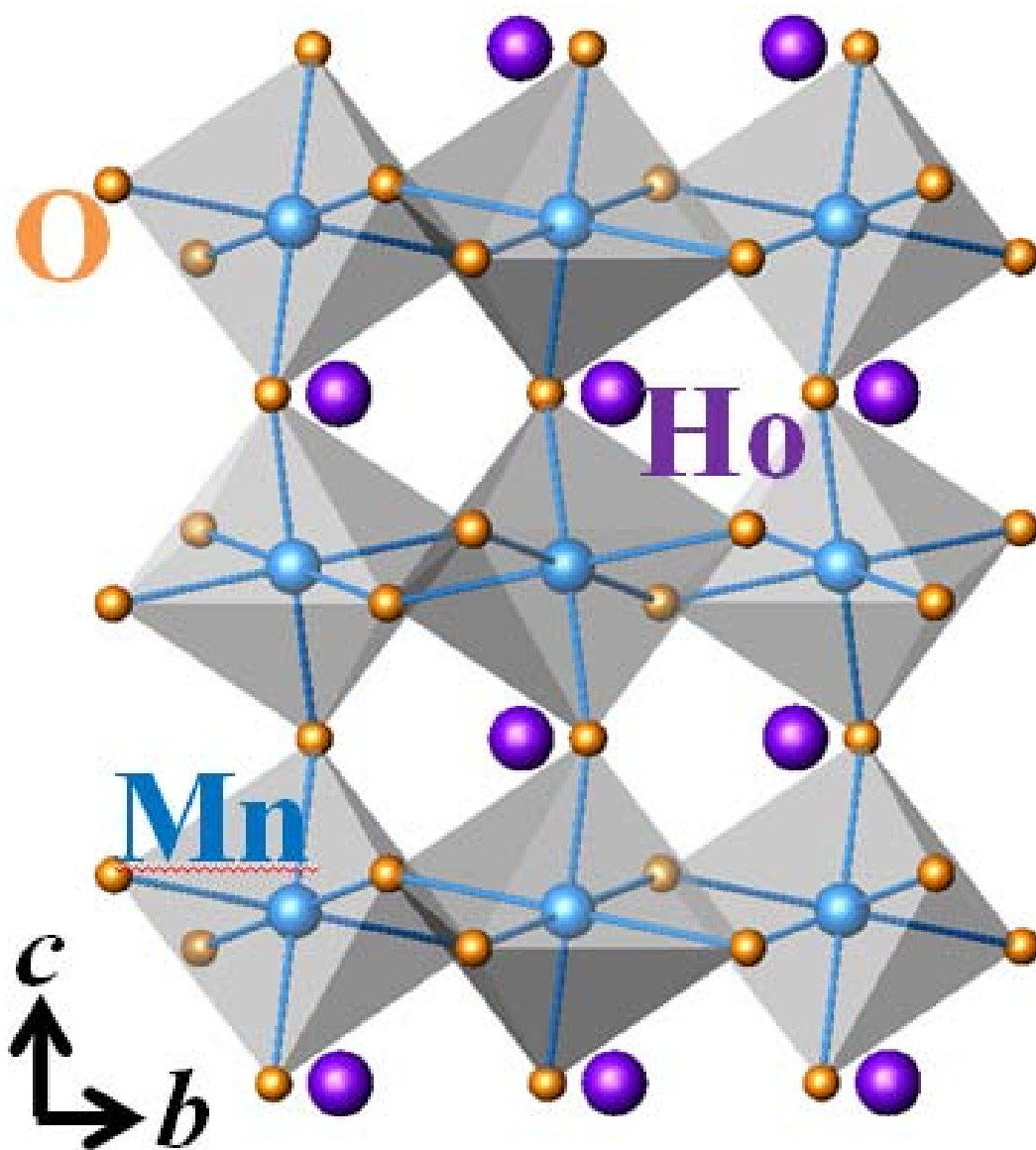


FIG. II. 1. The crystal structure of the  $\text{o-HoMnO}_3$  viewed from  $a$ -axis. The gray

$c$ -axis, contrary to the theoretical prediction [5, 6] of  $\mathbf{P}||a$ . We argue that Ho-Mn exchange striction plays a key role in this system, and discuss possible outcomes of the Mn-Mn interaction in the orthorhombic manganites. Our model predicts that in magnetic rare earth manganites, coexisting Mn-Mn and  $R$ -Mn interactions can give rise to a new phenomenon – a temperature-dependent direction of  $\mathbf{P}$ .

## 2. Experimental Method

o-HoMnO<sub>3</sub> crystallizes in a distorted perovskite structure (space group  $Pbnm$ ), shown in FIG. II. 1. We have synthesized rod-like large single crystals with dimensions up to 2x2x7 mm<sup>3</sup> (see FIG. II. 3.) utilizing conventional Bi<sub>2</sub>O<sub>3</sub> flux method. Previously, polycrystalline o-HoMnO<sub>3</sub> has been obtained using high-pressure synthesis. We find that flux growth with Bi<sub>2</sub>O<sub>3</sub>, Ho<sub>2</sub>O<sub>3</sub> and MnO<sub>2</sub> can stabilize both hexagonal *and* orthorhombic crystals at the ambient pressure. Mixture of Bi<sub>2</sub>O<sub>3</sub>:Ho<sub>2</sub>O<sub>3</sub>:MnO<sub>2</sub> = 6:0.5:1 ratio produces the hexagonal phase, whereas 12:0.5:1 ratio leads to orthorhombic single crystals. The crystals exhibit an orthorhombic perovskite structure with  $a=5.2689(2)$ ,  $b=5.8450(2)$ , and  $c=7.3698(2)$  Å at room temperature, and no twinning, as confirmed by refinement of single-crystal x-ray diffraction data. It is consistent with previously published structure of polycrystalline samples [11, 12]. The absence of twinning was further confirmed by neutron diffraction experiments, in which a careful search revealed no diffraction peaks due to possible twin domains. Magnetization ( $M$ ) was measured with a SQUID magnetometer.  $\mathbf{P}$  and dielectric constant ( $\epsilon$ ) were obtained by integrating pyroelectric current measured with an electrometer and using an LCR meter at  $f=44$  kHz, respectively.

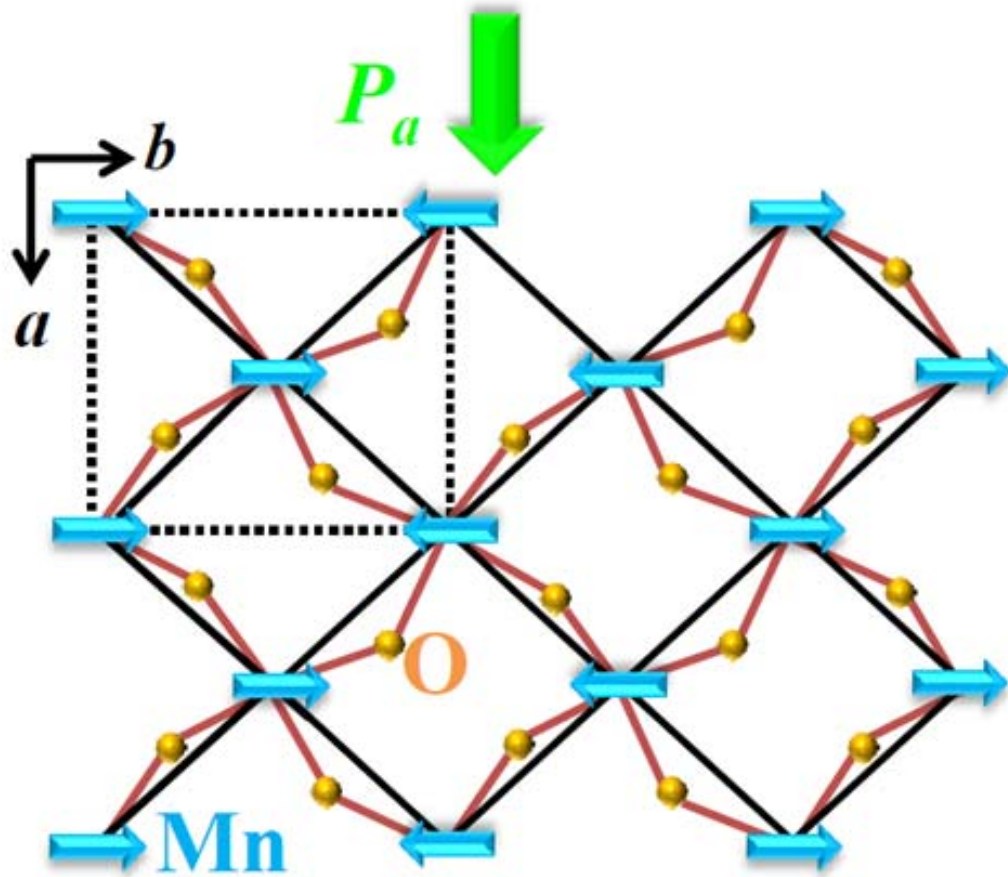


FIG. II. 2. Lattice and magnetic structure ( $k=0.5$ ) of E-type orthorhombic  $RMnO_3$ .  $R$  atoms are not shown. Oxygen displacements reflect the effect of Mn-Mn exchange striction. Dashed line shows structural unit cell. The magnetic unit cell is twice as large in the  $y$  direction.

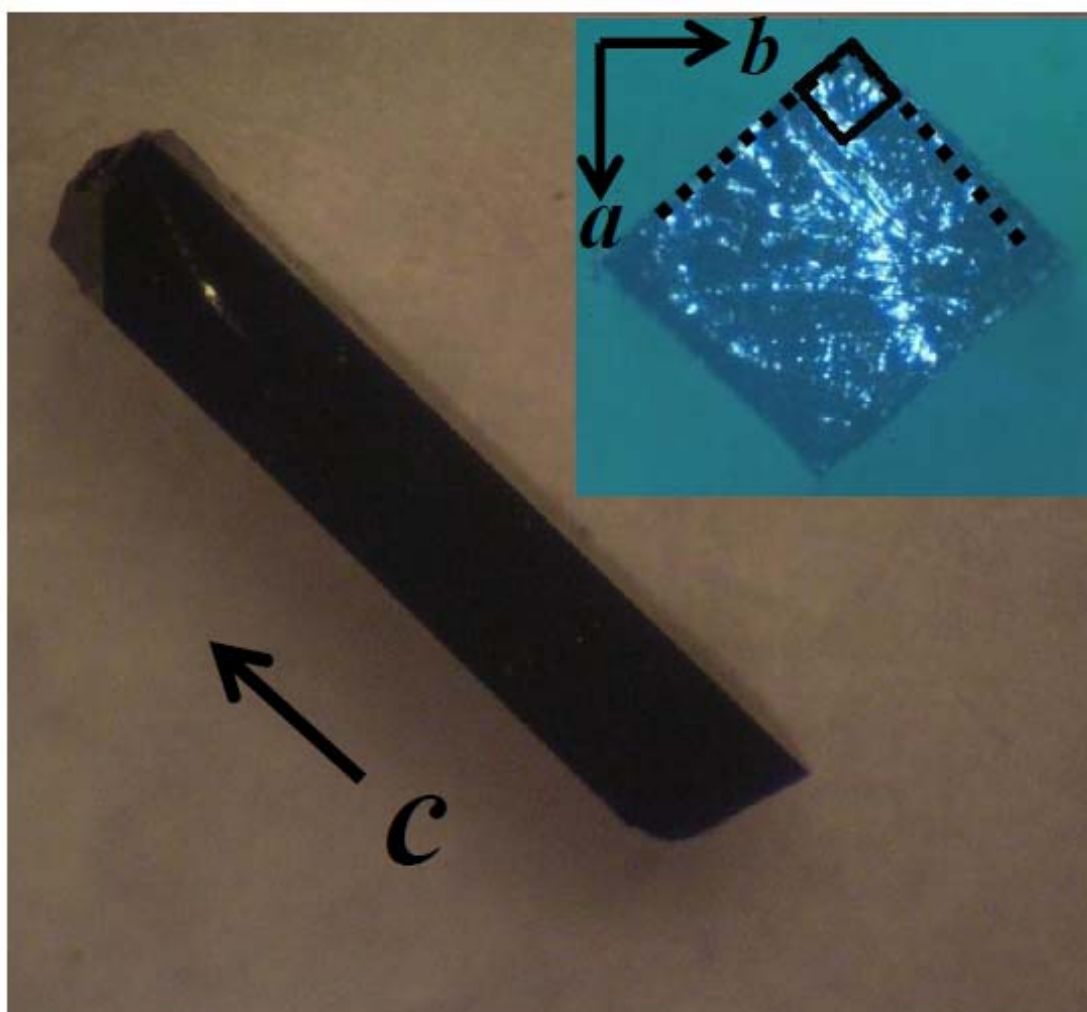


FIG. II. 3. The image of flux grown single crystal of o-HoMnO<sub>3</sub>.

Neutron diffraction data were collected on BT9 triple-axis spectrometer at NIST Center for Neutron Research.

### 3. Result and Discussion

Mn spins in o-HoMnO<sub>3</sub> order at  $T_N \approx 40$  K, exhibiting  $(0, A_y, 0)$ -type incommensurate structure with wave vector  $Q=(h, k, l)=(0, \sim 0.4, 0)$ , and spins parallel to the  $b$  axis [11]. At a lower  $T$ , *some* polycrystalline samples [12] become commensurate with  $k=0.5$ , exhibiting the  $E$ -type order discussed theoretically in Ref. [5], and shown in FIG. II. 2. For  $T < 15$  K, Ho spins order in the  $(a_x, f_y, 0)$  pattern and the same  $Q$  as Mn [11]. Our data are consistent with these results. Magnetic field ( $H$ ) and  $T$  dependences of  $M$  are shown in FIGs. II. 4.(a,b). The anomalies corresponding to  $T_N=42$  K and  $T_{Ho}=15$  K are clearly observed in the  $T$  derivative of  $M_c$  shown in the inset in FIG. II. 4(b), as well as in the  $M_a$  and  $M_b$  derivatives (not shown). At low  $T$ , substantial magnitude of  $M_b$  develops, possibly due to Ho contribution. FIGs. II. 5 and 6 show  $T$  dependence of various physical properties under zero  $H$ . Onset of tiny ferroelectric polarization along the  $c$  axis ( $P_c$ ) at  $T=30$  K appears (FIG. II. 5.(a)), and  $P_c$  exhibits an abrupt increase at  $T_{Ho}=15$  K, reaching  $1,500 \mu\text{C}/\text{m}^2$  at 2 K. The magnitudes of  $P_a$  and  $P_b$  are negligible at any  $T$ . Dielectric constant along the  $c$  axis ( $\epsilon_c$ ) displays a pronounced peak at  $T_{Ho}$ , in accordance with the appearance of FE, whereas  $\epsilon_a$  increases broadly below  $T_N$ , see FIG. II. 5.(b). The specific heat, shown in FIG. II. 6.(b), exhibits a sharp peak at  $T_N$ , and a small (but discernable) anomaly at  $T_{Ho}$  is also visible.

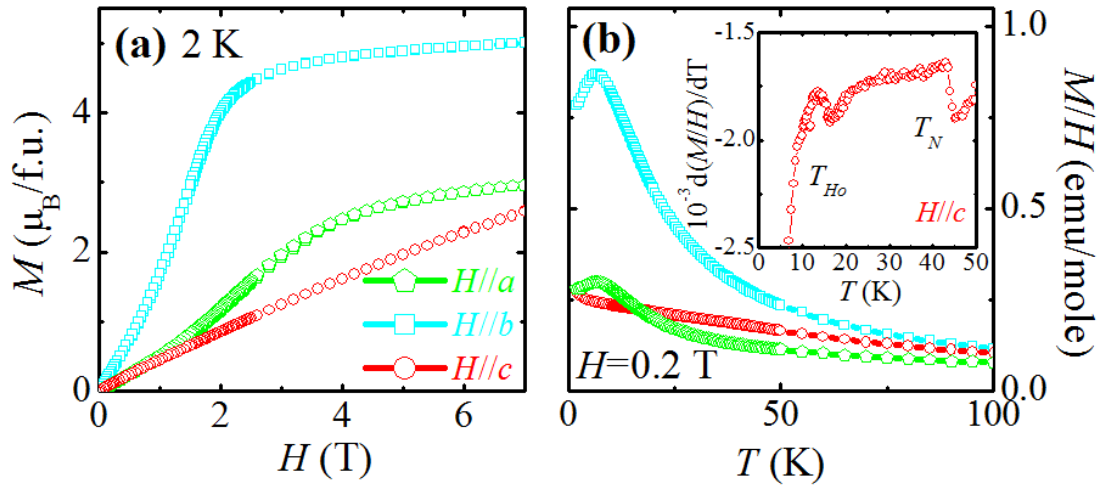


FIG. II. 4. (a) Magnetization vs. magnetic field for  $T=2$  K. (b) Magnetic susceptibility vs. temperature ( $1 \text{ emu}=4\pi \cdot 10^{-6} \text{ m}^3$ ). The inset shows temperature derivative of the susceptibility.



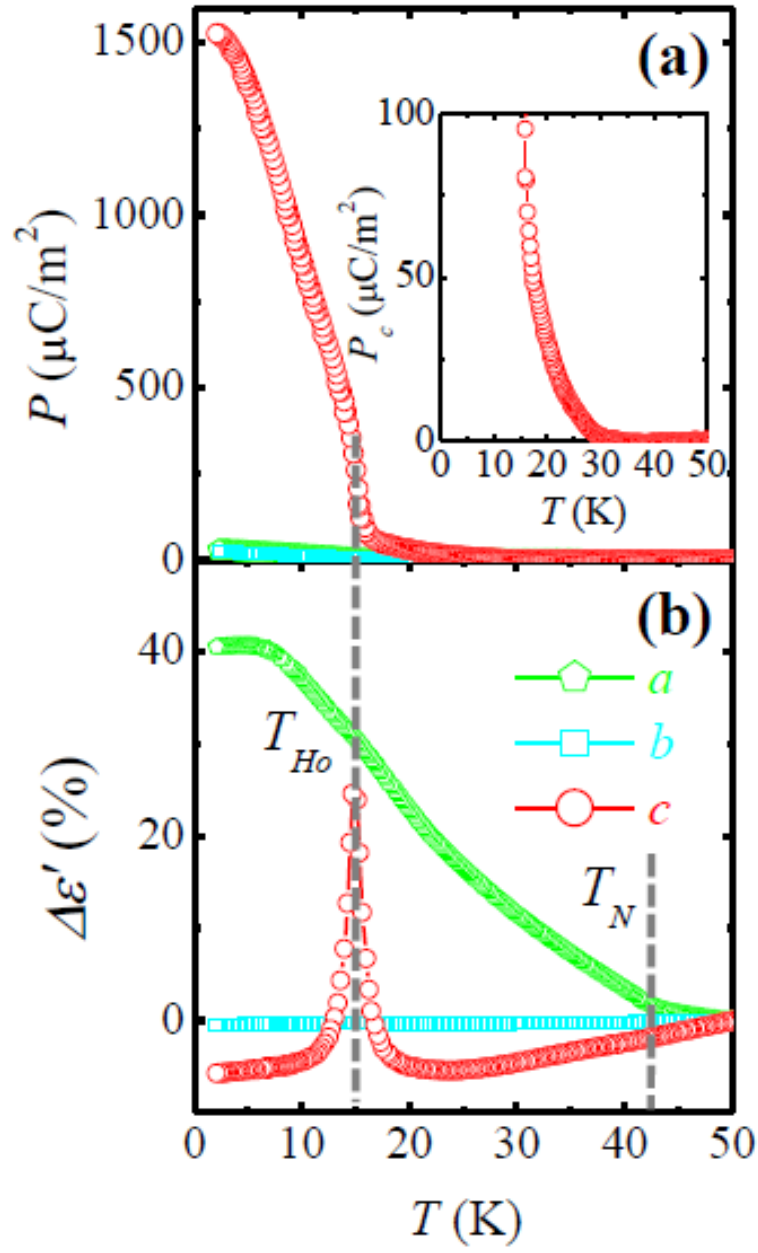


FIG. II. 5. Temperature dependences of the electric polarization (a) and dielectric susceptibility (b) along the three crystallographic axes.

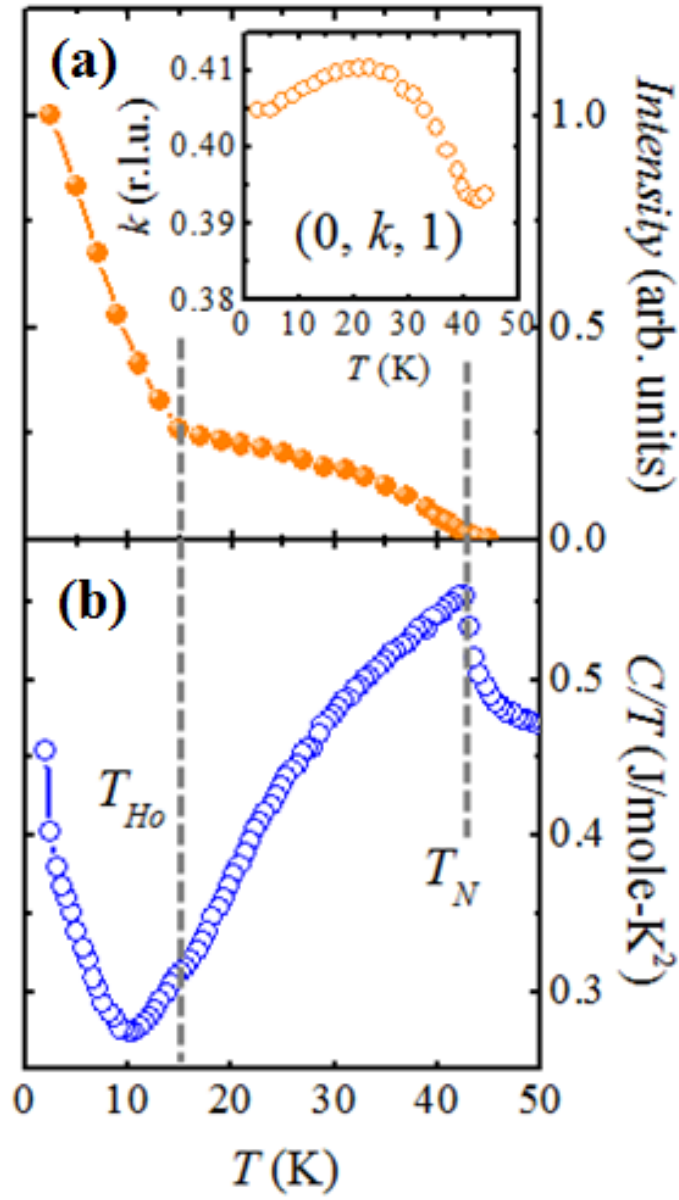


FIG. II. 6. (a) Integrated intensity of the  $(0,k,1)$  magnetic peak vs. temperature. The  $k$  component of the peak position is shown in the inset. (b) Temperature dependence of the specific heat.

Neutron diffraction data show that our samples are incommensurate at all temperatures. FIG. II. 6.(a) shows the  $T$  dependence of the integrated intensity of the  $(0, k, 1)$  magnetic peak,  $k \approx 0.4$ . The magnetic order appears at  $T_N = 42$  K, and the peak intensity increases significantly for  $T < T_{Ho}$ , simultaneously with a large increase of  $P_c$ . Inset in FIG. II. 6.(a) shows the  $T$ -dependent position  $k$  of the magnetic peak obtained from Gaussian fits. With decreasing  $T$ ,  $k$  exhibits a slight variation, but always stays close to  $k = 0.4$ . There appear to be changes in the slope of this dependence in the vicinity of the FE anomalies at  $\sim 30$  K, and at 15 K, reflecting the magnetoelectric coupling in this system.

The FE in the  $E$ -type manganites is currently believed [5, 6] to be induced by Mn-Mn symmetric exchange striction, *i.e.* repulsion of co-aligned Mn spins. This repulsion, together with the associated motion of the oxygen ions, leads to the appearance of  $P_a$ , as illustrated in FIG. II. 2. for the  $k = 0.5$  commensurate state. The Mn spin is given by  $S_y(y) = S \cos(ky - \varphi_i)$ , where  $\varphi_0$  and  $\varphi_{1/2}$  are the phases for the two spin chains along the  $b$  axis in the unit cell, one at  $x = 0$ , and the other at  $x = 0.5$  ( $x, y$  are in lattice units), see FIG. II. 7.(a). In the  $E$ -type commensurate state,  $k = 0.5$ ,  $\Delta\varphi \equiv \varphi_{1/2} - \varphi_0 = \pi/2$ , and the magnetic structure lacks the inversion symmetry, *i.e.* is acentric. Superimposed on the lattice structure, it is consistent with non-zero  $P_a$ . In the  $k \neq 0.5$  state the spin magnitude is not constant, and other phase differences  $\Delta\varphi$  are allowed, leading to both polar acentric (*e.g.*  $\Delta\varphi = \pi/2$ ), and centric ( $\Delta\varphi = 0$  and  $\pi$ ) spin density waves (SDW) [13]. In the latter case,  $P_a = 0$  if the inversion centers of the SDW and the atomic structure coincide. In our samples, measured  $P_a$  is zero, and therefore the centric incommensurate SDW must be realized. One of the two possible Mn magnetic structures for the centric incommensurate

SDW, corresponding to  $\Delta\varphi=0$ , is shown in FIG. II. 7.(a), the other with  $\Delta\varphi=\pi$  simply has the opposite spin direction for  $x=0.5$ . (For simplicity, the  $k=0.4$  state with period of exactly 5 unit cells is shown.) These structures are antiferroelectric, with one half of the unit cell having the opposite  $P_a$  to the other. Large increase of  $\varepsilon_a$  below  $T_N$  (FIG. II. 5.) without the presence of  $P_a$  strongly supports this conclusion.

The primary result of our work is the unexpected direction of  $\mathbf{P}$ . Because of the clear association of FE with the Ho order, the natural candidate mechanism of multiferroicity is Ho-Mn interaction. In fact, rare-earth – 3d element interaction was reported to be essential in multiferroic orthoferrites [14, 15], as well as to play a role in some spiral manganites [16, 17]. We find that Ho-Mn exchange striction indeed provides a simple explanation for the observed phenomena. Disregarding the  $x$  component of the Ho spins which does not contribute to the striction, the Ho SDW order essentially follows that of Mn, but with an experimentally undetermined phase shift between the two [11]. To maximize the energy gain from the Ho-Mn striction producing the  $c$ -axis displacement, the phase shift should be zero or  $\pi$  because it pairs large Ho and Mn spins adjacent in the  $x$  direction (the Mn spins adjacent in the  $y$  direction are antiparallel to each other for the same  $z$ , partially cancelling the effect of the striction). As shown in FIG. II. 7.(b) for one of these phase shifts, the Ho spin is then anti-aligned with the 3 Mn spins below, and aligned with the 3 Mn spins above, and moves down due to exchange striction. One can readily check that in this case, Mn-Ho exchange striction moves all the Ho spins of one chain (*e.g.* for  $x=0$ ) in the same direction along the  $c$  axis. The energy gain is the same for aligning with the Mn spins above or below the Ho atom, and therefore the  $x=0$  and  $x=0.5$  Ho chains in the magnetic unit cell can either have the same or the opposite

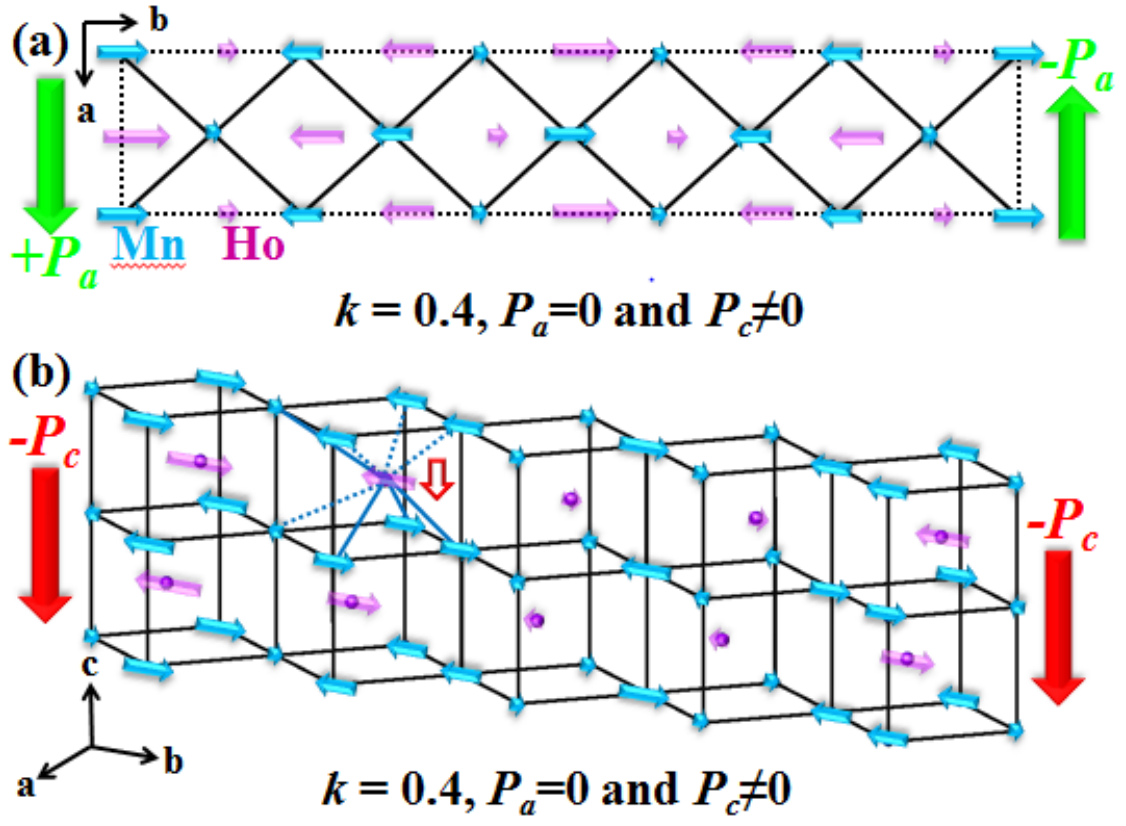


FIG. II. 7. (a), (b) The magnetic order leading to  $P_a=0$  and  $P_c>0$  in the  $k=0.4$  state. Dashed line in (a) outlines the magnetic unit cell. In (b), thick solid and dashed lines designate attractive and repulsive Ho-Mn interactions, respectively.

directions of  $P_c$ . Experimentally,  $P_c \neq 0$ , and therefore the Ho order shown in FIGs. II. 7. (a,b) which produces the same  $P_c$  in every Ho chain should be realized. Clearly, experimental confirmation of this phase relationship between the Ho and Mn SDWs, and whether it is affected by the poling used for  $P_c$  measurements, would be of significant interest. Finally, we note that the onset of the weak  $P_c$  at  $T \approx 30$  K could be produced via the mechanism due to weak Ho moment induced by the Mn order, which was previously observed in polycrystalline samples [12].

o-HoMnO<sub>3</sub> exhibits a strong magnetoelectric effect. FIG. II. 9.(a) shows the full suppression of  $P_c$  at  $H=2$  and  $4$  T for  $H//b$  and  $H//a$ , respectively. For  $H//c$ , only a small decrease of  $P_c$  is found. The suppression of  $P_c$  coincides with a drop in  $\epsilon_c$  (FIG. II. 9.(b)), and with an anomaly in  $dM/dH$  (inset in FIG. II. 9.(a)). The vanishing polarization is probably associated with field-induced reorientation of the Ho spins and the corresponding changes in the effects of Ho-Mn exchange striction. Our data show that the reorientation is easier to achieve in the  $ab$  plane, consistent with the magnetic anisotropy that tends to confine the Ho spins there [11, 12]. FIGs. II. 10 and 11 show  $T$  dependences of  $P_c$  and  $\epsilon_c$  in various applied fields. Consistent with the data of FIGs. II. 9.(a,b), magnetic field suppresses the ferroelectric state, and decreases the ferroelectric transition temperature.

Presence of two coexisting exchange-striction mechanisms of multiferroicity in the E-type orthorhombic manganites is the key result of this work. Depending on the phase relationships within and between the Mn and Ho SDWs, both Mn-Mn and Ho-Mn

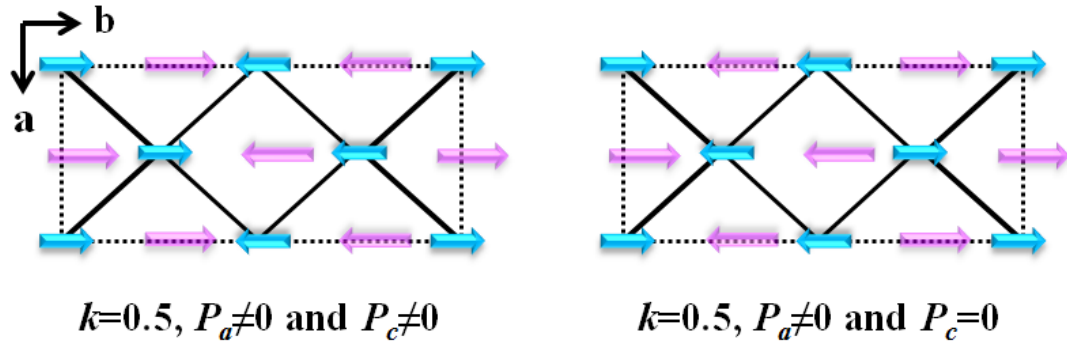


FIG. II. 8. Spin structures with zero and non-zero c-axis polarization in the  $k=0.5$   $E$ -type state. In all figures, the  $a$ -axis components of the Ho spins are not shown.

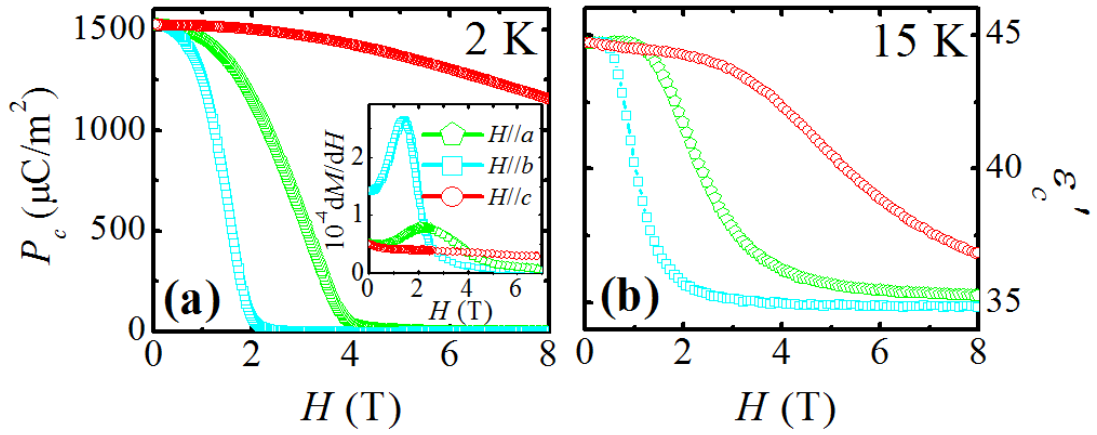


FIG. II. 9. Magnetic field dependences of the electric polarization  $P_c$  (a) and dielectric susceptibility  $\epsilon_c$  (b) for different directions of  $H$ .

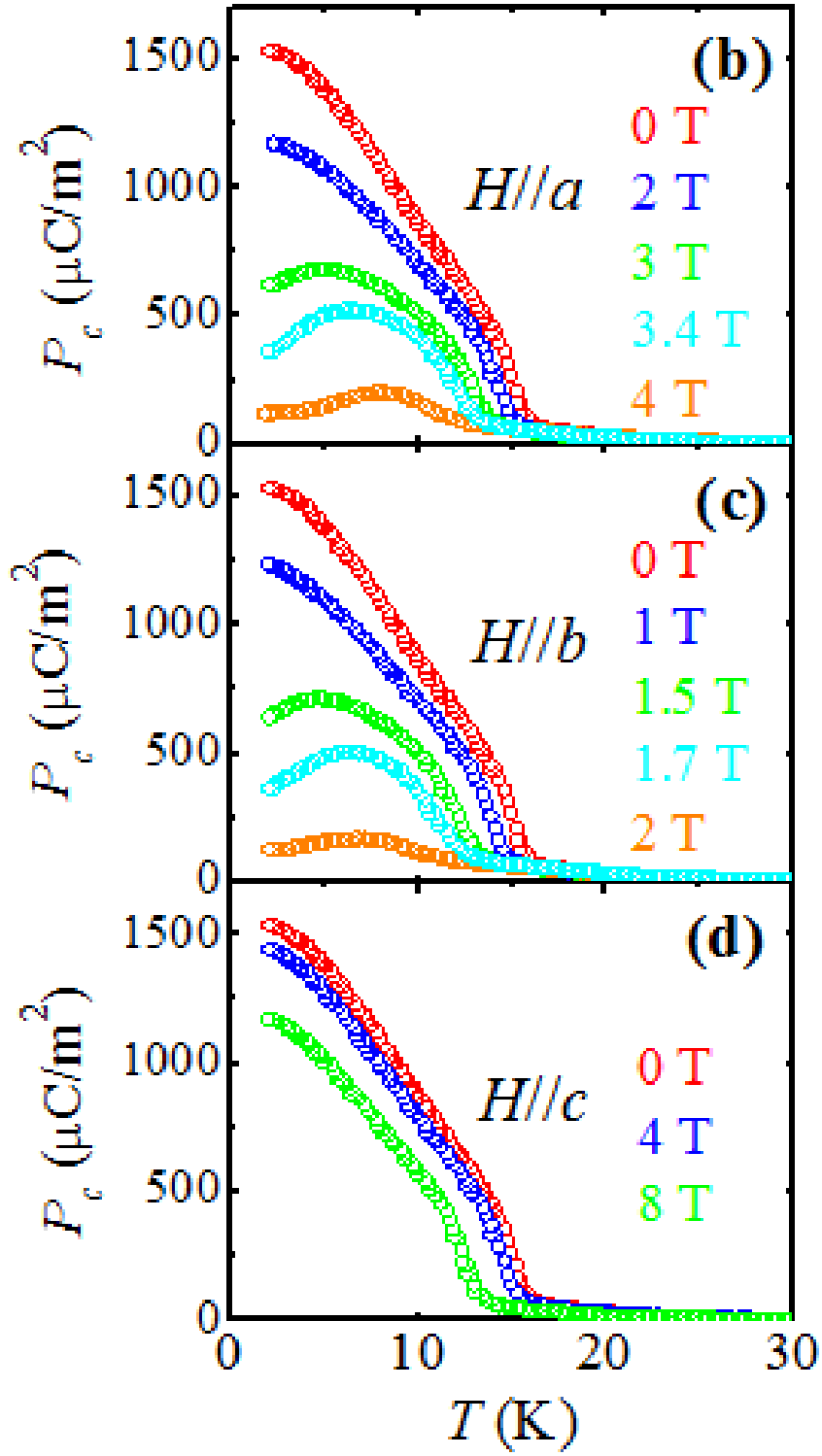


FIG. II. 10. Temperature dependences of the electric polarization (a-c) in various applied magnetic fields.



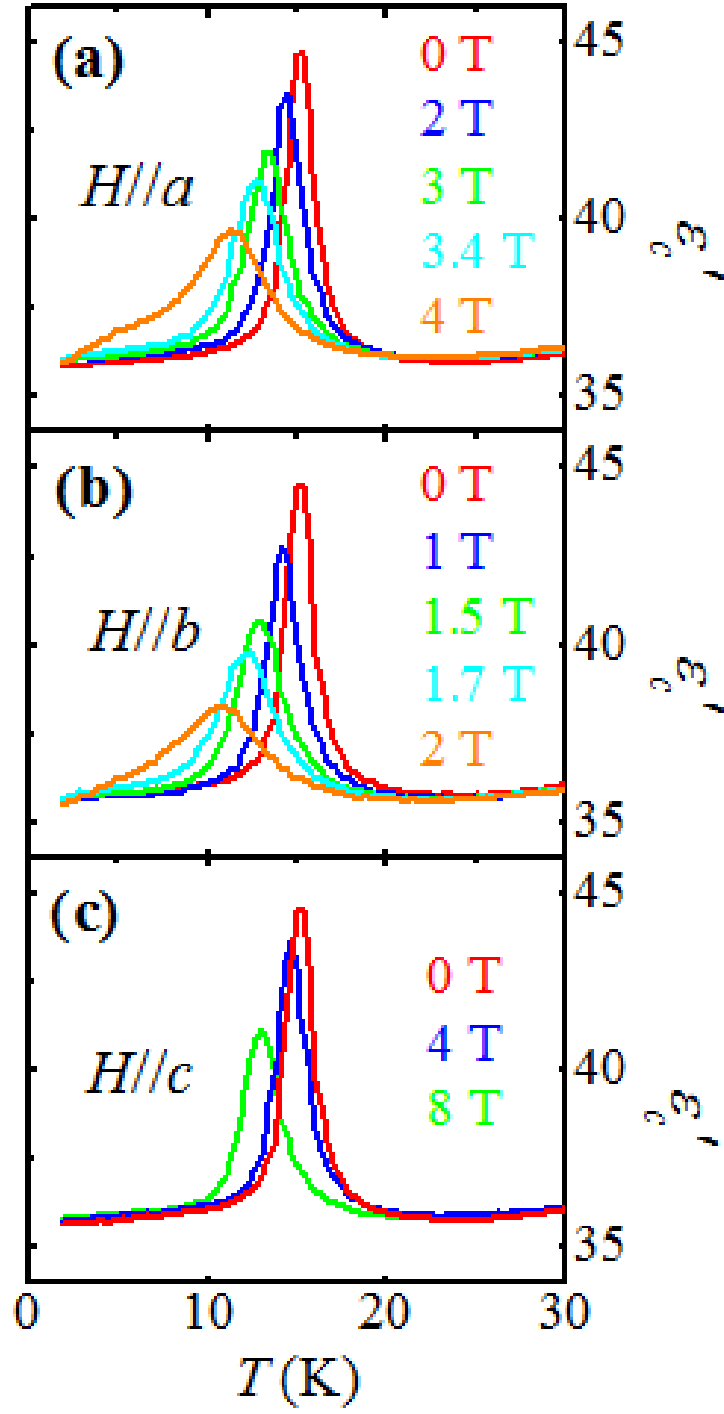


FIG. II. 11 Temperature dependences of the dielectric constants (a-c) in various applied magnetic fields.

interactions can produce zero or non-zero electric polarization along the  $a$  and  $c$  axis, respectively. The  $k=0.5$  state appears to be an exception for which the  $P_a=0$  state is absent, because centric SDW would imply zero Mn spin for half of the Mn ions. However, even for  $k=0.5$ , states with both zero and non-zero  $P_c$  are possible, as illustrated in FIG. II. 8. The presence of two coexisting mechanisms producing different directions of  $\mathbf{P}$  may open new possibilities for magnetoelectric control, and should lead to previously unobserved phenomena. In our samples, only one mechanism (Ho-Mn) leads to FE. However, some of the previously studied polycrystalline o-HoMnO<sub>3</sub> samples [12] enter the  $k=0.5$  state at  $T=T_L$  which is larger than  $T_{Ho}$ , and significant  $\mathbf{P}$  is observed for  $T_{Ho}<T<T_L$ . A large increase of  $\mathbf{P}$  at  $T_{Ho}$  is also present in these samples. For these samples, our model predicts that the polarization is initially along the  $a$  axis, and that a large  $c$ -axis component develops in addition with decreasing  $T$ . Thus, we expect that the *direction* of  $\mathbf{P}$  changes with  $T$  in the  $k=0.5$  crystals. The reason for the variation of the exact magnitude and  $T$  dependence of  $\mathbf{P}$  and (in)commensurability among published results in polycrystalline specimens [11, 12] and our crystal data is currently unclear, but the presence of defects or residual strains may play an important role. To verify the intriguing possibility of temperature-induced rotation of the  $\mathbf{P}$ , preparation of such  $k=0.5$  crystals is certainly desirable.

In summary, we report first studies of single-crystalline o-HoMnO<sub>3</sub>, which is currently considered a prototype  $E$ -type multiferroic with symmetric exchange-striction mechanism. Contrary to the current belief, the ferroelectric polarization in our crystals is along the  $c$  axis. We argue that Mn-Mn and Ho-Mn exchange striction mechanisms

coexist in this system. These mechanisms can lead to both ferroelectric and antiferroelectric orders along the  $a$  axis (Mn-Mn), and the  $c$  axis (Ho-Mn). In our samples, the Ho-Mn interaction produces the  $c$ -axis polarization, while the Mn-Mn exchange striction induces the  $a$ -axis antiferroelectric order. We also propose that under certain conditions, these coexisting mechanisms should lead to temperature-induced rotation of FE polarization in the  $E$ -type manganites.

#### 4. REFERENCES

- [1] W. Eerenstein, *et al.*, Nature 442, 759 (2006).
- [2] S.-W. Cheong, *et al.*, Nat. Mater. 6, 13 (2007).
- [3] N. Hur, *et al.*, Nature 429, 392 (2004).
- [4] Y. J. Choi, *et al.*, Phys. Rev. Lett. 100, 047601 (2008).
- [5] I. Sergienko, *et al.*, Phys. Rev. Lett. 97 (2006).
- [6] P. Silvia, *et al.*, Journal of Physics: Condensed Matter 20, 434208 (2008).
- [7] K. Yamauchi, *et al.*, Phys. Rev. B 78 (2008).
- [8] S. Ishiwata, *et al.*, Phys. Rev. B 81 (2010).
- [9] B. Lorenz, *et al.*, Phys. Rev. B 76 (2007).
- [10] S. M. Feng, *et al.*, New Journal of Physics 12, 073006 (2010).
- [11] H. Brinks, *et al.*, Phys. Rev. B 63 (2001).
- [12] A. Muñoz, *et al.*, Inorganic Chemistry 40, 1020 (2001).
- [13] L. C. Chapon, *et al.*, Phys. Rev. Lett. 96, 097601 (2006).
- [14] Y. Tokunaga, *et al.*, Nat. Mater. 8, 558 (2009).

- [15] S. Alessandro, *et al.*, New Journal of Physics 12, 093026 (2010).
- [16] N. Aliouane, *et al.*, Journal of Physics: Condensed Matter 20, 434215 (2008).
- [17] M. Mochizuki, *et al.*, Phys. Rev. Lett. 105, 037205 (2010).

## **Chapter III**

### **Tunable Large Ferroelectric Polarization in a Magnetism-Driven Ferroelectric**

## 1. Introduction

Multiferroics are fascinating materials where multiple orders out of ferroelectricity, ferroelasticity and magnetism coexist and are coupled [1]. A significant fraction of the current research is focused on magnetism-driven ferroelectrics where the presence of competing interactions and/or magnetic frustration induces an antiferromagnetic order with broken space inversion symmetry that allows ferroelectricity to develop. Both symmetric and antisymmetric parts of the magnetic exchange coupling can be coupled to the polar distortions. Antisymmetric exchange interaction is active in cycloidal-magnetic multiferroics such as  $\text{LiCu}_2\text{O}_2$  and  $\text{TbMnO}_3$  [2-4] while multiferroicity in  $\text{Ca}_3\text{CoMnO}_6$  and  $\text{TbMn}_2\text{O}_5$  [5, 6] systems primarily from symmetric exchange interaction. The ferroelectric polarization ( $P$ ) in magnetism-driven ferroelectrics turns out to be minuscule, compared with that of the typical ferroelectrics such as  $\text{BaTiO}_3$  ( $P \sim 2 \times 10^5 \mu\text{C}/\text{m}^2$ ). For example, polarization values of  $\text{LiCu}_2\text{O}_2$ ,  $\text{TbMnO}_3$ ,  $\text{Ca}_3\text{CoMnO}_6$ , and  $\text{TbMn}_2\text{O}_5$  are  $4 \mu\text{C}/\text{m}^2$ ,  $800 \mu\text{C}/\text{m}^2$ ,  $90 \mu\text{C}/\text{m}^2$ , and  $400 \mu\text{C}/\text{m}^2$ , respectively. Thus, one of the pressing challenges of the research on magnetism-driven multiferroics is finding systems or means to enhance the magnitude of polarization. In  $\text{GdFeO}_3$  and orthorhombic  $\text{HoMnO}_3$  [7-9], the symmetric exchange interaction between rare-earth and transition metal ions plays an essential role in producing large polarization ( $\sim 1,500 \mu\text{C}/\text{m}^2$ ). The strong coupling between structural distortions and magnetic order can in principle also lead to a large variation of the electric polarization under the application of magnetic fields. However, in known materials to date, the effect of strong magnetic fields is either to rotate tiny  $P$  by  $90^\circ$  in cycloidal-multiferroics [10, 11] or induce only a small variation of  $P$  in symmetric exchange-striction compounds [6]. In

the course of studying systematically the multiferroic properties of  $\text{RE}\text{Mn}_2\text{O}_5$  (RE=rare earths such as Gd, Tb, ..., Lu and Y), we discovered that  $\text{GdMn}_2\text{O}_5$  exhibits an electrical polarization of unprecedented magnitude  $P=3,600 \text{ } \mu\text{C}/\text{m}^2$ . Furthermore, applying magnetic fields induces a giant change of  $P$  by  $5,000 \text{ } \mu\text{C}/\text{m}^2$  which is the largest among the known multiferroic systems.

It is very essential to obtain the complete magnetic structure of the system to investigate the origin of large  $P$  as well as the remarkable variation of  $P$  under the magnetic fields. Several x-ray resonant diffraction studies have been performed in the past few years [12-15], which have improved the knowledge of many complex magnetic systems by taking advantage of the element selective property to investigate e.g. RE ions or by refining usually small but important details of the magnetic structure configurations. However, the experimental difficulties to collect a large amount of data and properly correct them in order to refine the lots of parameters prohibit constructing full complex magnetic structure. In our experiment, combining the data collected in-resonance at the Gd  $L_{III}$ -edge and off-resonance enables us to complete magnetic phase diagram of  $\text{GdMn}_2\text{O}_5$  entirely with x-ray magnetic scattering.

In this paper, we present our finding of a large ferroelectric polarization in  $\text{GdMn}_2\text{O}_5$  along the  $b$  axis ( $P_b$ ), as large as  $3,600 \text{ } \mu\text{C}/\text{m}^2$  and the significant reversible tuning of  $P_b$  ( $\Delta P_b \approx 5,000 \text{ } \mu\text{C}/\text{m}^2$ ) by applying external magnetic fields along the  $a$  axis ( $H_a$ ), which is the largest magnitude reported so far in magnetism-driven ferroelectrics. Based on x-ray magnetic scattering data, we model the complete magnetic structure of

both Gd and Mn moments in the ferroelectric state. We propose a magnetoelectric coupling scheme where the large ferroelectric polarization originates predominantly from the Gd-Mn nearly-symmetric exchange striction rather than the known mechanism of Mn-Mn exchange striction in the related compounds.

## 2. Experimental Method

The single crystals of  $\text{GdMn}_2\text{O}_5$  with an orthorhombic structure (centrosymmetric space group,  $Pbam$ ) were grown utilizing a conventional  $\text{B}_2\text{O}_3/\text{PbO}/\text{PbF}_2$  flux method [16]. Magnetization ( $M$ ) was measured with a SQUID magnetometer.  $P$  and dielectric constant ( $\epsilon$ ) were obtained by integrating pyroelectric current measured with an electrometer and using an LCR meter at  $f=44$  kHz, respectively. The x-ray magnetic scattering data was collected at the I16 beamline (Diamond Light Source Ltd.) [17, 18].

In  $\text{GdMn}_2\text{O}_5$ ,  $\text{Mn}^{4+}$  ions occupy oxygen octahedra, whereas  $\text{Mn}^{3+}$  ions are in oxygen square-pyramids, and they form zigzag antiferromagnetic chain modulating along the  $a$  axis with spins parallel within each chain and tilted by about  $15^\circ$  with respect to the  $a$  axis. From the x-ray magnetic scattering data, we found that Mn spins exhibit an incommensurate order with wave-vector  $\mathbf{k}=(0.486,0,0.18)$  below  $T_{N1}\approx 40$  K, followed by a lock-in to the commensurate order with  $\mathbf{k}=(0.5,0,0)$  below  $T_{N2}\approx 33$  K. We note that in contrast with other  $\text{REMn}_2\text{O}_5$  (RE=Tb, Dy, Ho, Er, and Tm) compounds in which the ordering of rare earth moments occurs at low temperatures ( $\sim 5$  K) [13, 19],  $\text{GdMn}_2\text{O}_5$  exhibits Gd spin order spontaneously at the temperature where Mn spins lock in, i.e. at  $T_{N2}\approx 33$  K.



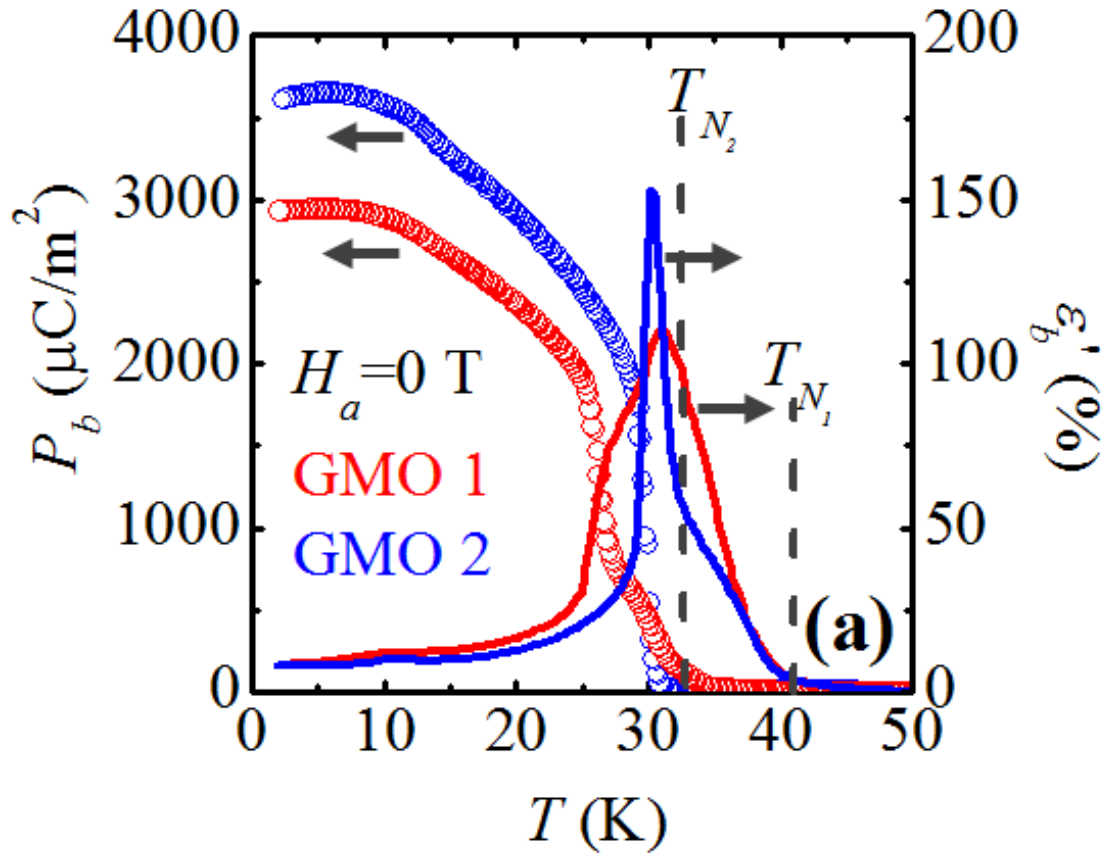


FIG. III. 1. Temperature dependences of electric polarizations and dielectric constants along the  $b$  axis under zero magnetic field for GMO 1 (red) and GMO 2 (blue).

### 3. Result and Discussion

The temperature dependence of  $P_b$ 's in zero magnetic field for two different crystals (GMO1 and GMO2) was measured. The onset of  $P_b$  for both appears at  $T_{N2} \approx 33$  K where the commensurate order of Mn spins occurs (FIG. III. 1.), and the magnitude of  $P_b$  in GMO 2 reaches to  $3,600 \mu\text{C}/\text{m}^2$  at 2 K. We emphasize that the observed ferroelectric polarization of  $\text{GdMn}_2\text{O}_5$  is the largest in magnitude among those of  $\text{REMn}_2\text{O}_5$  with other RE and, in fact, those of all magnetism-induced ferroelectrics discovered so far. In GMO 2,  $\epsilon'_b$  starts to increase with a shoulder-like feature below 40 K followed by the pronounced sharp peak near  $T_{N2}$ , consistent with the rapid growth of  $P_b$ . With lowering temperature further,  $P_b$  increases broadly with getting the magnitude about two times larger at the lowest temperature. On the other hand, GMO 1 shows two-step-like increase of  $P_b$  below  $T_{N2}$  with smaller magnitude of  $P_b$  at 2 K and a broader anomaly in  $\epsilon'_b$ . Since the commensurate order of both Gd and Mn does not change below  $T_{N2}$ , the extensive growths of  $P_b$  with decreasing the temperature for both samples and the second step of  $P_b$  at  $\sim 26$  K in GMO 1 may originate from the pinned magnetoelectric domains with  $P$  opposite to the poling electric field. FIG. III. 2. displays the magnetic field dependence of  $P_b$  measured at 2 K on GMO 1. The sample was prepared by poling in  $E_b \approx 10$  kV/cm and  $H_a = 0$  T. Upon increasing  $H_a$  from 0 T,  $P_b$  tends to decrease until it suddenly reverses at  $\sim 4.7$  T. The magnitude of  $P_b$  reaches to  $-2,000 \mu\text{C}/\text{m}^2$  above the transition. Thus, the drastic change of  $P_b$  induced by the external magnetic field is of the order of  $\Delta P_b \approx 5,000 \mu\text{C}/\text{m}^2$ . Upon decreasing  $H_a$  from 9 T,  $P_b$  exhibits large magnetic hysteresis and does not recover the initial value at zero magnetic field, possibly due to the creation of multiple

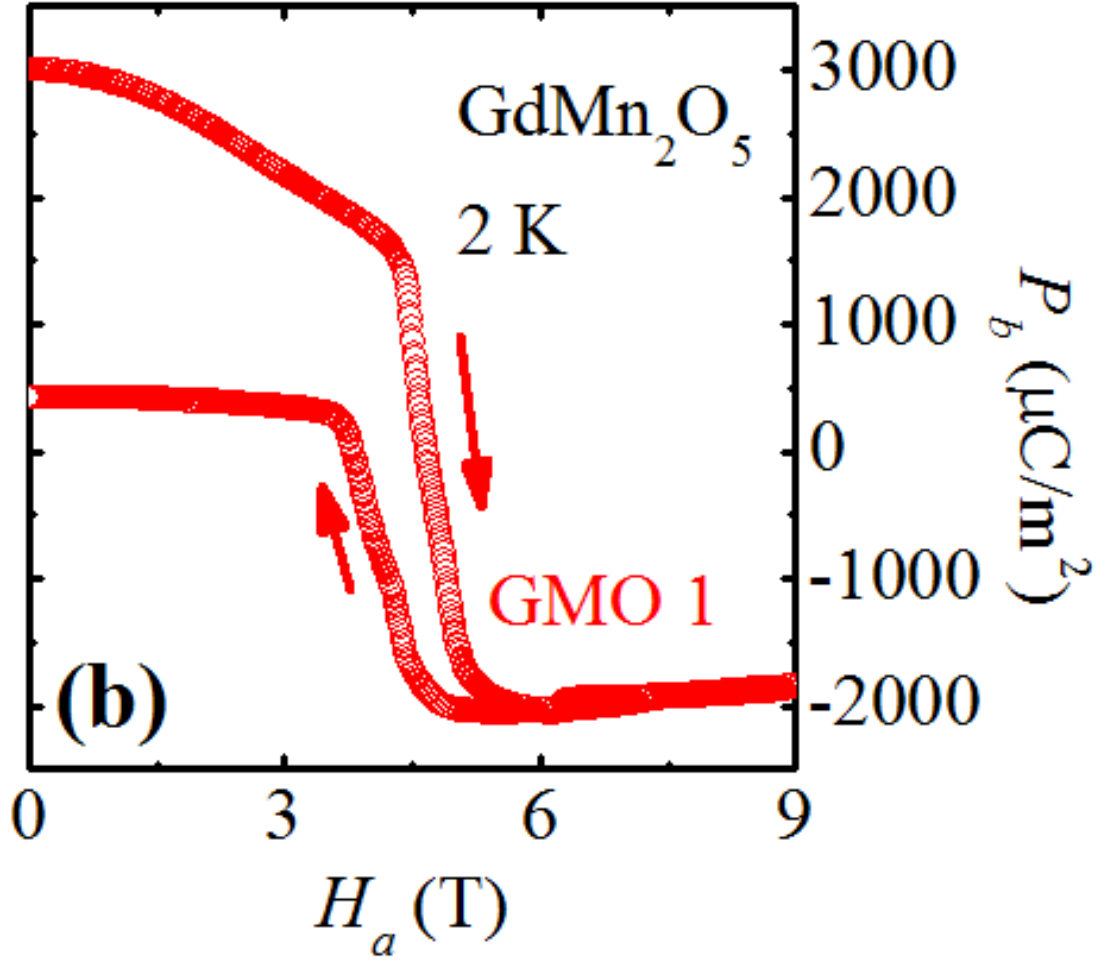


FIG. III. 2.  $H_a$  dependence of  $P_b$  at 2 K, where  $H_a$  was swept from 0 T to 9 T, then back to 0 T after poling in  $E_b \approx 10$  kV/cm, for GMO 1.

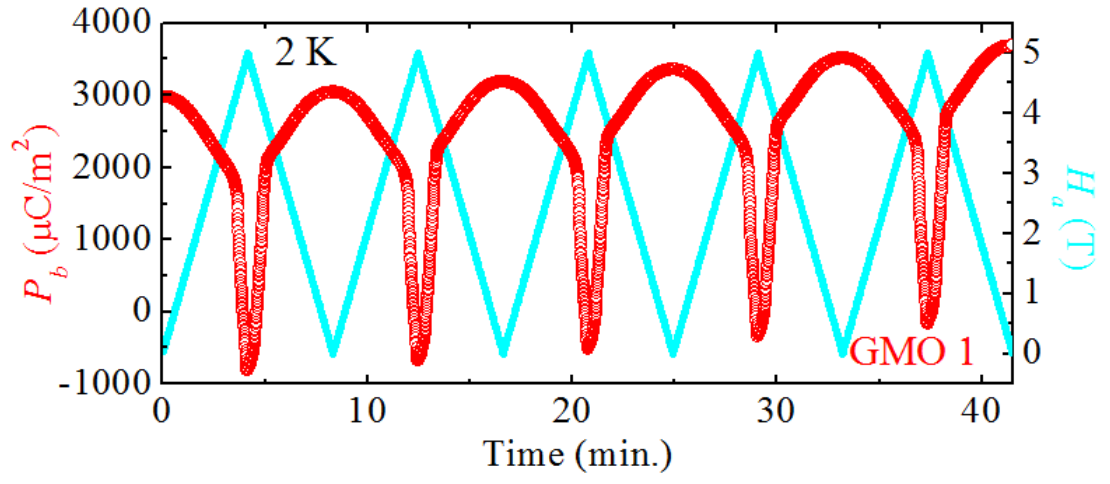


FIG. III. 3. Repeated variation of  $P_b$  (red circles) at 2K under the application of  $H_a$  (light blue lines) for GMO 1.  $H_a$  was varied linearly between 0 and 5 T.

magnetoelectric domains with the opposite  $P$ . We also achieved the repeated variation of  $P_b$  by changing  $H_a$  linearly between 0 and 5 T at 2 K as shown in FIG. III. 3. The magnetic field of 5 T was chosen to minimize the magnetic hysteresis and maximize the variation of ferroelectric polarization during repetition. The sequential flipping of the polarization continues without significant decay and the abundant change of ferroelectric polarization induced by the magnetic field persists.

Detailed measurements of magnetic and dielectric properties were performed on GMO 1. The temperature and magnetic field dependences of magnetization are shown in FIGs. III. 4. and 5. The anomalies corresponding to 33 K and 26 K are clearly shown in the temperature derivative of magnetization along the  $a$  axis ( $M_a$ ) in the inset in FIG. III. 4. The isothermal  $M_a$  at 2 K displays spin-flop transitions at around 5 T in accordance with the reversal of  $P_b$ . The temperature dependences of  $P_b$  and  $\epsilon'_b$  under the various magnetic fields from 0 to 9 T were also measured. As shown in FIG. III. 6. (a),  $P_b$  tends to decrease in the overall range below  $T_{N2}$  under  $H_a$ . At 4.7 T where the spin-flop transition at 2 K occurs,  $P_b$  presents complicated temperature dependence and a slightly negative value at the lowest temperature. With further increase of  $H_a$ , the magnitude of the reversed  $P_b$  becomes escalated. Accompanied with the appearance of reversed  $P_b$ ,  $\epsilon'_b$  also exhibits an additional peak at 4.7 T below 20 K and the peak develops sharper and higher above 4.7 T. However, the main peak which corresponds to the onset of  $P_b$  at  $T_{N2}$  diminishes with increasing  $H_a$  and splits into two peaks near 4.7 T.

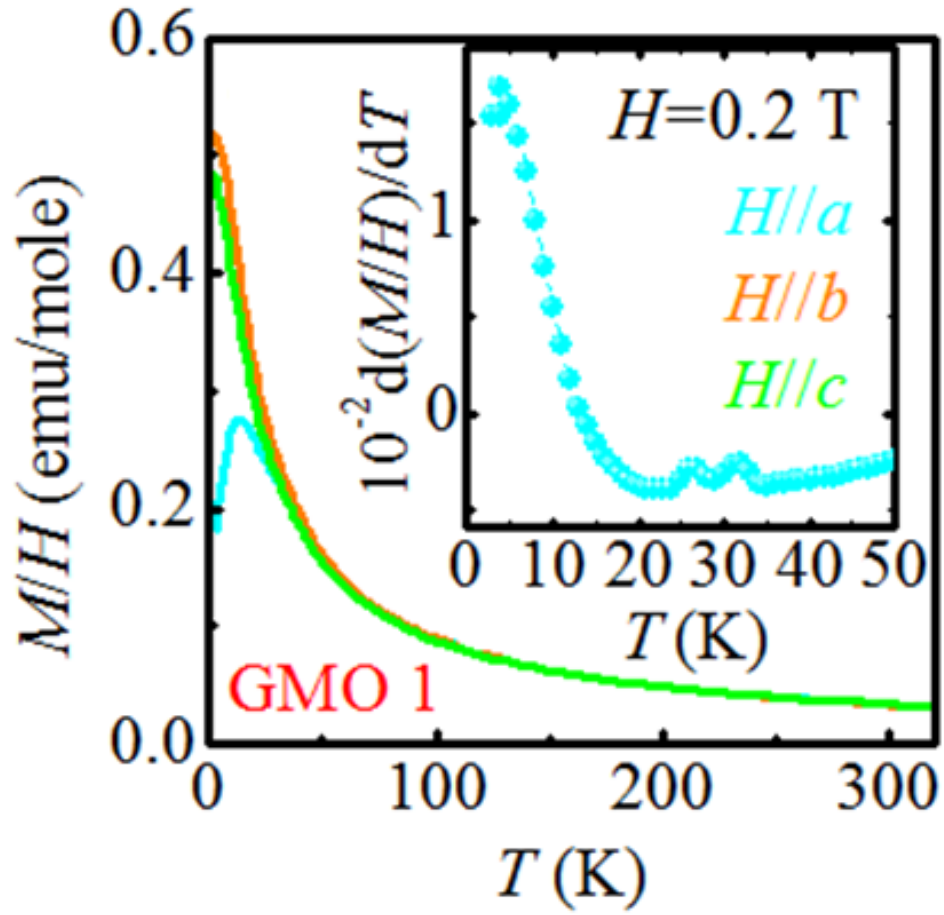


FIG. III. 4. Temperature dependence of magnetization along the three different crystallographic axes for  $H=0.2$  T. Inset shows the temperature derivative of the susceptibility along the  $a$ -axis.

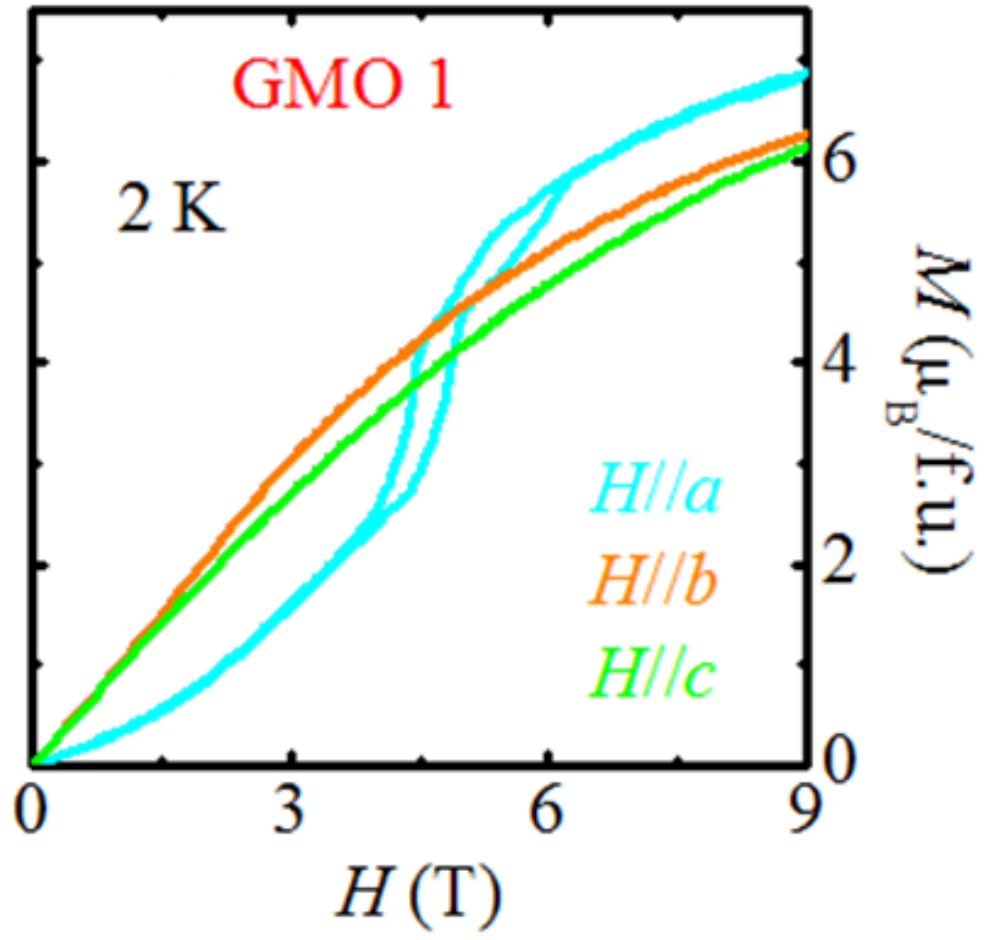


FIG. III. 5. Magnetic field dependence of magnetization along the  $a$ ,  $b$ , and  $c$  axes at 2 K.

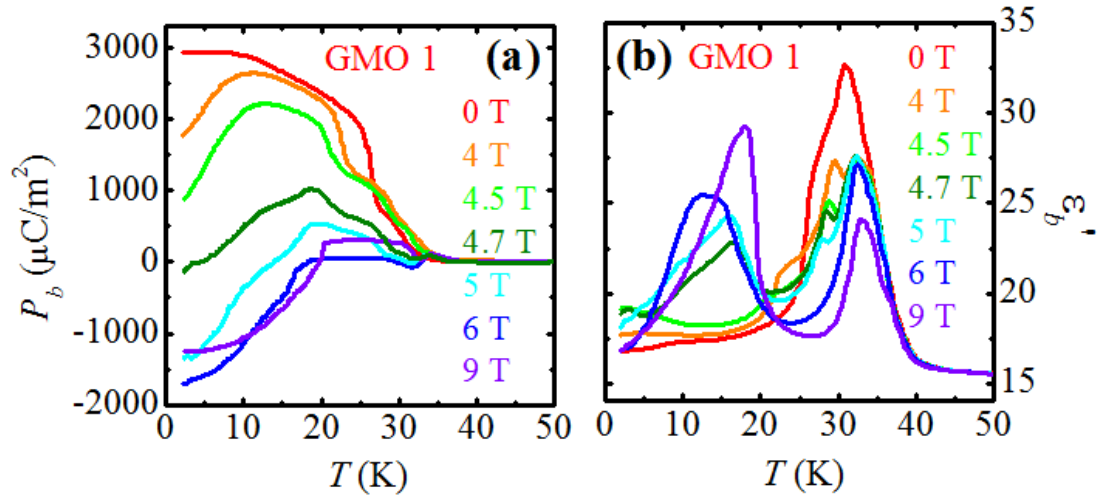


FIG. III. 6. Temperature vs.  $P_b$  (a) and  $\epsilon'_b$  (b) in various magnetic fields ( $H_a=0, 4, 4.5, 4.7, 5, 6$ , and  $9 \text{ T}$ ). All the data were obtained from GMO 1.



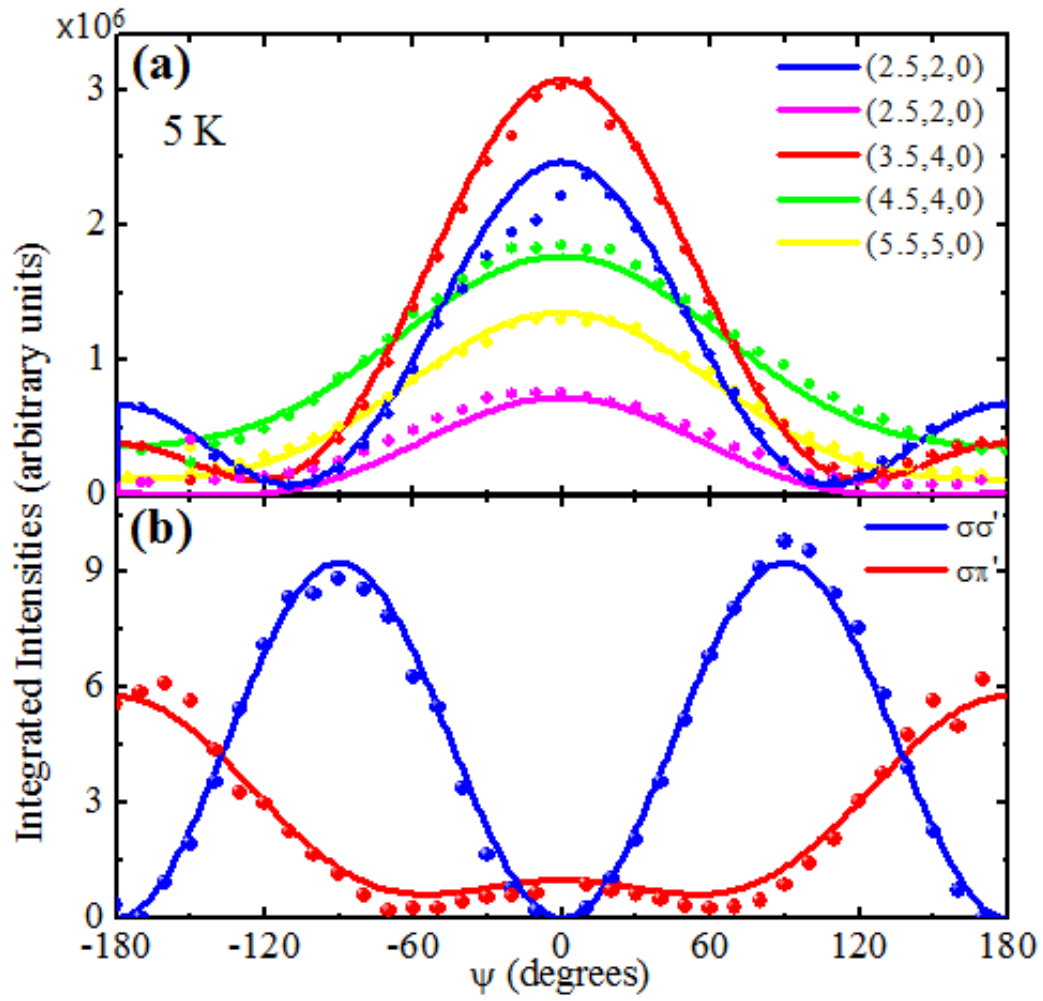


FIG. III. 7. Azimuthal dependence of the magnetic Bragg peak intensities at 5 K. The azimuth value is given with respect to a reference in the (1 0 0) direction. (a) Magnetic Bragg reflections at resonance (Gd *LIII* edge). The symbols containing the error bars show the experimental data points. The solid curves are fits to the data. (b) (2.5 3 0) reflection in non-resonant condition at 6.4 keV, in the  $\sigma\sigma'$  (blue) and  $\sigma\pi'$  (red) channels. Error bars are contained in the spot size.

The magnetic structure of  $\text{GdMn}_2\text{O}_5$  was studied by x-ray magnetic scattering, both off resonance and in resonant conditions (RMS) at the Gd  $L_{III}$  edge. The model for the magnetic structure of the Gd sublattice has been derived from the azimuthal dependence of five magnetic reflections measured in resonant conditions at 5 K. (FIG. III. 7.(a)) The Gd magnetic configuration and the magnetic symmetry were found by a least-square refinement of all azimuthal scans considered simultaneously. The complete magnetic structure, i.e. including the Mn magnetic ordering and the relative phase between Gd and Mn modulations, was probed using non-resonant magnetic scattering. (FIG. III. 7.(b)) Only a single off-resonant azimuthal scan could be collected in the full azimuthal range, preventing to perform an unconstrained refinement including all Mn moments. Instead, the magnetic configuration of the Mn in the  $ab$  plane was fixed to that found for other commensurate structure of the  $\text{RE}\text{Mn}_2\text{O}_5$  compounds. By including the Gd contribution derived from the RMS work, the off-resonance scans can be adequately fitted.

FIG. III. 8. displays the complete magnetic structure of  $\text{GdMn}_2\text{O}_5$  projected in the  $ab$  plane in the commensurate phase. The Gd moments are aligned almost ferromagnetically relative to the neighboring  $\text{Mn}^{3+}$  moments. It is now well accepted that in  $\text{RE}\text{Mn}_2\text{O}_5$  [1, 20, 21], the electric polarization originates from the symmetric exchange striction of Mn ions between nearly collinear Mn spins. The exchange striction is dominated by the spin-configuration of neighboring  $\text{Mn}^{3+}$ - $\text{Mn}^{4+}$  pair and generates an ionic ferroelectric polarization along the  $b$  axis whose sign is dictated by the repulsion and attraction of pairs of ions bearing anti-parallel and parallel spin configurations,

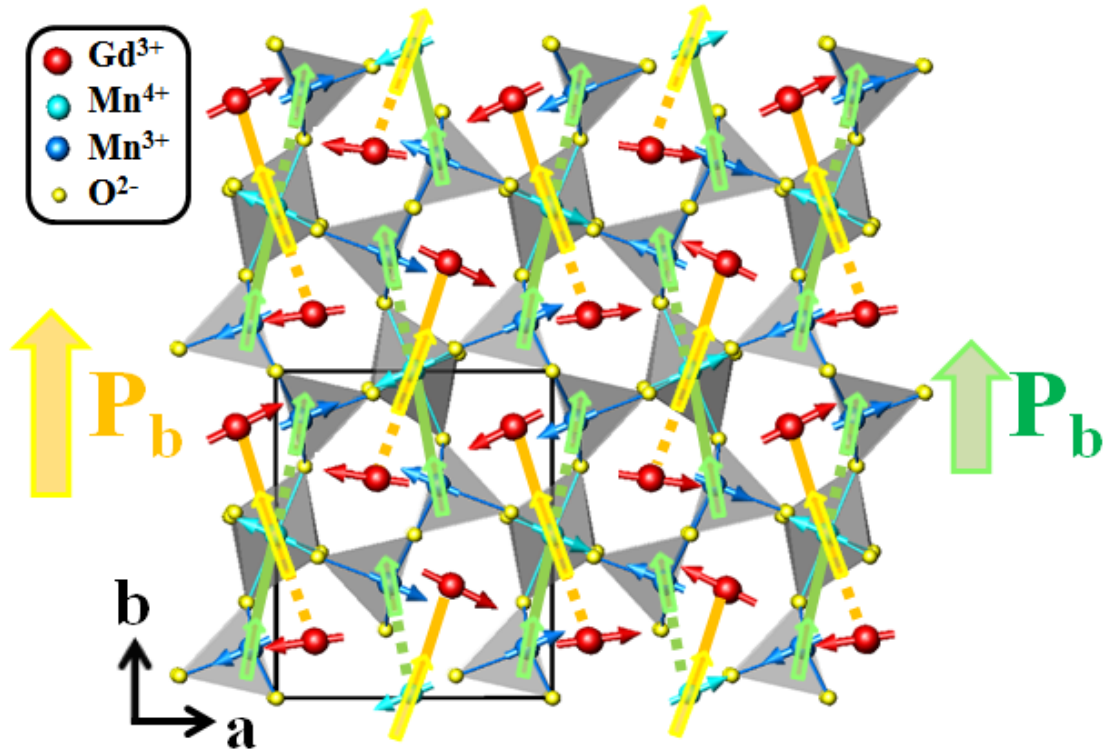


FIG. III. 8. In-plane crystallographic and magnetic structure of  $\text{GdMn}_2\text{O}_5$  with illustrating both  $\text{Gd}$  and  $\text{Mn}$  spins in the low temperature commensurate state. The solid and dotted lines indicate attractive and repulsive exchange interactions for  $\text{Gd}$ - $\text{Mn}$  (yellow) and  $\text{Mn}$ - $\text{Mn}$  (green), respectively. Open arrows reflect the directions of the ionic displacements corresponding to the macroscopic  $P_b$ .

respectively. In this case, the angle of  $\text{Mn}^{3+}\text{-O-Mn}^{4+} \sim 71^\circ$  which is close to  $90^\circ$  favors ferromagnetic arrangement within the pairs so that the parallel pairs ( $\text{Mn}^{3+}\text{-Mn}^{4+}$  spin pairs connected with green solid line in FIG. III. 8.) are brought closer to each other while the anti-parallel pairs ( $\text{Mn}^{3+}\text{-Mn}^{4+}$  spin pairs connected with green dotted line in FIG. III. 8.) tend to move away from each other. The resulting ferroelectric polarization is indicated in green arrows in FIG. III. 8.

However, the symmetric exchange striction between Mn pairs might not be singly responsible for the remarkable ferroelectricity in  $\text{GdMn}_2\text{O}_5$ . Note that the system such as  $\text{YMn}_2\text{O}_5$  where the ferroelectricity results mainly from the Mn-Mn exchange striction display a polarization of only  $1,000 \mu\text{C}/\text{m}^2$  which is less than one third of the one found in  $\text{GdMn}_2\text{O}_5$  [22]. The magnetic structure of  $\text{GdMn}_2\text{O}_5$  strongly suggests that the plausible explanation for the additional source of polarization lies in the symmetric exchange striction mechanism of Gd-Mn spin pairs in the commensurate phase. Note that the contributions of rare earth-transition metal interaction to the ferroelectricity have been known in some multiferroics such as the orthoferrite and orthorhombic  $\text{HoMnO}_3$ . In the case of  $\text{Gd}^{3+}\text{-Mn}^{4+}$  pairs, because of the bond angle of  $\text{Gd-O-Mn} \sim 140^\circ$ , anti-parallel arrangement of spins becomes more favorable assuming Goodenough-Kanamori rule would be valid. The attraction between antiparallel Gd-Mn pairs gives the distortion producing the ferroelectricity along the  $b$  axis (yellow arrow in FIG. III. 8.) as the same direction for the ferroelectric polarization induced by Mn-Mn exchange striction. The promoted ferroelectricity due to the distinct presence of Gd-Mn exchange-striction in  $\text{GdMn}_2\text{O}_5$  is originated from its simplest magnetic structure among  $\text{REMn}_2\text{O}_5$  series

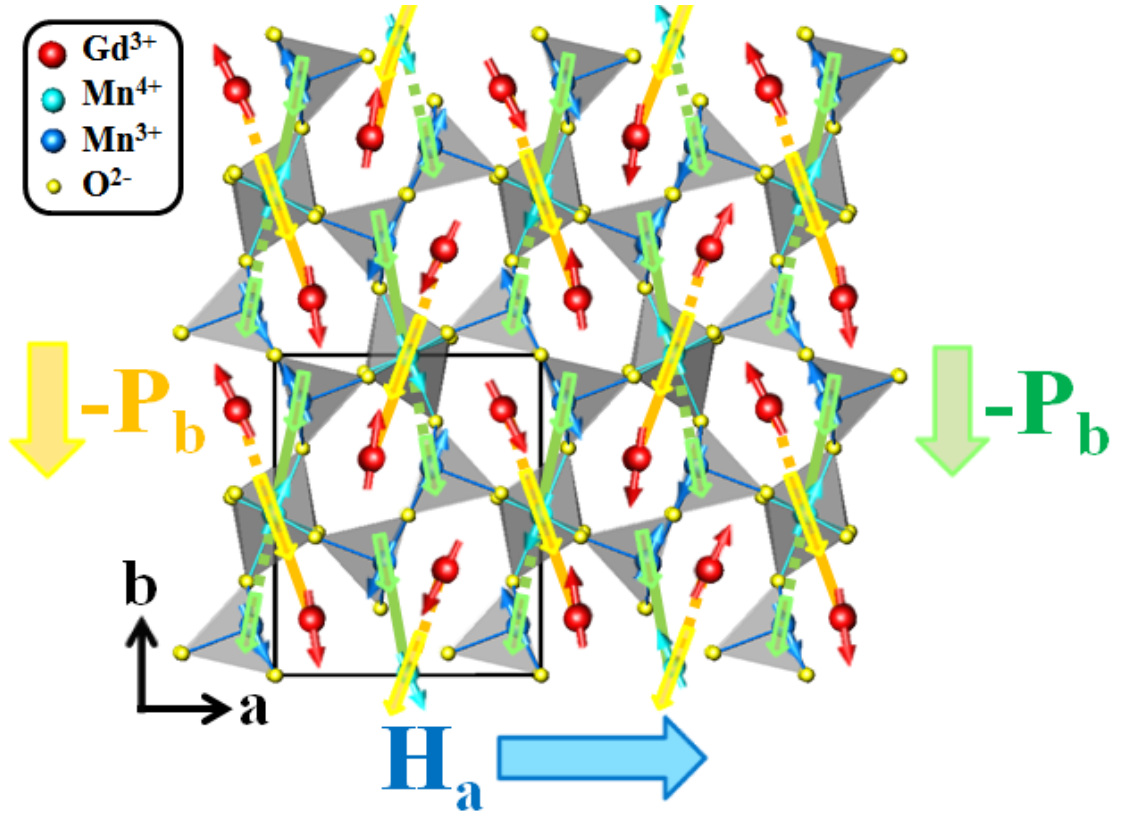


FIG. III. 9. In-plane spin structure regarding the reversed direction of  $P_b$  under the application of  $H_a$ .

below  $T_{N2}$ . From our investigation of the magnetic structure, along the  $a$  axis, the zigzag antiferromagnetic chains propagate with  $k_x=0.5$  like other  $\text{RE}\text{Mn}_2\text{O}_5$  compounds in the commensurate phase. In contrast with other compounds,  $\text{GdMn}_2\text{O}_5$  possesses the propagation vector of  $k_z=0$  which produces the ferromagnetic stacking along  $c$  axis. The dissimilar magnetic structure can be explained from the ionic size of  $\text{Gd}^{3+}$  slightly larger than other rare-earth in the series, which influences on the Mn exchange striction through the Gd layer.

The application of the magnetic fields along the easy axis,  $a$  axis, reverses the ferroelectric polarization. We offer the conceivable scenario on the reversal of ferroelectric polarization. In  $\text{BiMn}_2\text{O}_5$ , the spin-flop in the antiferromagnetic zigzag spin chain under the applied magnetic field is known to be responsible of the reversal of polarization [23, 24]. As shown in FIG. III. 9., upon applying  $H_a$ , both Gd and Mn spins rotate clockwise or counter-clockwise by  $90^\circ$  with respect to the initial orientations. This results in the conversion of the relative orientations of spin pairs (both Gd-Mn and Mn-Mn pairs), and therefore gives rise to the reversal of the ferroelectric polarization.

In summary, we have established that  $\text{GdMn}_2\text{O}_5$  displays the largest ferroelectric polarization in zero magnetic field and the largest variation of polarization in a magnetic field among the spin-driven ferroelectrics. Furthermore, the direction of the polarization can be repeatedly switched by an applied magnetic field. Based on the complete magnetic structure probed by x-ray resonant and off-resonant magnetic scattering, we argue that in addition to the Mn-Mn exchange striction mechanism, the Gd-Mn symmetric exchange

striction is primarily responsible for the observed large ferroelectric polarization.

#### 4. REFERENCES

- [1] D. I. Khomskii, J. Magn. Magn. Mater. **306**, 1 (2006).
- [2] S-W. Cheong and M. Mostovoy, Nature Mater. **6**, 13 (2007).
- [3] N. Hur *et al.*, Nature **429**, 392 (2004).
- [4] T. Goto *et al.*, Phys. Rev. Lett. **92**, 257201 (2004).
- [5] N. Hur *et al.*, Phys. Rev. Lett. **93**, 107207 (2004).
- [6] T. Kimura *et al.*, Nature **426**, 55 (2003).
- [7] G. Lawes *et al.*, Phys. Rev. Lett. **95**, 087205 (2005).
- [8] T. Kimura *et al.*, Phys. Rev. B **73**, 220401(R) (2006).
- [9] T. Kimura *et al.*, Phys. Rev. Lett. **94**, 137201 (2005).
- [10] Y. Yamasaki *et al.*, Phys. Rev. Lett. **96**, 207204 (2006).
- [11] K. Taniguchi *et al.*, Phys. Rev. Lett. **97**, 097203 (2006).
- [12] S. Park *et al.*, Phys. Rev. Lett. **98**, 057601 (2007).
- [13] H. Katsura *et al.*, Phys. Rev. Lett. **95**, 057205 (2005).
- [14] M. Mostovoy, Phys. Rev. Lett. **96**, 067601 (2006).
- [15] I.A. Sergienko, and E. Dagotto, Phys. Rev. B **73**, 094434 (2006).
- [16] A. B. Harris *et al.*, Phys. Rev. B **73**, 184433 (2006).
- [17] L. C. Chapon *et al.*, Phys. Rev. Lett. **96**, 097601 (2006).
- [18] Y. Noda *et al.*, Physica B **385-386**, 119 (2006).
- [19] H. Kimura *et al.*, J. Phys. Soc. Jpn. **75**, 113701-1 (2006).
- [20] I. A. Sergienko *et al.*, Phys. Rev. Lett. **97**, 227204 (2006).

- [21] B. Lorentz *et al.*, Phys. Rev. B **76**, 104405 (2007).
- [22] M. E. Fisher and W. Selke, Phys. Rev. Lett. **44**, 1502 (1980).
- [23] S. Rayaprol *et al.*, Sol. Stat. Comm. **128**, 79 (2003).
- [24] V. G. Zubkov *et al.*, J. of Sol. Stat. Chem. **160**, 293 (2001).
- [25] A. Maignan *et al.*, Eur. Phys. J. B, **15**, 657 (2000).
- [26] J. Rodriguez-Carvajal, Physica B **192**, 55 (1993).
- [27] J. A. Mydosh, *Spin Glasses. An Experimental Introduction*. (Taylor & Francis, London, 1993).
- [28] X. Yao and V. C. Lo, J. Appl. Phys. **104**, 083919 (2008).
- [29] Y. J. Jo *et al.*, Phys. Rev. B **79**(1), 012407 (2009).



## **Chapter IV**

## **Conclusion**

## 1. Summary

The recent discoveries of multiferroics and the origins of ferroelectricity driven by particular types of spin arrangements, have been extensively discussed in chapter I. A few examples were presented regarding the mechanisms of symmetric and anti-symmetric exchange strictions which result in ferroelectricity. Also, new trend of studies on multiferroics were introduced, such as the realization of a cross-control effect by utilizing ferromagnetic-ferroelectric phase coexistence and the observation of multiferroic vortex-antivortex networks extending to large-scale domain structures in hexagonal manganites.

In chapter II, a new multiferroic, single-crystalline orthorhombic-perovskite  $\text{HoMnO}_3$  was investigated. The larger rod-like single crystals of the orthorhombic  $\text{HoMnO}_3$  were first grown by the flux method in an ambient pressure, which is a significant progress because the ambient pressure during the growth usually stabilizes only hexagonal phase of  $\text{HoMnO}_3$ . The grown crystals with incommensurate E-type magnetic structure exhibit much large ferroelectric polarization than that observed in polycrystalline samples. The onset of polarization appears to be below Ho ordering temperature and the direction of polarization is found to be along the  $c$ -axis, completely different from the theoretical expectations. From the analysis, the polarization along the  $c$ -axis can be explained by the new emerging mechanism of Ho-Mn exchange striction and the loss of polarization along the  $a$ -axis due to Mn-Mn exchange striction can be validated with the antiferroelectric order described in the incommensurate spin state. Thus, the realization of a crystal possessing the commensurate E-type spin order may

lead to the intricate switching of direction of ferroelectric polarization triggered by the temperature variation.

In chapter III, the new discovery of tunable giant ferroelectric polarization in the multiferroic  $\text{GdMn}_2\text{O}_5$  has been presented. The ferroelectric polarization along the  $b$ -axis is found to be the largest and be varied repeatedly with the largest change by applying external magnetic fields along the  $a$ -axis among the spin-driven ferroelectrics known to date. In addition, contrary to the known origin for ferroelectricity in  $\text{REMn}_2\text{O}_5$ , the Mn-Mn exchange striction mechanism, the complete magnetic structure constructed by the x-ray resonant scattering experiment elucidate the large ferroelectricity in  $\text{GdMn}_2\text{O}_5$  originates mostly from the Gd-Mn symmetric exchange striction. The result supplies the new route to enhance the magnitude and tenability of ferroelectric polarization in multiferroics.

## 2. Prospect of multiferroics research

Despite the great achievement made on the multiferroics research so far, there still exist some difficulties in utilizing the extraordinary effect of magnetoelectric couplings in multiferroics directly to the true device applications. The main hurdles for practical operations lie in a very low working temperature of magnetoelectric controls of magnetic and dielectric properties, a relatively small magnitude of ferroelectric polarization compared to the conventional ferroelectric materials, and so on.

Lately, the Z-type hexaferrite,  $\text{Sr}_3\text{Co}_2\text{Fe}_{24}\text{O}_{41}$  has shown the possibility to overcome such problems [1]. Hexaferrites are iron oxides with the hexagonal structure and form in a number of different types relying on their chemical formula and structures

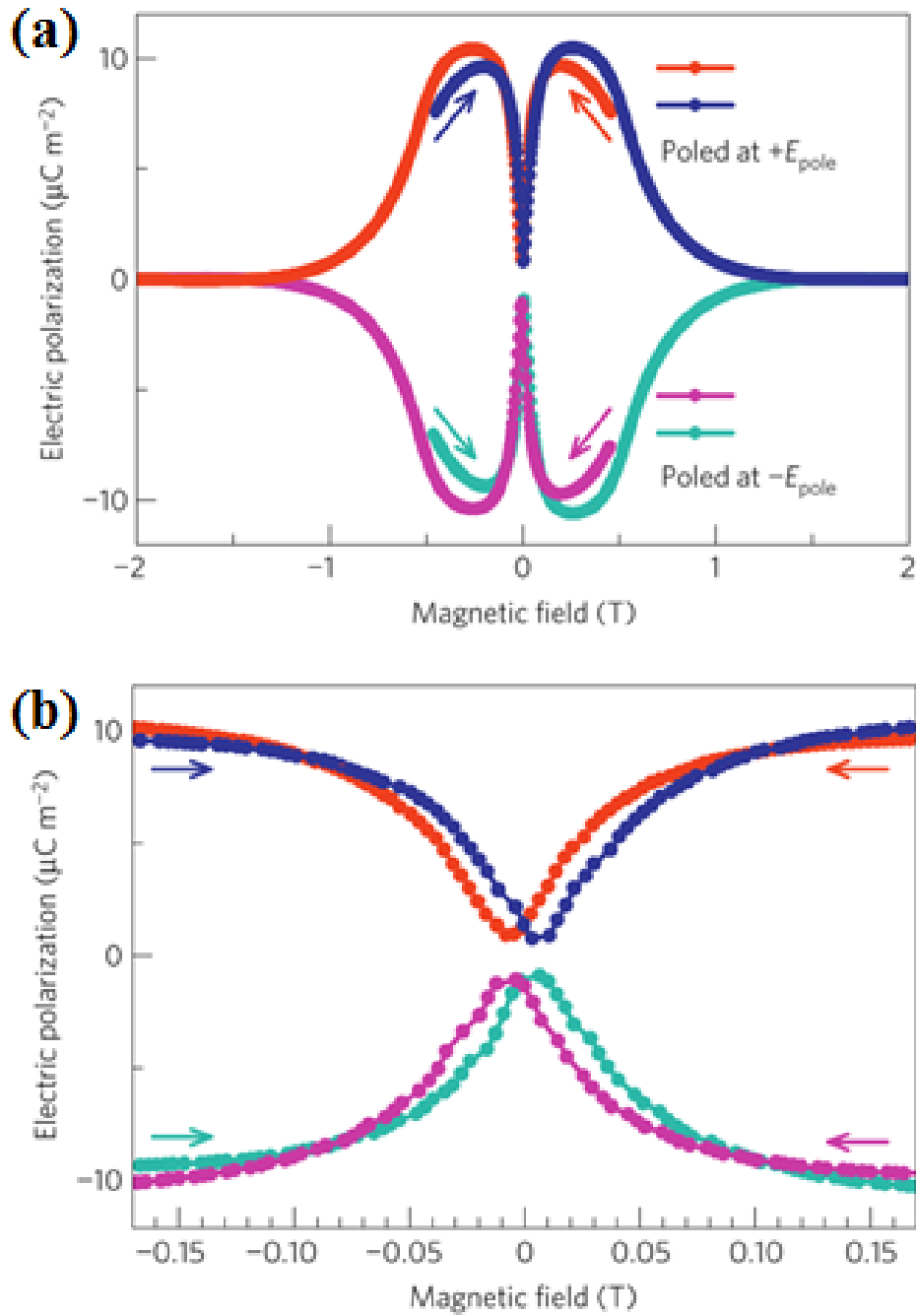


FIG. IV. 1. Room-temperature magnetoelectric effect of  $\text{Sr}_3\text{Co}_2\text{Fe}_{24}\text{O}_{41}$  ceramics sintered in oxygen. (a) Magnetic field dependence of electric polarization at 300 K. (b) Expanded views of a portion of (a). These data show effects of the sign of the poling electric field and that of magnetic field on the magnetoelectric signals [1].

[2]. Y-type Hexaferrites, such as  $(\text{Ba,Sr})_2\text{Zn}_2\text{Fe}_{12}\text{O}_{22}$  and  $\text{Ba}_2\text{Mg}_2\text{Fe}_{12}\text{O}_{22}$ , are the magnetic-field-induced ferroelectrics [3, 4]. The multiferroic transition temperatures of these Y-type hexaferrites are above room temperature, however, the control of dielectric properties by applying magnetic fields can be observed only at the temperatures below  $\sim 130$  K because of the considerable conduction at higher temperatures. Recently, Kitagawa *et al.* successfully synthesized the Z-type hexaferrite,  $\text{Sr}_3\text{Co}_2\text{Fe}_{24}\text{O}_{41}$  ceramics whose magnetic transition temperature is around  $\sim 670$  K. The sample sintered in oxygen shows very high resistivity which provides an optimum condition for accomplishing room-temperature magnetoelectric tunability. FIG. IV. 1. demonstrates the pronounced magnetoelectric coupling effect measured at 300 K. In spite of almost no spontaneous ferroelectric polarization in zero magnetic field, application of magnetic field leads to the electric polarization which reveals a maximum at 0.25~0.3 T, followed by the decrease and final disappearance at around 1 T. The result may present the possible application for magnetoelectric devices at room temperature.

Another tactic to achieve tunable room-temperature multiferroicity can be presented using interfacial co-play between ferromagnetic and ferroelectric thin films. The room-temperature multiferrocity has been demonstrated in the hetero-structural  $\text{Fe/BaTiO}_3$  and  $\text{Co/BaTiO}_3$  [5]. It appears that the spin-polarized transport can be controlled by switching the direction of ferroelectric polarization in  $\text{BaTiO}_3$ . The result is displayed in the measurement of tunneling magneto-resistance (TMR) in the  $\text{Fe/BTO/LSMO}$  and  $\text{Co/BTO/LSMO}$  tunnel junction through intricate interfacial correlation between magnetism and ferroelectricity. The element selective X-ray resonant magnetic scattering (XRMS) spectra also reveal a spontaneous magnetic moment in

BaTiO<sub>3</sub> with magnetically hysteric behavior. As shown in FIG. IV. 2., the ferromagnetic-like character of BaTiO<sub>3</sub> is observed by X-ray magnetic circular dichroism signals at selected energies as a function of the magnetic field. FIG. IV. 3. shows the out- of-plane piezoresponse of BaTiO<sub>3</sub> film as a function of the applied voltage. Therefore, BaTiO<sub>3</sub> in the heterostructure turns out to be the room-temperature multiferroic.

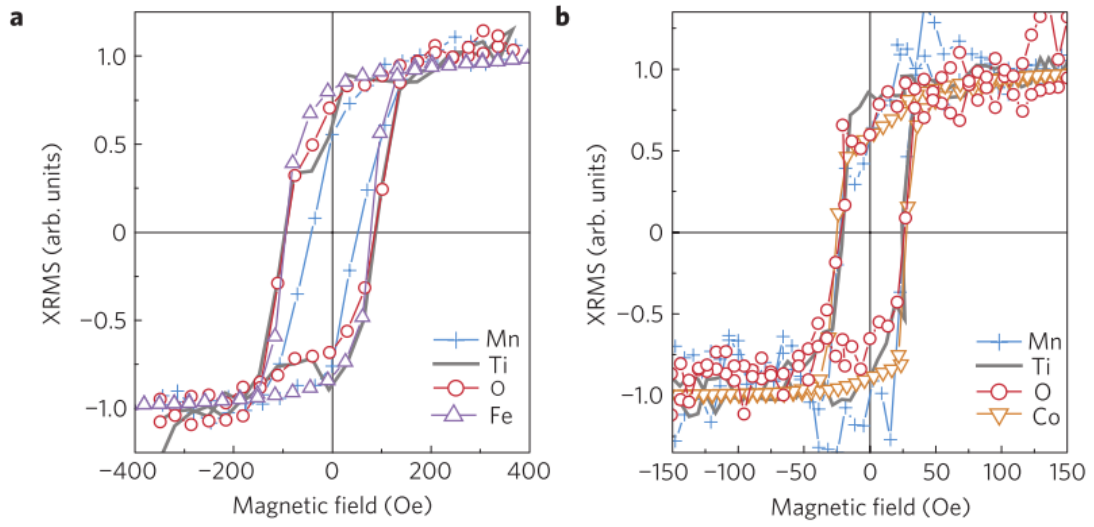


FIG. IV. 2. (a) XRMS versus magnetic field for Mn, Fe, Ti and O for the Fe/BTO sample measured at 300 K. (b) XRMS versus magnetic field for Mn, Co, Ti and O for the Co/BTO sample measured at 300 K.

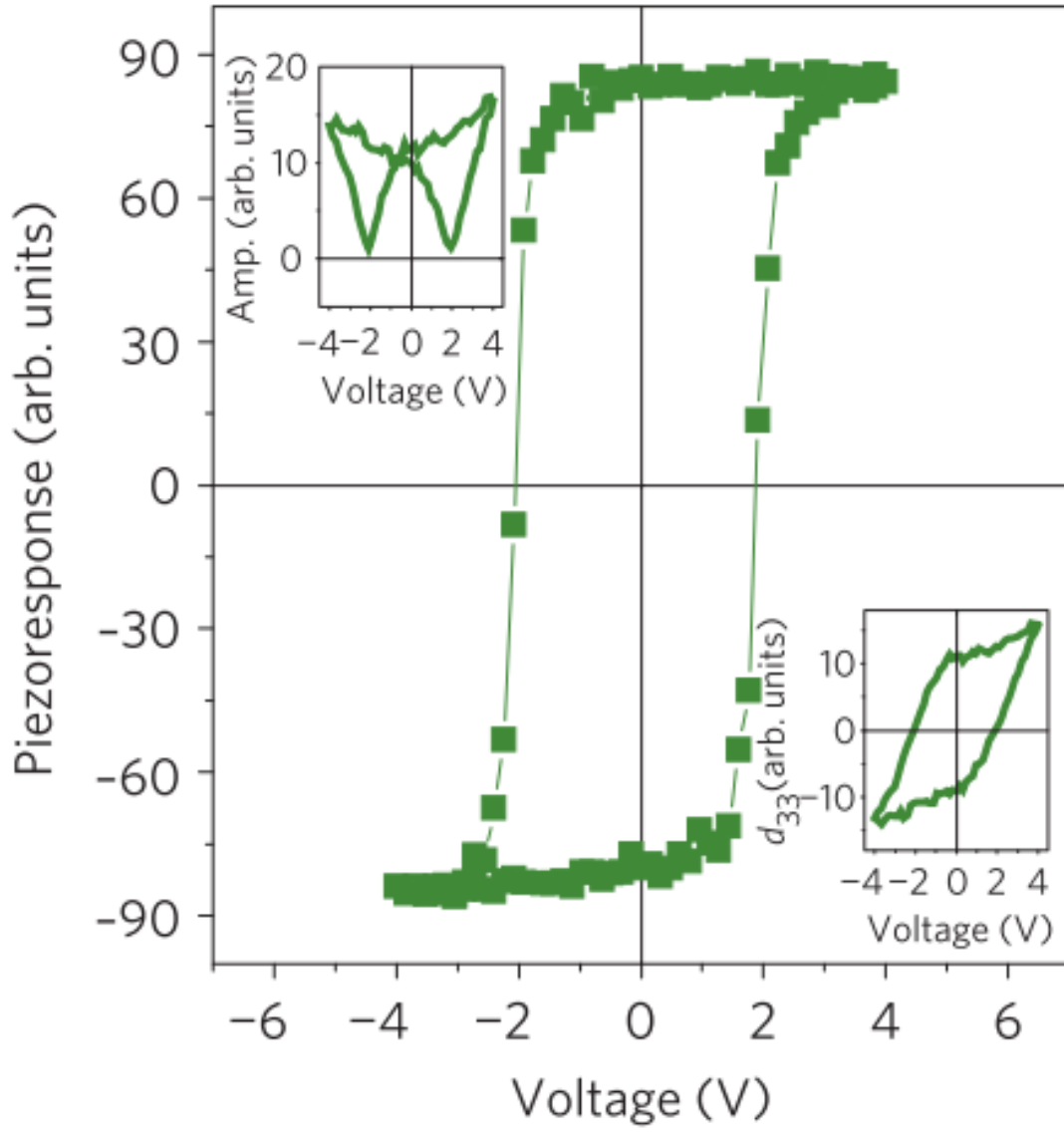


FIG. IV. 3. Out-of-plane piezoresponse phase loop of a BTO(1.2nm)/LSMO sample at 300 K. The corresponding amplitude and extracted piezoelectric coefficient ( $d_{33}$ ) data are shown in the insets.



### 3. REFERENCES

- [1] Y. Kitagawa, *et al.*, Nat Mater **9**, 797 (2010).
- [2] J. A. Kohn, *et al.*, Science **172**, 519 (1971).
- [3] S. Ishiwata, *et al.*, Science **319**, 1643 (2008).
- [4] S. H. Chun, *et al.*, Phys. Rev. Lett. **104** (2010).
- [5] S. Valencia, *et al.*, Nat Mater **10**, 753 (2011).

## Appendix I.

PRL **105**, 097201 (2010)

Selected for a Viewpoint in *Physics*  
PHYSICAL REVIEW LETTERS

week ending  
27 AUGUST 2010

### Cross-Control of Magnetization and Polarization by Electric and Magnetic Fields with Competing Multiferroic and Weak-Ferromagnetic Phases

Y. J. Choi, C. L. Zhang,\* N. Lee, and S.-W. Cheong

Rutgers Center for Emergent Materials and Department of Physics and Astronomy, Rutgers University,  
136 Frelinghuysen Road, Piscataway, New Jersey 08854, USA  
(Received 19 January 2010; published 23 August 2010)

From our investigation of magnetoelectric properties of a multiferroic phase in  $\text{Eu}_{0.75}\text{Y}_{0.25}\text{MnO}_3$  competing with a weak-ferromagnetic phase in magnetic fields, we found intriguing hysteretic behaviors of physical properties with variation of temperature and magnetic field. These hysteretic behaviors arise from the kinetic arrest (dearrest) processes of the first-order multiferroic-weak-ferromagnetic transition, resulting in frozen (melted) magnetoelectric glass states with coexisting two phases. Tipping the delicate balance of two competing phases by applying electric and magnetic fields leads to a remarkable control of magnetization and electric polarization.

DOI: 10.1103/PhysRevLett.105.097201

PACS numbers: 75.85.+t, 75.30.Kz, 77.80.-e

Coexistence of two or more distinct physical phases in complex materials, where various physical degrees of freedoms are intricately coupled and a number of order parameters are delicately balanced, is associated with a variety of unprecedented physical phenomena [1–3]. For instance, in perovskite manganites, the delicate balance between localization and hopping of charge carriers induces the competition of ferromagnetic (FM) metallic and antiferromagnetic (AFM) charge-ordered-insulating phases [1,4]. This competition can, in turn, lead to the coexistence of those two phases at low temperatures ( $T$ ), formed by kinetic arrest of the first-order AFM-insulating to FM-metallic transition [5–7]. The formation of the magnetic glass depends sensitively on external perturbations such as strain or applied magnetic fields ( $H$ ) [6,8], which is closely related to the origin of the colossal magnetoresistance effect of perovskite manganites [1,4]. Evidently, scientific understanding of the interrelationship between the nanoscale coexistence of competing phases and macroscopic physical properties is crucial for controlling the functionality of complex materials.

Multiferroics, where magnetism and ferroelectricity coexist in one material, have attracted great interest due to remarkable cross-coupling effects between seemingly distinct physical properties [9,10]. In a new class of multiferroics called magnetism-driven ferroelectrics, magnetic order without space-inversion symmetry breaks lattice space-inversion symmetry through exchange striction, inducing ferroelectricity [9,10]. Sufficient external  $H$  can change the spin configuration of magnetic order in magnetism-driven ferroelectrics and can result in drastic changes of ferroelectric (FE) and dielectric properties, i.e., large magnetoelectric (ME) effects [11–14]. Herein, we present a new way of achieving a colossal ME effect in a multiferroic by utilizing the high sensitivity of competing magnetic phases to external perturbations. We found that, in  $\text{Eu}_{0.75}\text{Y}_{0.25}\text{MnO}_3$ , a multiferroic (MF) phase with a cycloidal-spiral magnetic state can exist simultaneously

with a weak-ferromagnetic (WFM) phase in  $H$ . A glasslike ME state, called a ME glass, forms at low  $T$  by the kinetic arrest of the first-order spiral magnetic to WFM transition, resulting from the retarded growth of the low- $T$  WFM phase out of the supercooled high- $T$  MF phase upon cooling [5,6]. Upon heating, the ME glass becomes dearrested to the equilibrium WFM phase via thermal fluctuations above the freezing  $T$  [5,6]. Dynamically modulated two phases exhibit fascinating  $T$ -dependent magnetic and FE behaviors, and magnetization ( $M$ ) and polarization ( $P$ ) exhibit highly enhanced responses to electric fields ( $E$ ) or  $H$ .

$\text{Eu}_{1-x}\text{Y}_x\text{MnO}_3$  ( $x \leq 0.45$ ) crystallizes in an orthorhombically distorted perovskite structure (space group  $Pbnm$ ) [15–18]. It is reported that continuous increase of orthorhombic distortion by replacing  $\text{Eu}^{3+}$  ions by smaller  $\text{Y}^{3+}$  ions leads to an evolution of low- $T$  ground state from the WFM to the MF phase with a spiral magnetic order [16–18]. For  $x$  equal to or near zero, the low- $T$  magnetic state in zero  $H$  is a canted A-type AFM phase, i.e., a WFM phase, where Mn spins are aligned ferromagnetically in the  $ab$  plane and antiferromagnetically with a slight canting along the  $c$  axis [Fig. 1(a)]. Significant structural distortions for large  $x$  values result in a spiral spin state within the  $ab$  plane, which gives rise to a bulk FE polarization along the  $a$  axis,  $P_a$  [Fig. 1(b)] [19–21]. A single crystal of  $\text{Eu}_{0.75}\text{Y}_{0.25}\text{MnO}_3$  was grown by a floating zone method in argon gas flow. Three types of magnetic and electric measurements were performed: warming measurements after zero  $H$  cooling (ZFC-W), cooling measurements in  $H$  (FC-C), and warming measurements after cooling in  $H$  (FC-W).  $M$  was measured with a SQUID magnetometer (Quantum Design MPMS).  $P$  and the dielectric constant ( $\epsilon$ ) were obtained by integrating pyroelectric current measured with an electrometer and using an  $LCR$  meter at  $f = 44$  kHz, respectively [22].

Our single-crystalline  $\text{Eu}_{0.75}\text{Y}_{0.25}\text{MnO}_3$  in  $H$  exhibits an intricate balance between MF and WFM phases.  $T$ -dependent  $M_c$  and  $P_a$  ( $T_{FE} \approx 30$  K) of  $\text{Eu}_{0.75}\text{Y}_{0.25}\text{MnO}_3$

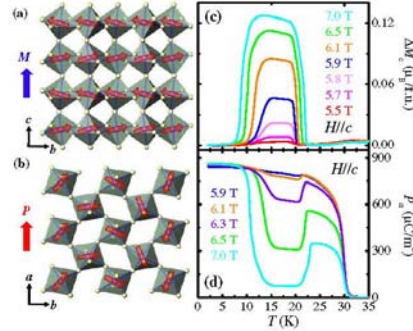


FIG. 1 (color online). (a),(b) Crystallographic and low- $T$  Mn-spin structures of orthorhombic perovskite  $\text{Eu}_{1-x}\text{Y}_x\text{MnO}_3$ . Magnetic  $\text{Mn}^{3+}$  ions locate at the center of octahedral  $\text{O}_2$  cages. Also shown are the directions of  $M$  and  $P$  of canted A-type AFM (WFM) and cycloidal-spiral magnetic phases, respectively. (c)  $T$  dependence of the  $H_c$ -induced WFM moment along the  $c$  axis,  $\Delta M_c$ , in  $H_c = 5.5\text{--}7.0$  T applied after zero-field cooling. (d)  $T$  dependence of  $P$  along the  $a$  axis,  $P_a$ , in  $H_c = 5.9\text{--}7.0$  T. Reduction of  $P_a$  in intermediate  $T$  ranges correlates with the emergence of WFM moment in (c).

[Figs. 1(c) and 1(d)], obtained in ZFC-W in  $H_c = 5.5\text{--}7.0$  T, reveal that a WFM moment develops in an intermediate  $T$  window in large  $H_c$ , and  $P_a$  is suppressed when the WFM moment appears. Figure 1(c) shows the  $T$  dependence of  $\Delta M_c = M_c - \chi_0 H_c$ , where linear susceptibility  $\chi_0$  is  $\sim 0.057 \mu_B/\text{f.u.}$  (f.u. denotes formula unit) and  $\Delta M_c$  corresponds to the  $H_c$ -induced WFM moment. Note that the maximum WFM moment ( $\sim 0.13 \mu_B/\text{f.u.}$ ) in 7.0 T is comparable with the WFM moment of the canted A-type AFM (or WFM) phase [Fig. 1(a)] in  $\text{Eu}_{1-x}\text{Y}_x\text{MnO}_3$  with zero or small  $x$  [17,18]. This suggests strongly that in  $\text{Eu}_{0.75}\text{Y}_{0.25}\text{MnO}_3$ , a WFM phase can appear in large  $H_c$  and is energetically nearly degenerate with the persisting MF phase [23]. The intermediate values of  $\Delta M_c$  and  $P_a$  in the  $T$  window of  $\sim 10\text{--}23$  K in  $H_c$  of  $\sim 5.5\text{--}7.0$  T suggest the coexistence of MF and WFM phases in a broad phase space region. With increasing  $H_c$ ,  $\Delta M_c$  increases,  $P_a$  decreases, and the coexisting  $T$  region of WFM and MF phases widens.

Detailed magnetic and FE behaviors through different  $T$ - $H$  procedures turn out to be consistent with the kinetic arrest and dearrest processes of the first-order MF to WFM transition. These behaviors are closely analogous with the magnetic and transport behaviors of colossal magnetoresistance manganites [6,7,24,25]. Figure 2(a) displays  $T$ -dependent  $\Delta M_c$  obtained through three different  $T$ - $H$  procedures in  $H_c = 5.9$  T: ZFC-W (open circles), FC-C (open squares), and FC-W (open triangles). The freezing  $T_f$ , below which kinetics of the first-order MF to WFM transition is arrested probably due to a significant frozen

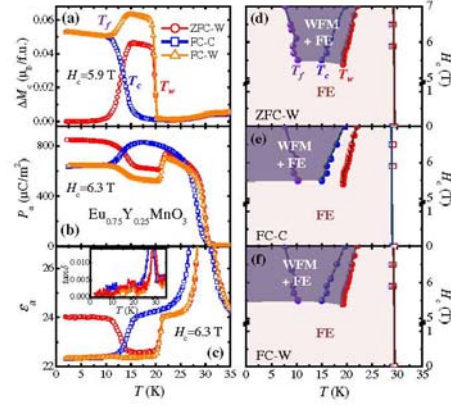


FIG. 2 (color online). (a)–(c)  $T$  dependence of  $\Delta M_c$  in  $H_c = 5.9$  T,  $P_a$  in  $H_c = 6.3$  T, and  $\epsilon_a$  [tan $\delta$  in the inset in (c)] in  $H_c = 6.3$  T, respectively. For the data in each figure, three different measurements were performed: upon warming after cooling in  $H_c = 0$  T (ZFC-W, open circles), upon cooling in  $H_c$  (FC-C, open squares), and upon warming after cooling in  $H_c$  (FC-W, open triangles).  $T_f$  denotes a freezing  $T$ .  $T_c$  and  $T_w$  correspond to the first-order transition  $T$  between the MF and WFM phases for cooling and warming, respectively. (d)–(f)  $H$ - $T$  phase diagrams for three different procedures (ZFC-W, FC-C, and FC-W), obtained from  $T$ -dependent  $\Delta M_c$  data. Dark areas represent the coexistence regions of FE and WFM phases, depending on the  $T$ - $H$  history.

disorder and thus a ME glass forms, is determined by  $T$  at which the FC-C and FC-W  $\Delta M_c$  curves start to deviate from each other at low  $T$ . The first-order nature of the MF to WFM transition is well reflected in the large thermal hysteresis.  $T_c$  and  $T_w$  denote the transition  $T$  upon cooling and warming, respectively.  $\Delta M_c$  for ZFC-W in  $H_c = 5.9$  T is close to zero at low  $T$ , indicating that the low- $T$  state after ZFC is purely MF. Upon warming above  $T_f$ , the kinetically arrested MF phase starts to get dearrested to the equilibrium state with the coexisting MF and WFM phases. This thermally assisted dearresting process gives rise to a WFM moment upon warming above  $\sim 10$  K [6]. This WFM moment disappears above  $T_w$ . For FC-C, a WFM phase develops below  $T_c$  and shows an almost plateaulike  $\Delta M_c$  feature at low  $T$ , possibly due to a significantly retarded relaxation below  $T_f$ . Upon warming during FC-W above  $T_f$ , the frozen ME glass melts, and this melting generates an additional WFM moment upon warming above  $T_f$  [24,25].

$P_a$  and  $\epsilon_a$  behaviors through different  $T$ - $H$  histories are highly consistent with the  $\Delta M_c$  behavior. For example,  $P_a$  in 6.3 T basically behaves in an opposite manner to the variation of  $\Delta M_c$  [Fig. 2(b)]. Upon warming of ZFC-W,  $P_a$  of the MF phase after ZFC decreases in compensation of



the growth of the WFM moment above  $T_f$ . At  $T_w$ , the reduced  $P_a$  jumps to a larger value upon warming while the WFM moment vanishes.  $P_a$  for FC-C shows a decrease below  $T_c$  in parallel with the emergence of the WFM moment, and the reduced  $P_a$  remains intact below  $T_f$ . Upon warming of FC-W, the reduced  $P_a$  decreases further as an additional WFM moment appears and becomes sharply enhanced above  $T_w$  when the WFM phase disappears.  $e_a$ , obtained in 6.3 T [Fig. 2(c)], exhibits a peak at the onset  $T$  ( $\sim 30$  K) of  $P_a$ , similar with a typical behavior at an FE transition. Steplike features of  $e_a$  at  $T_c$  and  $T_w$  appear similar with those of  $P_a$ , and the negligible  $T$  dependence of  $e_a$  below  $T_f$  is consistent with the formation of a ME glass below  $T_f$  through kinetic arrest. The reasonably small magnitude of tangential loss  $\tan\delta$  in the inset in Fig. 2(c) indicates that the specimen is insulating enough to sustain the FE properties.

Figures 2(d)–2(f) display  $T$ - $H$  phase diagrams from our  $\Delta M_c$  data for three different procedures in  $H_c$ . The phase diagrams manifest coexisting regions of the MF and WFM phases. The MF phase persists below the FE transition  $T$ , but the WFM phase appears in different regions, depending on the  $T$ - $H$  history. Coexisting  $T$  ranges of MF and WFM phases can be summarized as  $T_f < T < T_w$  for ZFC-W,  $T < T_c$  for FC-C, and  $T < T_w$  for FC-W.

We found that magnetic and FE properties of  $\text{Eu}_{0.75}\text{Y}_{0.25}\text{MnO}_3$  are controllable by  $E$  and  $H$ , respectively, through changing the relative volume fraction of the MF and WFM phases. As shown in Figs. 1(c) and 1(d), increasing  $H_c$  enhances the WFM phase in the two-phase region while it demotes the MF phase.  $E_a$  also considerably influences both phases. In Fig. 3(a), the solid curves show the  $T$ -dependent  $\Delta M_c$  measured in  $H_c = 5.9$  T as well as  $E_a \approx 10$  kV/cm. It reveals that the WFM moment is remarkably reduced from the value obtained in zero  $E_a$ . In ZFC-W, the maximum WFM moment in zero  $E_a$  reaches  $0.046 \mu_B/\text{f.u.}$  at  $\sim 15$  K, whereas the WFM moment in  $E_a \approx 10$  kV/cm is reduced by  $\sim 50\%$ . For the  $E_a \approx 10$  kV/cm measurement,  $E_a$  was held during the entire process: The initial poling process in  $+E_a$  produces a single FE domain with  $+P_a$  [22], and warming of the  $+P_a$  state in  $+E_a$  restrains the development of the WFM moment. Note that, for FC-C and FC-W, the maximum WFM moment was found to decrease by  $\sim 30\%$  and  $20\%$ , respectively, in  $E_a \approx 10$  kV/cm. Note that the  $T$  ranges where the WFM moment is significantly influenced by applying  $E_a$  match well with the dark shaded regions in the  $H$ - $T$  phase diagrams in Figs. 2(d)–2(f), indicating the coexistence regions of the MF and WFM phases. As the WFM moment decreases with  $E_a$ ,  $P_a$  can be “promoted” by applying  $E_a$ . Figure 3(b) shows the  $T$ -dependent  $P_a$  for ZFC-W and FC-W in 6.3 T with and without  $E_a \approx 10$  kV/cm. Because of the poling procedure required for the pyroelectric current measurements on  $\text{Eu}_{0.75}\text{Y}_{0.25}\text{MnO}_3$ ,  $P_a$ ’s with and without  $E_a$  begin with the same value at 2 K.  $P_a$  curves with and without  $E_a$  start

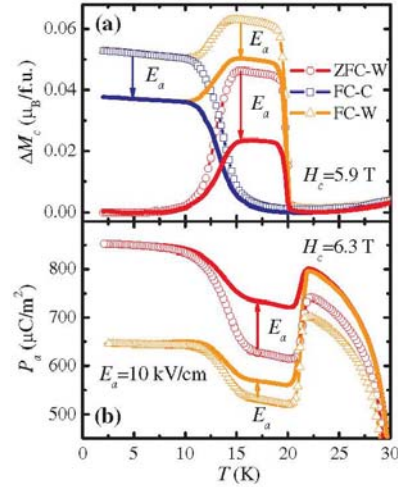


FIG. 3 (color online). (a) Comparison of  $T$ -dependent  $\Delta M_c$  in  $H_c = 5.9$  T measured in  $E_a = 0$  [the same with the data in Fig. 2(a)] and  $E_a \approx +10$  kV/cm (solid curves) for ZFC-W, FC-C, and FC-W.  $\Delta M_c$  is significantly reduced by the application of  $E_a$  in the two-phase coexisting regions. (b) Comparison of  $T$ -dependent  $P_a$  in  $H_c = 6.3$  T in  $E_a = 0$  [the same with data in Fig. 2(b)] and  $E_a \approx +10$  kV/cm (solid curves) for ZFC-W and FC-W.  $P_a$  becomes enhanced with applied  $E_a$  in the intermediate  $T$  range, where  $\Delta M_c$  is suppressed with  $E_a$ .

to deviate to each other above  $T_f$ , and the maximum differences for ZFC-W and FC-W are  $\sim 17\%$  and  $8\%$ , respectively. The relatively small differences of  $P_a$  produced by applying  $E_a$ , compared to the  $\Delta M_c$  differences in Fig. 3(a), may stem from the same poling process used for the  $P_a$  measurements with and without  $E_a$ . Note that a data set of FC-C is not present in Fig. 3(b) because  $P_a$  for FC-C in Fig. 2(b) is obtained always in the presence of poling  $E_a$ .

Repeated variation of  $\Delta M_c$  is achieved by changing  $E_a$  linearly between  $+10$  and  $-10$  kV/cm as shown in Figs. 4(a) and 4(b). Time-dependent  $\delta M_c$  (the variation of  $\Delta M_c$ ) was measured at 15 K in  $E_a = 0$  and  $H_c = 5.5$  T, after cooling the specimen in  $E_a \approx +10$  kV/cm and  $H_c = 0$  down to 2 K and then warming to 15 K in  $E_a = 0$  and  $H_c = 5.5$  T. Initial poling in  $+E_a$  produces a single FE domain with  $+P_a$  [22], and warming to 15 K in  $H_c = 5.5$  T creates a small WFM moment associated with a small volume fraction of the WFM phase at 15 K. Because of kinetic dearrest at 15 K,  $\Delta M_c$  relaxes significantly with time as shown in the inset in Fig. 4(a). On top of the relaxation tendency,  $\Delta M_c$  oscillates in a manner opposite to the variation of  $E_a$ . Repeated variation of  $\Delta M_c$  in Fig. 4(a) is obtained after subtracting the increasing part of  $\Delta M_c$  as a relaxation background. Initial increase

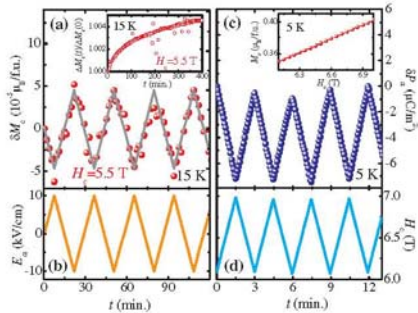


FIG. 4 (color online). (a),(b) Repeated variation of  $\Delta M_c$  ( $\delta M_c$ ) at 15 K in  $H_c = 5.5$  T by applying  $E_a$ , varied linearly with time between +10 and -10 kV/cm. The inset in (a) shows time-dependent  $\Delta M_c$  in  $H_c = 5.5$  T at 15 K without  $E_a$ .  $\delta M_c$  was obtained after subtracting the relaxation part shown in the inset in (a).  $\delta M_c$  follows a linear fit well (solid line) and varies in a manner opposite to the  $E_a$  variation, shown in (b). (c), (d) Linearly modulated  $P_a$  ( $\delta P_a$ ) with time at 5 K with a linear variation of  $H_c$  between 6.1 and 7.0 T. The inset in (c) displays  $H_c$ -dependent  $M_c$  at 5 K for  $6.1 \text{ T} < H_c < 7.0 \text{ T}$  after cooling in 6.1 T.

of positive  $E_a$  leads to a linear decrease in  $\Delta M_c$ , probably due to strengthening of the MF phase with  $+P_a$ . When  $E_a$  is reduced from +10 and -10 kV/cm,  $\Delta M_c$  increases linearly. This tendency repeats with oscillating variation of  $E_a$ . As a counterpart, modulation of  $P_a$  ( $\delta P_a$ ) with  $H_c$  is obtained at 5 K as shown in Fig. 4(c). Note that, above  $T_f$ , the relaxation of  $P_a$  (i.e., the continuous decrease of  $P_a$  with time) was large, so we were not able to measure the modulation of  $P_a$  with  $H_c$ . Instead, the specimen was prepared by cooling to 5 K, below  $T_f$ , in  $E_a \approx +10$  kV/cm and  $H_c = 6.1$  T, and then removing  $E_a$ . We found that, despite the kinetic arrest below  $T_f$ , repeated variation of  $H_c$  between 6.1 and 7.0 T [Fig. 4(d)] gives rise to a linear modulation of  $P_a$  on the order of 1%, in a manner opposite to the change of  $M_c$  [inset in Fig. 4(c)].

In summary, in  $\text{Eu}_{0.75}\text{Y}_{0.25}\text{MnO}_3$  with the presence of  $H_c$ , a MF phase with cycloidal-spiral magnetism intricately balances with an emergent WFM phase. Coexistence of competing MF and WFM phases in a broad range of  $T$ - $H$  phase space results from kinetic arrest-dearest processes of the first-order MF to WFM phase transition, strongly depending on the  $T$ - $H$  history. Coexistence of the competing phases can be significantly influenced by external perturbations such as  $E$  and  $H$ , which leads to a remarkable control of  $M$  and  $P$  with  $E$  and  $H$ . We emphasize that most of the large ME coupling effects in multiferroics are associated with the control of  $P$  with  $H$ . However, the control

of FM-type  $M$  by applying  $E$  is most relevant to technological applications, but scarcely observed [26,27]. Our results are clearly distinct from the recent work on  $\text{GdFeO}_3$ , where a control of  $M$  by  $E$  is achieved by manipulating partially clamped FE and FM domains [27], and provide a new revenue to achieve a true cross-control of  $M$  and  $P$  with  $E$  and  $H$ .

We acknowledge D. Kwok for improving the presentation of the manuscript. This work was supported by NSF Grant No. DMR-080410.

\*Present address: Department of Physics, University of Tennessee, Knoxville, TN 37996, USA.

- [1] See, for example, E. Dagotto, *Nanoscale Phase Separation and Colossal Magnetoresistance* (Springer-Verlag, New York, 2003).
- [2] See, for example, *Proceedings of the Workshop on Phase Separation in Cuprate Superconductors*, Erice, Italy, 1992 (World Scientific, New York, 2003).
- [3] R.J. Zeches *et al.*, *Science* **326**, 977 (2009).
- [4] M. Uehara *et al.*, *Nature (London)* **399**, 560 (1999).
- [5] M.K. Chattopadhyay *et al.*, *Phys. Rev. B* **72**, 180401(R) (2005).
- [6] K. Kumar *et al.*, *Phys. Rev. B* **73**, 184435 (2006).
- [7] P. Chaddah *et al.*, *Phys. Rev. B* **77**, 100402(R) (2008).
- [8] K.H. Ahn *et al.*, *Nature (London)* **428**, 401 (2004).
- [9] S.W. Cheong and M. Mostovoy, *Nature Mater.* **6**, 13 (2007).
- [10] D.I. Khomskii, *Physics* **2**, 20 (2009).
- [11] N. Hur *et al.*, *Nature (London)* **429**, 392 (2004); *Phys. Rev. Lett.* **93**, 107207 (2004).
- [12] T. Kimura *et al.*, *Nature (London)* **426**, 55 (2003); *Phys. Rev. Lett.* **94**, 137201 (2005); *Phys. Rev. B* **73**, 220401(R) (2006).
- [13] G. Lawes *et al.*, *Phys. Rev. Lett.* **95**, 087205 (2005); *Phys. Rev. B* **74**, 024413 (2006).
- [14] K. Taniguchi *et al.*, *Phys. Rev. Lett.* **97**, 097203 (2006).
- [15] Y. Noda *et al.*, *J. Appl. Phys.* **99**, 08S905 (2006).
- [16] V. Yu. Ivanov *et al.*, *Phys. Status Solidi B* **243**, 107 (2006).
- [17] J. Hemberger *et al.*, *Phys. Rev. B* **75**, 035118 (2007).
- [18] Y. Yamasaki *et al.*, *Phys. Rev. B* **76**, 184418 (2007).
- [19] T. Kimura *et al.*, *Phys. Rev. B* **68**, 060403(R) (2003).
- [20] H. Katsura *et al.*, *Phys. Rev. Lett.* **95**, 057205 (2005); C. Jia *et al.*, *Phys. Rev. B* **76**, 144424 (2007).
- [21] M. Mostovoy, *Phys. Rev. Lett.* **96**, 067601 (2006).
- [22] See supplementary material at <http://link.aps.org/supplemental/10.1103/PhysRevLett.105.097201> for sample preparation, measurement details, and ferroelectric characterization of  $\text{Eu}_{0.75}\text{Y}_{0.25}\text{MnO}_3$  crystal.
- [23] S. Danjoh *et al.*, *Phys. Rev. B* **80**, 180408(R) (2009).
- [24] L. Ghivelder and F. Parisi, *Phys. Rev. B* **71**, 184425 (2005).
- [25] P.A. Sharma *et al.*, *Phys. Rev. B* **71**, 224416 (2005).
- [26] E. Ascher *et al.*, *J. Appl. Phys.* **37**, 1404 (1966).
- [27] Y. Tokunaga *et al.*, *Nature Mater.* **8**, 558 (2009).



## Appendix II.

RAPID COMMUNICATIONS

PHYSICAL REVIEW B 84, 020101(R) (2011)



# Mechanism of exchange striction of ferroelectricity in multiferroic orthorhombic $\text{HoMnO}_3$ single crystals

N. Lee,<sup>1</sup> Y. J. Choi,<sup>1</sup> M. Ramazanoglu,<sup>1</sup> W. Ratcliff II,<sup>2</sup> V. Kiryukhin,<sup>1</sup> and S.-W. Cheong<sup>1</sup><sup>1</sup>Rutgers Center for Emergent Materials and Department of Physics & Astronomy, Rutgers University, Piscataway, New Jersey 08854, USA<sup>2</sup>NIST Center for Neutron Research, NIST, Gaithersburg, Maryland 20899, USA

(Received 21 April 2011; published 1 July 2011)

*E*-type perovskite magnet  $\text{HoMnO}_3$  is considered to be a prototype Mn-Mn exchange-striction driven multiferroic. We have grown orthorhombic  $\text{HoMnO}_3$  single crystals and studied the directional dependence of their electric polarization  $P$ . The direction of  $P$  is not along the crystallographic  $a$  axis, as predicted, but along the  $c$  axis. The magnetic state is incommensurate. The direction  $P$  along the  $c$  axis is primarily induced by Ho-Mn exchange striction, and Mn-Mn striction in the incommensurate spin state leads to an antiferroelectric order along the  $a$  axis. We predict the rotation of  $P$  with temperature in commensurate *E*-type  $\text{RMnO}_3$  ( $R$  denotes magnetic rare earth).

DOI: 10.1103/PhysRevB.84.020101

PACS number(s): 77.80.-e, 75.30.Et, 75.80.+q

Multiferroics attract a significant amount of attention because of the cross coupling between magnetism and ferroelectricity (FE) and the related possibility of controlling magnetism with an electric field (and vice versa).<sup>1,2</sup> FE induced by magnetic order is especially interesting because of the strong effect of a magnetic field ( $H$ ) on the ferroelectric order. Exchange striction is a major mechanism producing FE in magnetically ordered systems.<sup>2</sup> Both symmetric and antisymmetric parts of the exchange coupling can drive FE. The latter case is known to occur in spiral magnets, such as  $\text{TbMnO}_3$ .<sup>2</sup> These systems exhibit small electric polarizations ( $P$ ) of the order of  $10^{-1} \mu\text{C}/\text{cm}^2$  three orders of magnitude smaller than in proper ferroelectrics. Symmetric exchange is expected to produce much larger  $P$ . However, the corresponding materials identified so far show similarly small values of  $P$ .<sup>3,4</sup> Theoretical predictions<sup>5,6</sup> of a 100-times-larger  $P$  in the magnetic *E* phase of orthorhombic perovskite manganites  $\text{o-RMnO}_3$  ( $R = \text{Ho-Lu}$  and  $\text{Y}$ ) induced by Mn-Mn exchange striction has, therefore, attracted a lot of interest.<sup>7-10</sup> Unfortunately, these compounds exhibit<sup>9,10</sup> maximum  $P$  values of only  $\sim 10^{-1} \mu\text{C}/\text{cm}^2$ . In many cases (e.g., for  $R = \text{Ho}$ ), any significant  $P$  is achieved only below the rare-earth magnetic ordering temperature ( $T$ ).<sup>9</sup> This indicates an essential role of the rare-earth magnetism, which is unaccounted for in the extant models. Importantly, all the *E*-type manganites studied so far have been synthesized only in the polycrystalline form, preventing characterization of many of their intrinsic properties.

In this paper, we report the studies on single crystals of orthorhombic  $\text{HoMnO}_3$  ( $\text{o-HoMnO}_3$ ). Unexpectedly, we find that  $P$  is pointing along the crystallographic  $c$  axis, contrary to the theoretical prediction<sup>5,6</sup> of  $P \parallel a$ . We argue that Ho-Mn exchange striction plays a key role in this system, and we discuss possible outcomes of the Mn-Mn interaction in the orthorhombic manganites. Our model predicts that in magnetic rare-earth manganites, coexisting Mn-Mn and *R*-Mn interactions can give rise to a distinctive phenomenon—a temperature-dependent direction of  $P$ .

$\text{o-HoMnO}_3$  crystallizes in a distorted perovskite structure (space group  $Pbnm$ ), shown in Fig. 1(a). We have synthesized rodlike large single crystals with dimensions up to

$2 \times 2 \times 7 \text{ mm}^3$  [see Fig. 1(b)] utilizing the conventional  $\text{Bi}_2\text{O}_3$  flux method. Previously, polycrystalline  $\text{o-HoMnO}_3$  was obtained using high-pressure synthesis. We find that flux growth with  $\text{Bi}_2\text{O}_3$ ,  $\text{Ho}_2\text{O}_3$ , and  $\text{MnO}_2$  can stabilize both hexagonal and orthorhombic crystals at ambient pressure. A mixture of  $\text{Bi}_2\text{O}_3\text{:Ho}_2\text{O}_3\text{:MnO}_2$  in a 6:0.5:1 ratio produces the hexagonal phase, whereas a 12:0.5:1 ratio leads to orthorhombic single crystals. The crystals exhibit an orthorhombic perovskite structure with  $a = 5.2689(2)$ ,  $b = 5.8450(2)$ , and  $c = 7.3698(2) \text{ \AA}$  at room temperature, and no twinning, as confirmed by refinement of single-crystal x-ray-diffraction data. This is consistent with the previously published structure of polycrystalline samples.<sup>11,12</sup> The absence of twinning was further confirmed by neutron-diffraction experiments, in which a careful search revealed no diffraction peaks due to possible twin domains. Magnetization ( $M$ ) was measured with a SQUID magnetometer.  $P$  and the dielectric constant ( $\epsilon$ ) were obtained by integrating pyroelectric current measured with an electrometer and using an LCR meter at  $f = 44 \text{ kHz}$ , respectively. Neutron-diffraction data were collected on a BT9 triple-axis spectrometer at the NIST Center for Neutron Research. In all figures, error bars (one standard deviation) are smaller than the symbol size.

Mn spins in  $\text{o-HoMnO}_3$  order at  $T_N \approx 40 \text{ K}$ , exhibiting  $(0, A_y, 0)$ -type incommensurate structure with wave vector  $Q = (h, k, l) = (0, \sim 0.4, 0)$  and spins parallel to the  $b$  axis.<sup>11</sup> At a lower  $T$ , some polycrystalline samples<sup>12</sup> become commensurate with  $k = 0.5$ , exhibiting the *E*-type order discussed theoretically in Ref. 5 and shown in Fig. 1(a). For  $T < 15 \text{ K}$ , Ho spins order in the  $(a_x, f_y, 0)$  pattern and the same  $Q$  as Mn.<sup>11</sup> Our data are consistent with these results. Magnetic-field ( $H$ ) and  $T$  dependences of  $M$  are shown in Figs. 1(c) and 1(d). The anomalies corresponding to  $T_N = 42 \text{ K}$  and  $T_{\text{Ho}} = 15 \text{ K}$  are clearly observed in the  $T$  derivative of  $M_c$  shown in the inset in Fig. 1(d), as well as in the  $M_a$  and  $M_b$  derivatives (not shown). At low  $T$ , a substantial magnitude of  $M_b$  develops, possibly due to Ho contribution. Figure 2 shows the  $T$  dependence of various physical properties under zero  $H$ . The onset of tiny ferroelectric polarization along the  $c$  axis ( $P_c$ ) occurs at  $T = 30 \text{ K}$  [Fig. 2(a)], and  $P_c$  exhibits an abrupt increase at  $T_{\text{Ho}} = 15 \text{ K}$ , reaching  $1500 \mu\text{C}/\text{m}^2$  at  $2 \text{ K}$ . The magnitudes of  $P_a$  and

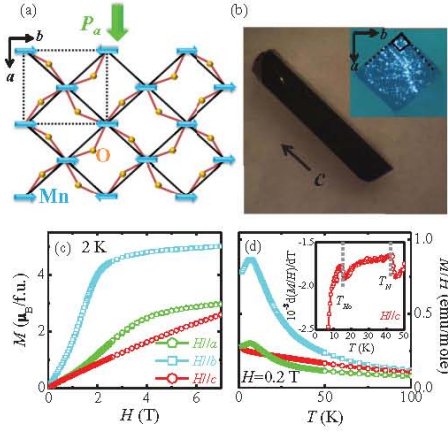


FIG. 1. (Color online) (a) Lattice and magnetic structure ( $k = 0.5$ ) of  $E$ -type orthorhombic  $RMnO_3$ .  $R$  atoms are not shown. Oxygen displacements reflect the effect of Mn-Mn exchange striction. Dashed line shows structural unit cell. The magnetic unit cell is twice as large in the  $y$  direction. (b) Single crystal of  $o$ -HoMnO<sub>3</sub>. (c) Magnetization vs magnetic field for  $T = 2$  K. (d) Magnetic susceptibility vs temperature ( $1 \text{ emu} = 4\pi \times 10^{-6} \text{ m}^3$ ). The inset shows the temperature derivative of the susceptibility.

$P_b$  are negligible at any  $T$ . The dielectric constant along the  $c$  axis ( $\epsilon_c$ ) displays a pronounced peak at  $T_{Ho}$ , in accordance with the appearance of FE, whereas  $\epsilon_a$  increases broadly below  $T_N$ ; see Fig. 2(b). The specific heat, shown in Fig. 2(d), exhibits

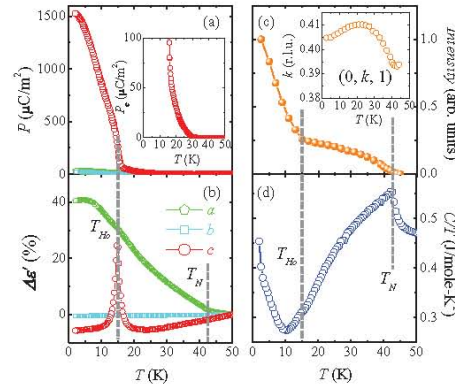


FIG. 2. (Color online) Temperature dependences of the electric polarization (a) and dielectric susceptibility (b) along the three crystallographic axes. (c) Integrated intensity of the  $(0, k, 1)$  magnetic peak vs temperature. The  $k$  component of the peak position is shown in the inset. (d) Temperature dependence of the specific heat.

a sharp peak at  $T_N$ , and a small (but discernable) anomaly at  $T_{Ho}$  is also visible.

Neutron-diffraction data show that our samples are incommensurate at all temperatures. Figure 2(c) shows the  $T$  dependence of the integrated intensity of the  $(0, k, 1)$  magnetic peak,  $k \approx 0.4$ . The magnetic order appears at  $T_N = 42$  K, and the peak intensity increases significantly for  $T < T_{Ho}$ , simultaneously with a large increase of  $P_c$ . The inset in Fig. 2(c) shows the  $T$ -dependent position  $k$  of the magnetic peak obtained from Gaussian fits. With decreasing  $T$ ,  $k$  exhibits a slight variation but always stays close to  $k = 0.4$ . There appear to be changes in the slope of this dependence in the vicinity of the FE anomalies at  $\sim 30$  K and at 15 K, reflecting the magnetoelectric coupling in this system.

The FE in the  $E$ -type manganites is currently believed<sup>5,6</sup> to be induced by Mn-Mn symmetric exchange striction, i.e., repulsion of coaligned Mn spins. This repulsion, together with the associated motion of the oxygen ions, leads to the appearance of  $P_a$ , as illustrated in Fig. 1(a) for the  $k = 0.5$  commensurate state. The Mn spin is given by  $S_y(y) = S \cos(ky - \varphi_i)$ , where  $\varphi_0$  and  $\varphi_{1/2}$  are the phases for the two spin chains along the  $b$  axis in the unit cell, one at  $x = 0$  and the other at  $x = 0.5$  ( $x, y$  are in lattice units); see Fig. 3(a). In the  $E$ -type commensurate state,  $k = 0.5$ ,  $\Delta\varphi \equiv \varphi_{1/2} - \varphi_0 = \pi/2$ , and the magnetic structure lacks the inversion symmetry, i.e., it is acentric. It is consistent with nonzero  $P_a$  when superimposed on the lattice structure. In the  $k \neq 0.5$  state, the spin magnitude

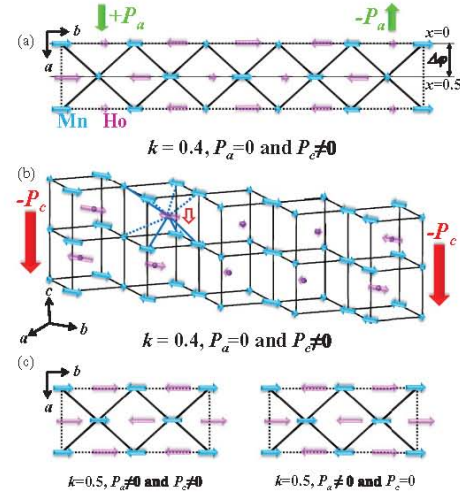


FIG. 3. (Color online) (a), (b) The magnetic order leading to  $P_a = 0$  and  $P_c < 0$  in the  $k = 0.4$  state. Dashed line in (a) outlines the magnetic unit cell. In (b), thick solid and dashed lines designate attractive and repulsive Ho-Mn interactions, respectively. (c) Spin structures with zero and nonzero  $c$ -axis polarization in the  $k = 0.5$   $E$ -type state. In all figures, the  $a$ -axis components of the Ho spins are not shown.



is not constant, and other phase differences  $\Delta\varphi$  are allowed, leading to both polar acentric (e.g.,  $\Delta\varphi = \pi/2$ ) and centric ( $\Delta\varphi = 0$  and  $\pi$ ) spin-density waves (SDW's).<sup>13</sup> In the latter case,  $P_a = 0$  if the inversion centers of the SDW and the atomic structure coincide. In our samples, measured  $P_a$  is zero, and therefore the centric incommensurate SDW must be realized. One of the two possible Mn magnetic structures for the centric incommensurate SDW, corresponding to  $\Delta\varphi = 0$ , is shown in Fig. 3(a); the other with  $\Delta\varphi = \pi$  simply has the opposite spin direction for  $x = 0.5$ . (For simplicity, the  $k = 0.4$  state with a period of exactly five unit cells is shown.) These structures are antiferroelectric, with one-half of the unit cell having the opposite  $P_a$  to the other. The large increase of  $\epsilon_a$  below  $T_N$  (Fig. 2) without the presence of  $P_a$  strongly supports this conclusion.

The primary result of our work is the unexpected direction of  $P$ . Because of the clear association of FE with the Ho order, the natural candidate mechanism of multiferroicity is Ho-Mn interaction. In fact, rare-earth-3d element interaction was reported to be essential in multiferroic orthoferrites,<sup>14,15</sup> as well as to play a role in some spiral manganites.<sup>16,17</sup> We find that Ho-Mn exchange striction indeed provides a simple explanation for the observed phenomena. Disregarding the  $x$  component of the Ho spins, which does not contribute to the striction, the Ho SDW order essentially follows that of Mn, but with an experimentally undetermined phase shift between the two.<sup>11</sup> To maximize the energy gain from the Ho-Mn striction producing the  $c$ -axis displacement, the phase shift should be zero or  $\pi$  because it pairs large Ho and Mn spins adjacent in the  $x$  direction (the Mn spins adjacent in the  $y$  direction are antiparallel to each other for the same  $z$ , partially canceling the effect of the striction). As shown in Fig. 3(b) for one of these phase shifts, the Ho spin is then anti-aligned with the three Mn spins below, and aligned with the three Mn spins above, and moves down due to exchange striction. One can readily check that in this case, Mn-Ho exchange striction moves all the Ho spins of one chain (e.g., for  $x = 0$ ) in the same direction along the  $c$  axis. The energy gain is the same for aligning with the Mn spins above or below the Ho atom, and therefore the  $x = 0$  and  $0.5$  Ho chains in the magnetic unit cell can either have the same or the opposite directions of  $P_c$ . Experimentally,  $P_c \neq 0$ , and therefore the Ho order shown in Figs. 3(a) and 3(b), which produces the same  $P_c$  in every Ho chain, should be realized. Clearly, experimental confirmation of this phase relationship between the Ho and Mn SDW's, and whether it is affected by the poling used for  $P_c$  measurements, would be of significant interest. Finally, we note that the onset of the weak  $P_c$  at  $T \approx 30$  K could be produced via the same mechanism due to the weak Ho moment induced by the Mn order, which was previously observed in polycrystalline samples.<sup>12</sup>

*o*-HoMnO<sub>3</sub> exhibits a strong magnetoelectric effect. Figure 4(a) shows the full suppression of  $P_c$  at  $H = 2$  and 4 T for  $H \parallel b$  and  $H \parallel a$ , respectively. For  $H \parallel c$ , only a small decrease of  $P_c$  is found. The suppression of  $P_c$  coincides with a drop in  $\epsilon_c$  [Fig. 4(b)] and with an anomaly in  $dM/dH$  [inset in Fig. 4(a)]. The vanishing polarization is probably associated with field-induced reorientation of the Ho spins and the corresponding changes in the effects of Ho-Mn exchange striction. Our data show that the reorientation is easier to achieve in the  $ab$  plane, consistent with the magnetic anisotropy that tends to confine

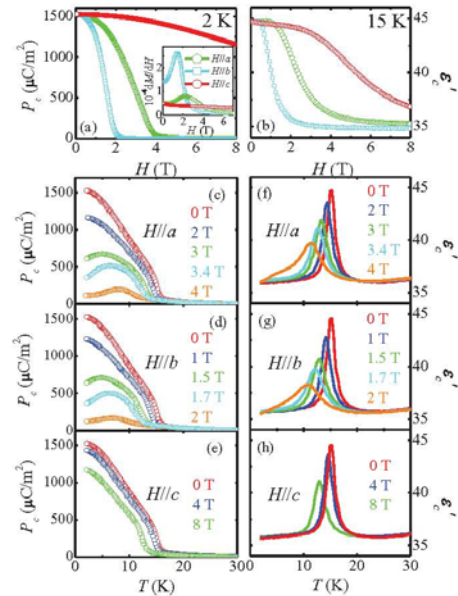


FIG. 4. (Color online) Magnetic-field dependences of the electric polarization  $P_c$  (a) and dielectric susceptibility  $\epsilon_c$  (b) for different directions of  $H$ . Temperature dependences of the electric polarization (c)–(e) and the dielectric susceptibility (f)–(h) in various applied magnetic fields.

the Ho spins there.<sup>11,12</sup> Figures 4(c)–4(e) show  $T$  dependences of  $P_c$  and  $\epsilon_c$  in various applied fields. Consistent with the data of Figs. 4(a) and 4(b), the magnetic field suppresses the ferroelectric state and decreases the ferroelectric transition temperature.

The presence of two coexisting exchange-striction mechanisms of multiferroicity in the  $E$ -type orthorhombic manganites is the key result of this work. Depending on the phase relationships within and between the Mn and Ho SDW's, both Mn-Mn and Ho-Mn interactions can produce zero or nonzero electric polarization along the  $a$  and  $c$  axis, respectively. The  $k = 0.5$  state appears to be an exception for which the  $P_a = 0$  state is absent, because centric SDW would imply zero Mn spin for half of the Mn ions. However, even for  $k = 0.5$ , states with both zero and nonzero  $P_c$  are possible, as illustrated in Fig. 3(c). The presence of two coexisting mechanisms producing different directions of  $P$  may open possibilities for distinctive magnetoelectric control, and should lead to previously unobserved phenomena. In our samples, only one mechanism (Ho-Mn) leads to FE. However, some of the previously studied polycrystalline *o*-HoMnO<sub>3</sub> samples<sup>12</sup> enter the  $k = 0.5$  state at  $T = T_L$ , which is larger than  $T_{Ho}$ , and significant  $P$  is observed for  $T_{Ho} < T < T_L$ . A large increase of  $P$  at  $T_{Ho}$  is also present in these samples. For these samples, our model predicts that the polarization is initially



along the  $a$  axis, and that a large  $c$ -axis component develops in addition with decreasing  $T$ . Thus, we expect that the *direction* of  $P$  changes with  $T$  in the  $k = 0.5$  crystals. The reason for the variation of the exact magnitude and  $T$  dependence of  $P$  and (in)commensurability among published results in polycrystalline specimens<sup>11,12</sup> and our crystal data is currently unclear, but the presence of defects or residual strains may play an important role. To verify the intriguing possibility of temperature-induced rotation of the  $P$ , preparation of such  $k = 0.5$  crystals is certainly desirable.

In summary, we report studies of single-crystalline  $\alpha$ -HoMnO<sub>3</sub>, which is currently considered to be a prototype  $E$ -type multiferroic with a symmetric exchange-striction mechanism. Contrary to the current belief, the ferroelectric polarization in our crystals is along the  $c$  axis. We argue that Mn-Mn and Ho-Mn exchange striction mechanisms coexist in

this system. These mechanisms can lead to both ferroelectric and antiferroelectric orders along the  $a$  axis (Mn-Mn) and the  $c$  axis (Ho-Mn). In our samples, the Ho-Mn interaction produces the  $c$ -axis polarization, while the Mn-Mn exchange striction induces the  $a$ -axis antiferroelectric order. We also propose that under certain conditions, these coexisting mechanisms should lead to temperature-induced rotation of FE polarization in the  $E$ -type manganites.

We are grateful to T. Emge for experimental assistance. This work was supported by the NSF under Grants No. DMR-1004568 and No. DMR-0804109. Y.J.C. was supported partially by a subgrant with Seoul National University under Prime Agreement Award No. KRF-2008-220-C00012 from the Global Research Network Program of the National Research Foundation.

- <sup>1</sup>W. Eerenstein, N. D. Mathur, and J. F. Scott, *Nature (London)* **442**, 759 (2006).
- <sup>2</sup>S.-W. Cheong and M. Mostovoy, *Nat. Mater.* **6**, 13 (2007).
- <sup>3</sup>N. Hur, S. Park, P. A. Sharma, J. S. Ahn, S. Guha, and S.-W. Cheong, *Nature (London)* **429**, 392 (2004).
- <sup>4</sup>Y. J. Choi, H. T. Yi, S. Lee, Q. Huang, V. Kiryukhin, and S.-W. Cheong, *Phys. Rev. Lett.* **100**, 047601 (2008).
- <sup>5</sup>I. A. Sergienko, C. Sen, and E. Dagotto, *Phys. Rev. Lett.* **97**, 227204 (2006).
- <sup>6</sup>S. Picozzi, K. Yamauchi, I. A. Sergienko, C. Sen, B. Sanyal, and E. Dagotto, *J. Phys. Condens. Matter* **20**, 434208 (2008).
- <sup>7</sup>K. Yamauchi, F. Freimuth, S. Blugel, and S. Picozzi, *Phys. Rev. B* **78**, 014403 (2008).
- <sup>8</sup>S. Ishiwata, Y. Kaneko, Y. Tokunaga, Y. Taguchi, T. Arima, and Y. Tokura, *Phys. Rev. B* **81**, 100411(R) (2010).
- <sup>9</sup>B. Lorenz, Y.-Q. Wang, and C.-W. Chu, *Phys. Rev. B* **76**, 104405 (2007).
- <sup>10</sup>S. M. Feng, Y. S. Chal, J. L. Zhu, N. Manivannan, Y. S. Oh, L. J. Wang, Y. S. Yang, C. Q. Jin, and K. H. Kim, *New J. Phys.* **12**, 073006 (2010).
- <sup>11</sup>H. W. Brinks, J. Rodriguez-Carvajal, H. Vjellvag, A. Kjekshus, and B. C. Hauback, *Phys. Rev. B* **63**, 094411 (2001).
- <sup>12</sup>A. Munoz, M. T. Casais, J. A. Alonso, M. J. Martinez-Lope, J. L. Martinez, and M. T. Fernandez-Diaz, *Inorg. Chem.* **40**, 1020 (2001).
- <sup>13</sup>A related scenario is realized in YMn<sub>2</sub>O<sub>5</sub>; see L. C. Chapon, P. G. Radaelli, G. R. Blake, S. Park, and S.-W. Cheong, *Phys. Rev. Lett.* **96**, 097601 (2006).
- <sup>14</sup>Y. Tokunaga, N. Furukawa, H. Sakai, Y. Taguchi, T. Arima, and Y. Tokura, *Nat. Mater.* **8**, 558 (2009).
- <sup>15</sup>A. Stroppa, M. Marsman, G. Kresse, and S. Picozzi, *New J. Phys.* **12**, 093026 (2010).
- <sup>16</sup>N. Aliouane, O. Prokhnenko, R. Feyerherm, M. Mostovoy, J. Strempher, K. Habicht, K. C. Rule, E. Dudzik, A. U. B. Wolter, A. Maljuk, and D. N. Argyriou, *J. Phys. Condens. Matter* **20**, 434215 (2008).
- <sup>17</sup>M. Mochizuki, N. Furukawa, and N. Nagaosa, *Phys. Rev. Lett.* **105**, 037205 (2010).

## Appendix III.

### Direct observation of the proliferation of ferroelectric dislocation loops and vortex-antivortex pairs

S. C. Chae<sup>1</sup>, N. Lee<sup>1</sup>, Y. Horibe<sup>1</sup>, M. Tanimura<sup>2</sup>, S. Mori<sup>3</sup>, B. Gao<sup>1</sup> and S.-W. Cheong<sup>1\*</sup>

<sup>1</sup>Rutgers Center for Emergent Materials and Department of Physics and Astronomy, Rutgers, The State University of New Jersey, Piscataway, NJ 08854

<sup>2</sup>Research Department, NISSAN ARC Ltd., Yokosuka, Kanagawa 237-0061, Japan

<sup>3</sup>Department of Materials Science, Osaka Prefecture University 1-1, Sakai, Osaka 599-8531, Japan, and JST, CREST, 1-1, Sakai, Osaka 599-8531, Japan.

\*e-mail: sange@physics.rutgers.edu

**We have discovered “stripe” patterns of antiphase-ferroelectric domains in hexagonal REMnO<sub>3</sub> (RE=Ho, Er, Tm, Yb, Lu) crystals (grown below ferroelectric transition temperatures, reaching up to 1435 °C), in contrast with the vortex patterns in hexagonal YMnO<sub>3</sub>. The appearance of a zoo of dislocation loops, resembling dislocation pairs, is observed with sufficient thermal fluctuations, but the stripe domain patterns turn to vortex-antivortex domain patterns when crystals cross T<sub>c</sub>. The experimental systematics are compared with the results of our six-state clock model simulation and also the Kibble-Zurek Mechanism for trapped topological defects.**

The subtle phase transitions straddling the delicate boundary between long-range-order and disorder have attracted significant attention due to the fundamental science and the tantalizing technological perspective [1]. For example, the ground state of two-dimensional (2D) spins with planar continuous degrees of freedom undergoes only quasi-long-range-order with spin-spin correlations falling off algebraically in space, and becomes a high-temperature disorder state with exponentially-decaying correlations through the so-called Kosterlitz-Thouless (KT) transition by the proliferation of unbound topological vortices [2, 3]. Not only the KT transition

in 2D planar spins but also various phenomena such as 2D melting and roughening transition at surface are associated with the emergence of a topological order, resulting from the binding of topological defects [4, 5]. Even though the ordering issue of 2D condensed matters is a time-honored topic, the topological ordering process in “large-scale real space” has little investigated experimentally. Furthermore, it is a profound question how the topological KT order is influenced by the 3<sup>rd</sup>-dimensional coupling and quenched disorder that exists often in real systems.

In order to understand the evolution between quasi-long-range-order and long-range-order, the so-called q-state clock model has been investigated extensively. The q-state clock model consists of 2D planar spins where the spins are restricted to q evenly-spaced orientations [6]. At low temperatures, there exists an ordered phase with long-range correlations when q is small. However, convincing evidence has been amassed, based both on qualitative and quantitative considerations, to indicate that for large enough q (thought to be  $5 \leq q < 8$ ) there exists an intermediate phase similar to the KT phase [7]. The q-state clock model with  $q \geq 8$  precisely reproduces the KT transition [8]. In the case of 2D melting problem [4], this intermediate phase is a hexatic phase with orientational correlations falling off algebraically and positional correlations exponentially [2, 9]. This hexatic phase is created from a low-temperature ordered state by the dissociation of dislocation pairs, and becomes a high-temperature disordered phase by the dissociation of disclination pairs, related with vortex-antivortex pairs. Note that a similar intermediate phase can exist in roughening transitions at surfaces [5].

Layered hexagonal  $\text{YMnO}_3$  is an improper ferroelectric where the size mismatch between Y and Mn-O layers induces a trimerization-type structural phase transition, and this structural transition leads to three antiphase domains ( $\alpha, \beta, \gamma$ ), each of which can support two directions (+, -) of ferroelectric polarization [10, 11]. The antiphase and ferroelectric domains of  $\text{YMnO}_3$  meet in cloverleaf arrangements that cycle through all six domain configurations. Occurring in pairs, the cloverleaves can be viewed as vortices and antivortices, in which the cycle of domain configurations is reversed [12]. Large-scale arrangements of topological vortices and antivortices in  $\text{YMnO}_3$  reveal intriguing real space domain patterns with mathematical simplicity, which can be analyzed with graph theory [13]. The six possible characteristics of domains, combined

with the layered structure of hexagonal  $\text{YMnO}_3$ , suggest the analogy between the 2D six-state clock model and the physics of  $\text{YMnO}_3$ . In the six-state clock model, it has been claimed the presence of three phases; long-range ordered (LRO) phase, intermediate KT phase, and high-temperature disordered phase [7]. However, vortex-antivortex domain patterns have been observed in  $\text{YMnO}_3$  at room temperature far below structural transition temperature, which suggests the intermediate KT phase, rather than a LRO phase, as the ground state.

Herein, in order to unveil the origin of this inconsistency, we have studied the systematics of domain configurations in a series of hexagonal  $\text{RE}\text{MnO}_3$  (RE=rare earths) crystals grown with a flux method, and also the thermal evolution of the domain configurations. In order to reveal domain patterns, thin-plate-like crystals with optically flat surfaces were etched chemically in phosphoric acid. The domain patterns of chemically-etched crystals were investigated using optical microscopy (OM), transmission electron microscopy (TEM) and atomic force microscopy (AFM). Note that preferential chemical etching of surface areas with upward polarization enables the observation of ferroelectric domain patterns on a crystal surface using OM or AFM. (see the detailed experimental method in the supplementary.)

Unlike vortex-antivortex domain patterns in  $\text{YMnO}_3$ , stripe domain patterns with large downward (-) polarization domains are discovered in most of  $\text{RE}\text{MnO}_3$  crystals. The OM image of a stripe domain pattern on one entire surface of an  $\text{ErMnO}_3$  crystal is shown in Fig. 1(a). These stripe lines in the OM image are identified as narrow trenches with the depth of  $\sim 500$  nm as revealed in AFM scans (see the inset of Fig. 1(a)), and tend to be along the  $[110]$  direction (the hexagonal  $P6_3cm$  notation). These trenched lines correspond to narrow upward (+) polarization domains [13]. These stripe domain patterns are distinct from the topological vortex-antivortex domain pattern with small domains in  $\text{YMnO}_3$ , shown in Fig. 1(b). In the vortex-antivortex domain pattern in  $\text{YMnO}_3$ , a vortex consists of six trimerization antiphase ( $\alpha$ ,  $\beta$ ,  $\gamma$ ) and ferroelectric (+,-) domains merging at the center of the vortex, and is paired with an antivortex (or antivortices) with the opposite vorticity in terms of structural antiphase and ferroelectric relationship as shown in the inset of Fig. 1(b) [13]. On the other hand, the stripe domain pattern in Fig. 1(a) spans the entire crystal surface, and we have, in fact, observed only these stripe domain patterns without any hint of the presence of vortices in all  $\text{RE}\text{MnO}_3$  (RE=Ho, Er, Tm, Yb,

Lu, but not Y) crystals. We also note that the stripe domain patterns with large downward-polarization domains appear to be consistent with an LRO phase, rather than the topological KT phase. As discussed below, this striking difference between stripe and vortex-antivortex domain patterns originates entirely from if the crystal growth temperature is above the structural transition temperature ( $T_c$ ) or not.

In order to explore the thermal evolution of these stripe domain patterns, we quenched crystals from various temperatures and then etched them chemically. Figure 2(a) displays the AFM image of a chemically-etched  $\text{ErMnO}_3$  surface after quenching from 1120 °C. Even though the equilibrating temperature is very high, the LRO stripe domain pattern changes little. However, when the temperature is raised by only 20 °C, the pattern changes significantly, and exhibits highly-curved lines with the appearance of many curved closed loops, as shown in Fig. 2(b). These closed loops resembles crystallographic dislocation loops observed in silicon carbide, oxides and liquid crystals [14]. Dark stripe lines, conserved robustly up to 1120 °C, start to wiggle heavily at 1140 °C, but never cross to each other, i.e., there is no hint of the presence of vortices in the entire crystal surface (see the supplementary section 2 and Fig. S2.). The more-or-less straight parts of dark stripe lines are indicated with white dashed lines in the upper region of Fig. 2(b). TEM image of closed loop domains is shown in Fig. 2(c), and the corresponding possible schematic is shown in Fig. 2(d). When counted along the arrow in Fig. 2(d), each closed loop consists of a pair of  $(\alpha, \beta, \gamma)$  and  $(\gamma, \beta, \alpha)$  domains with the opposite structural phase shifts, so it can be viewed as a dislocation pair. Therefore, when the system approaches  $T_c$  from blow, thermal fluctuations induce a large number of dislocation pairs in the form of dislocation loops in stripe domains.

When the temperature is further raised by 30 °C, the pattern becomes complicated as shown in Fig. 2(e), and in fact shows the crossing of lines and the presence of a large number of vortices. This vortex-antivortex domain pattern formation is more evident when the quenching temperature was raised to 1200 °C, as shown in Fig. 2(f). We have determined  $T_c$ 's at which stripe domain patterns turn into vortex-antivortex domain patterns for all  $\text{RE}\text{MnO}_3$  (RE=Ho, Er, Tm, Yb, Lu) from similar quenching experiments, which are plotted in the inset of Fig. 2(f).  $T_c$  of  $\text{YMnO}_3$  reported earlier is also plotted in the inset [15]. The rough linear dependence in the

inset strongly suggests that  $T_c$  at which stripe domain patterns turn into vortex-antivortex domain patterns is, indeed, the structural  $T_c$  of  $\text{RE}\text{MnO}_3$ . Note that  $T_c$ 's of  $\text{RE}\text{MnO}_3$  ( $\text{RE}=\text{Ho}, \text{Er}, \text{Tm}, \text{Yb}, \text{Lu}$ ) have never been reliably determined because of the very high temperature nature, and  $T_c$  drastically increases with decreasing RE size, which is consistent the notion that the structural transition is induced by the mismatch between small RE layers and large Mn-O layers in the  $\text{RE}\text{MnO}_3$  structure. Note that  $\text{RE}\text{MnO}_3$  crystals were grown by slow cooling of the materials with  $\text{Bi}_2\text{O}_3$  flux in the temperature range of 1200 °C and 950 °C, but the real growth through nucleation occurs probably slightly above 950 °C. Thus,  $\text{Y}\text{MnO}_3$  crystals are likely grown above  $T_c$ , but other  $\text{RE}\text{MnO}_3$  crystals below  $T_c$ . Therefore, it appears that stripe domain patterns form when the crystal growth temperature is below  $T_c$  while vortex-antivortex domain patterns are realized when crystals are exposed to temperatures above  $T_c$ .

Interestingly, we found that once vortex-antivortex domain patterns, spanning the entire crystal surface (see the supplementary section 3 and Fig. S3), form by crossing  $T_c$ , they are conserved with various thermal treatments, but the domain size of vortex-antivortex domain patterns or the distance between vortices and antivortices can vary in a systematic manner. In order to find out the thermal evolution of vortex-antivortex domain patterns and the domain growth kinetics, the cooling rate near  $T_c$  was changed from 0.5 °C/h to 300 °C/h. In addition, we cooled one specimen from 1220 °C to 677 °C with cooling rate of 5 °C/h, followed by quenching to room temperature. Figures 3(a), (b), (c) and (d) show the AFM images of etched  $\text{ErMnO}_3$  crystals with the above thermal treatments. With the large variation of cooling rate from 0.5 °C/h to 300 °C/h, vortex-antivortex domain patterns remain intact, but the domain size of vortex-antivortex domain patterns changes systematically.

We emphasize that the vortex-antivortex domain patterns in Figs. 3(b) and (c) are basically identical, indicating that the cooling rate below 677 °C does not influence the domain patterns. This is an important result for the origin of the mysterious second transition near 600 °C reported in many early publications [11, 15, 16, 17, 18]. This second transition at ~600 °C was identified as the ferroelectric transition from centrosymmetric  $P6_3/mmc$  to low-temperature polar  $P6_3cm$  structures via an intermediate  $P6_c/mcm$  structure [16] whereas other results argued for the nonexistence of intermediate  $P6_3/mcm$  state, but the presence of an isosymmetric phase transition

with Y-O hybridization [11, 15, 17]. We, in fact, compared directly vortex-antivortex domain patterns at room temperature and 730 °C from TEM dark-field experiments using the  $1\bar{1}1$  diffraction spot as shown in Figs. 4(a) and (b). Basically there is little difference between two vortex-antivortex domain patterns, which, combined with no difference in vortex-antivortex domain patterns on cooling rate across the second transition temperature, are consistent with the possibility of an isosymmetric change at the second transition if it exists.

The analysis of the evolution of domain size of vortex-antivortex domain patterns with varying cooling rate demonstrates slow growth kinetics associated with the topological vortex-antivortex domain patterns. The average distance of vortex-antivortex pairs vs. inverse cooling rate,  $t$ , is plotted in Fig. 4(c). The cooling rate dependence of the average vortex-antivortex pair distance,  $D$ , can be described by  $D \propto t^n$  with  $n=0.23$  (See the supplementary section 4 and Fig. S4). This value of  $n \approx 1/4$  is rather different from the typical parabolic domain growth value of  $n=1/2$  [19]. This slow growth kinetics with vortex-antivortex domain patterns seem consistent with the Kibble-Zurek Mechanism for spontaneous trapping of topological defects in a system undergoing a continuous phase transition [20, 21]. For the average vortex-antivortex pair distance  $\propto t^n$  with  $n \approx 1/4$ , the density of vortex should vary like  $t^{1/2}$ , which is precisely the prediction of the Kibble-Zurek mechanism with mean field critical exponents [21]. We also note that chemical/structural-defects-induced pinning may play an important role for the variation of the vortex-antivortex distance with cooling rate. In fact, strong pinning tendency of domain patterns has been observed in many of our results. For example, the domain patterns in Fig. 2(a) and Fig. 4(b) change little with expected large thermal fluctuations at temperatures such as 1120 °C and 730 °C. In addition, we have directly observed vortex-antivortex domain patterns pinned by large-scale surface defects, as shown in Fig. 4(d). Strong pinning, slow kinetics, and the different topology between vortex-antivortex and stripe domain patterns induce probably an “astronomical” time scale for the conversion of vortex-antivortex domain patterns to stripe domain patterns, even though the true ground state corresponds to stripe domain patterns.

The concept of topological KT order with binding vortices and antivortices was originally developed for the quasi-long-range-order in 2D XY systems. In the case of the 2D six-state clock model, the topological order exists only in an intermediate temperature range, and the ground

state is a LRO phase (see the supplementary section 5 and Fig. S5.). Any 3<sup>rd</sup> dimensional coupling will destabilize the intermediate KT phase in the six-state clock model. Therefore, one expects theoretically that a LRO phase will be the ground state of hexagonal REMnO<sub>3</sub> with six degrees of freedom, and the intermediate KT order may or may not exist, depending on the strength of 3<sup>rd</sup> directional coupling. Our results indicate that the LRO ground state with stripe domain patterns can be observed, but only when crystals were grown below  $T_c$ . When crystals were grown from temperatures above  $T_c$  or crystals with stripe domain patterns were exposed to a temperature above  $T_c$ , domain patterns are always vortex-antivortex domain patterns. In addition, we have observed convincing evidence for strong pinning and also slow kinetics associated with domain patterns. Furthermore, our results do not show any indication for two step transitions from an long-range order to a KT order to disorder. Therefore, it is convincing that there exists only one LRO transition associated with six degrees of freedom. However, in any real situations without astronomical-time-scale annealing, slow kinetic creation of topological defects, which is well manifested in the Kibble-Zurek mechanism, and their strong pinning induce KT-type vortex-antivortex domain patterns when crystals undergoes the structural transition at  $T_c$ . In other words, a KT order is only implicit in hexagonal REMnO<sub>3</sub> and should not occur as the ground state, but it is arrested by slow kinetic and strong pinning. This “arresting” scenario is fully consistent with our simulation of the 2D six-state clock model with different cooling rates (see the supplementary section 5 and Fig. S5.).

In summary, the true ground state with stripe domain patterns can be realized when hexagonal REMnO<sub>3</sub> (RE=Ho, Er, Tm, Yb, Lu) crystals are grown below  $T_c$ , and is consistent with the long-range-ordered ground state of the six-state clock model with a significant 3<sup>rd</sup> dimensional coupling. When crystals are approached to  $T_c$  from below, a zoo of dislocation loops, which can be viewed as dislocation pairs, appear. However, once crystals cross  $T_c$ , domain patterns with topological vortices and antivortices are realized. These vortex domains can be enlarged with the time exponent of 1/4, which is much smaller than the typical domain growth exponent of 1/2. It is conceivable that the topological KT-type vortex-antivortex domain patterns eventually turn into long-range-ordered stripe domain patterns through astronomical-time-scale annealing. Therefore, the presence of stripe domain patterns in REMnO<sub>3</sub> crystals grown below  $T_c$



is an experimental marvel, enabling the observation of unbound dislocation loops as well as vortex-antivortex pairs.

## References

- [1] C. H. Chen, J. M. Gibson, and R. M. Fleming, Phys. Rev. Lett. **47**, 723 (1981); A. Del Maestro, B. Rosenow, and S. Sachdev, Phys. Rev. B **74**, 024520 (2006); I. F. Herbut, and Z. Tešanović Phys. Rev. Lett. **73**, 484 (1994); O. Tchernyshyov, and G.-W. Chern, Phys. Rev. Lett. **95**, 197204 (2005); S. Larochelle, M. Ramazanoglu, and R. J. Birgeneau, Phys. Rev. E **73**, 060702 (2006).
- [2] J. M. Kosterlitz, and D. J. Thouless, J. Phys. C **6**, 1181 (1973).
- [3] D. R. Nelson, and J. M. Kosterlitz, Phys. Rev. Lett. **39**, 1201 (1977); V. Berezinskii, Sov. Phys. JETP **34**, 610 (1972).
- [4] B. I. Halperin, and D. R. Nelson, Phys. Rev. Lett. **41**, 121 (1978).
- [5] B. Kahng, and K. Park, Phys. Rev. B **47**, 5583 (1993).
- [6] D. J. Srolovitz, and J. F. Scott, Phys. Rev. B **34**, 1815 (1986); G. S. Grest, and D. J. Srolovitz, Phys. Rev. B **30**, 6535 (1984).
- [7] M. B. Einhorn, R. Savit, and E. Rabinovici, Nucl. Phys. B **170**, 16 (1980).
- [8] C. M. Lapilli, P. Pfeifer, and C. Wexler, Phys. Rev. Lett. **96**, 140603 (2006); S. K. Baek, P. Minnhagen, and B. J. Kim, Phys. Rev. E **80**, 060101 (2009).
- [9] N. N. Negulyaev *et al.*, Phys. Rev. Lett. **102**, 246102 (2009).
- [10] B. B. Van Aken *et al.*, Nature Mater. **3**, 164 (2004); M. Fiebig *et al.*, Nature **419**, 818 (2002).
- [11] T. Katsufuji *et al.*, Phys. Rev. B **64**, 104419 (2001).
- [12] T. Choi *et al.*, Nature Mater. **9**, 253 (2010).
- [13] S. C. Chae *et al.*, Proc. Nat. Acad. Sci. U. S. A. **107**, 21366 (2010).

- [14] M. J. Bowick *et al.*, *Science* **263**, 943 (1994); C. L. Kelchner, S. J. Plimpton, and J. C. Hamilton, *Phys. Rev. B* **58**, 11085 (1998); P. O. A. Persson *et al.*, *J. Appl. Phys.* **100**, 053521 (2006); Y. C. Wu *et al.*, *J. Am. Ceram. Soc.* **89**, 2213 (2006).
- [15] A. S. Gibbs, K. S. Knight, and P. Lightfoot, *Phys. Rev. B* **83**, 094111 (2011).
- [16] G. Nénert, and *et al.*, *J. Phys.: Condens. Matter* **19**, 466212 (2007); I. Ismailzade, and S. Kizhaev, *Sov. Phys.-Solid State* **7**, 236 (1965).
- [17] K. Lukaszewicz, and J. Karut-Kalici ska, *Ferroelectrics* **7**, 81 (1974); T. Lonkai *et al.*, *Phys. Rev. B* **69**, 134108 (2004); C. J. Fennie, and K. M. Rabe, *Phys. Rev. B* **72**, 100103 (2005).
- [18] N. Fujimura *et al.*, *Appl. Phys. Lett.* **69**, 1011 (1996).
- [19] G. S. Grest, M. P. Anderson, and D. J. Srolovitz, *Phys. Rev. B* **38**, 4752 (1988).
- [20] T. W. B. Kibble, *J. Phys. A: Math. Gen.* **9**, 1387 (1976).
- [21] W. H. Zurek, *Nature* **317**, 505 (1985).

### Figure legends

**FIG 1.** (color online). Two distinct domain patterns of  $\text{RE}\text{MnO}_3$  crystals; stripe vs. vortex patterns. (a) optical microscope image of a chemically-etched  $\text{ErMnO}_3$  crystal surface. The inset shows the atomic force microscope (AFM) image of a stripe domain pattern after chemical etching. These domain patterns for a long-range ordered phase are also observed in  $\text{HoMnO}_3$ ,  $\text{TmMnO}_3$ ,  $\text{YbMnO}_3$ ,  $\text{LuMnO}_3$  crystals, as shown in Fig. S1 in Supplementary. (b) Optical microscope image of a chemically-etched  $\text{YMnO}_3$  crystal surface. The inset shows the AFM image of an  $\text{YMnO}_3$  surface after chemical etching, showing a vortex-antivortex domain pattern. Vortex and antivortex are distinguished by the arrangement of trimerization antiphase and ferroelectric domains with the opposite sense of rotation around a core. Note that the entire surfaces of all as-grown crystals  $\text{RE}\text{MnO}_3$  ( $\text{RE}=\text{Ho}, \text{Er}, \text{Tm}, \text{Yb}, \text{Lu}$ ) exhibit no hint of the presence of any vortices or antivortices.

**FIG 2.** (color online). The thermal evolution of stripe domain patterns in  $\text{ErMnO}_3$ ; the creation of dislocation loops and vortex-antivortex pairs. (a), (b), (e) and (f), The AFM images of chemically-etched  $\text{ErMnO}_3$  crystals quenched from 1120 °C, 1140 °C, 1170 °C, and 1200 °C, respectively. A large number of dislocation loops are evident in (b), but (e) and (f) display vortex-antivortex patterns. The inset displays  $T_c$ 's of  $\text{RE}\text{MnO}_3$  estimated from the formation temperature of vortex-antivortex domain patterns.  $T_c$  of  $\text{YMnO}_3$  is from ref. [15]. (c) and (d), TEM image of dislocation loops of  $\text{ErMnO}_3$  quenched from 1140 °C and a possible corresponding schematic, respectively. The dislocation-loop domains observed in the TEM image are assigned with three antiphase domains ( $\alpha, \beta, \gamma$ ).

**FIG 3.** (color online). The evolution of vortex-antivortex domain patterns with varying cooling rate. The AFM images of chemically-etched  $\text{ErMnO}_3$  crystals; (a) cooled from 1220 °C to 890 °C with rate of 0.5 °C/h, followed by furnace cooling, (b) cooled from 1200 °C to room temperature with rate of 5 °C/h, (c) from 1200 °C to 677 °C with rate of 5 °C/h, followed by quenching, and (d) from 1200 °C to room temperature with rate of 300 °C/h.

**FIG 4.** (color online). The pinning of vortex-antivortex domains. (a) and (b) TEM images of vortex-antivortex domain patterns of  $\text{ErMnO}_3$  at room temperature and 730 °C, respectively. (c)

The cooling rate dependence of the average distance of vortex-antivortex pairs, exhibiting a power law dependence with the power of 0.23. (The open triangle is from Fig 3(c)). (d) The optical microscope and AFM (inset) images of a chemically-etched  $\text{ErMnO}_3$  crystal surface, suggesting strong pinning of vortex-antivortex domains by surface defects.

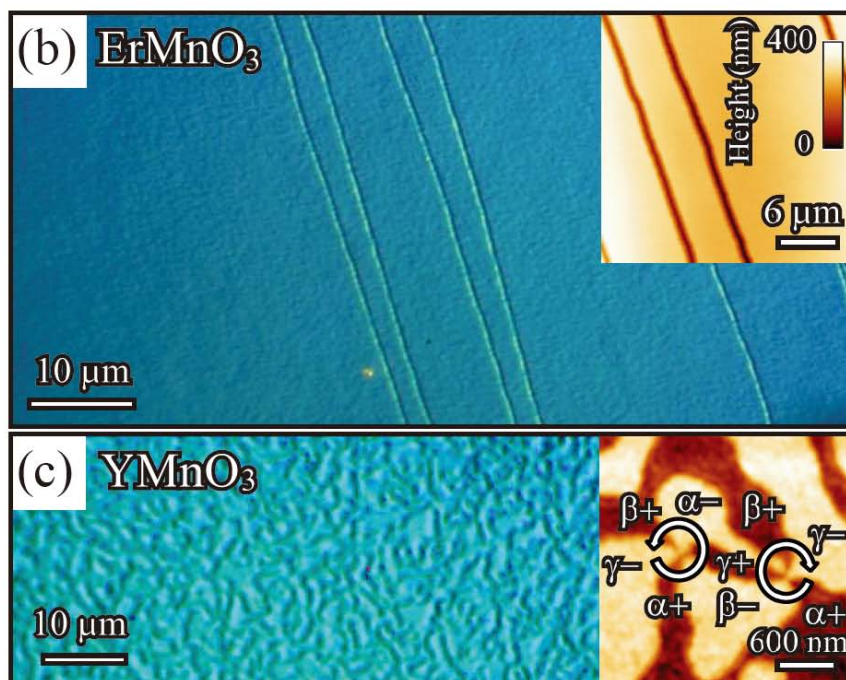


Figure 1

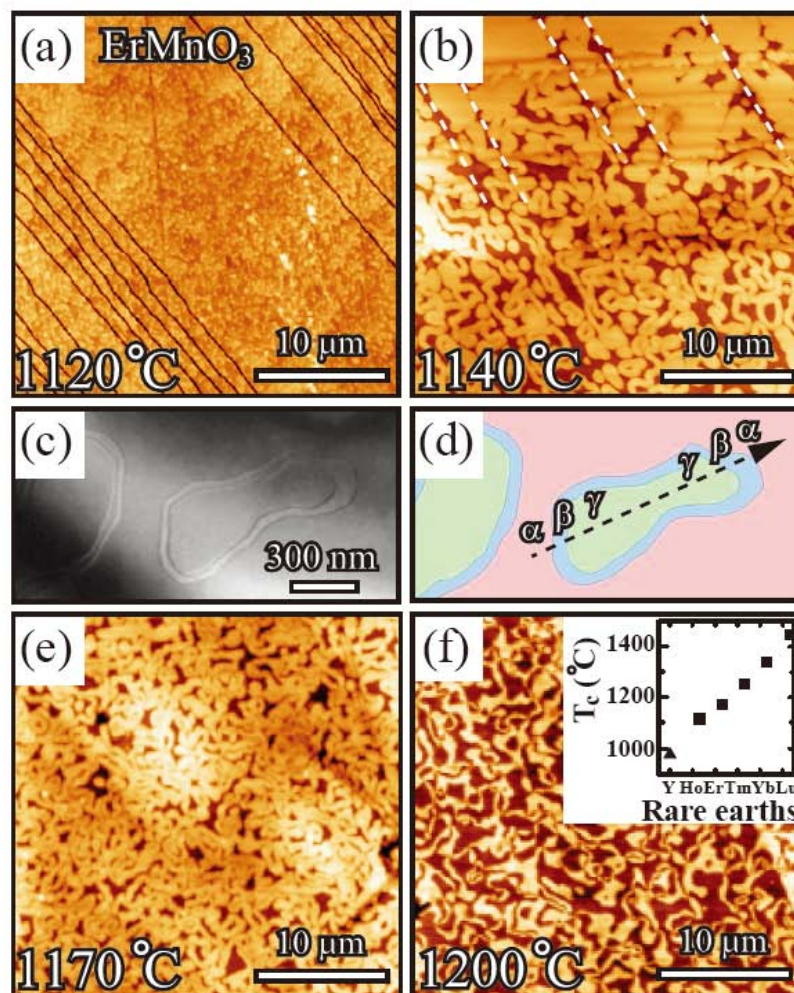


Figure 2

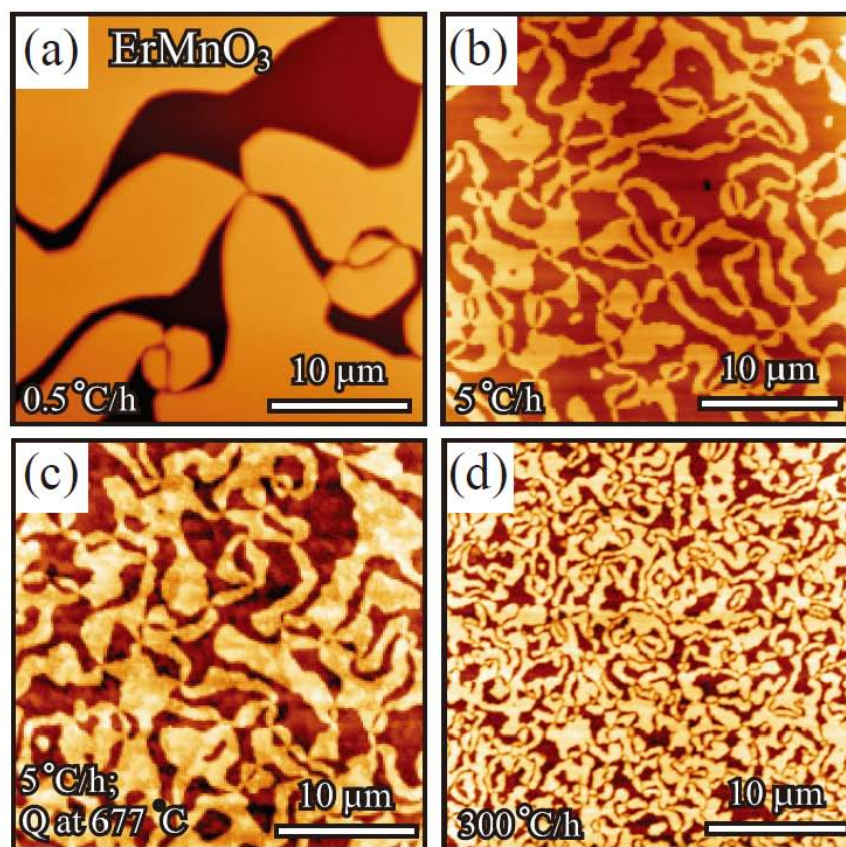


Figure 3



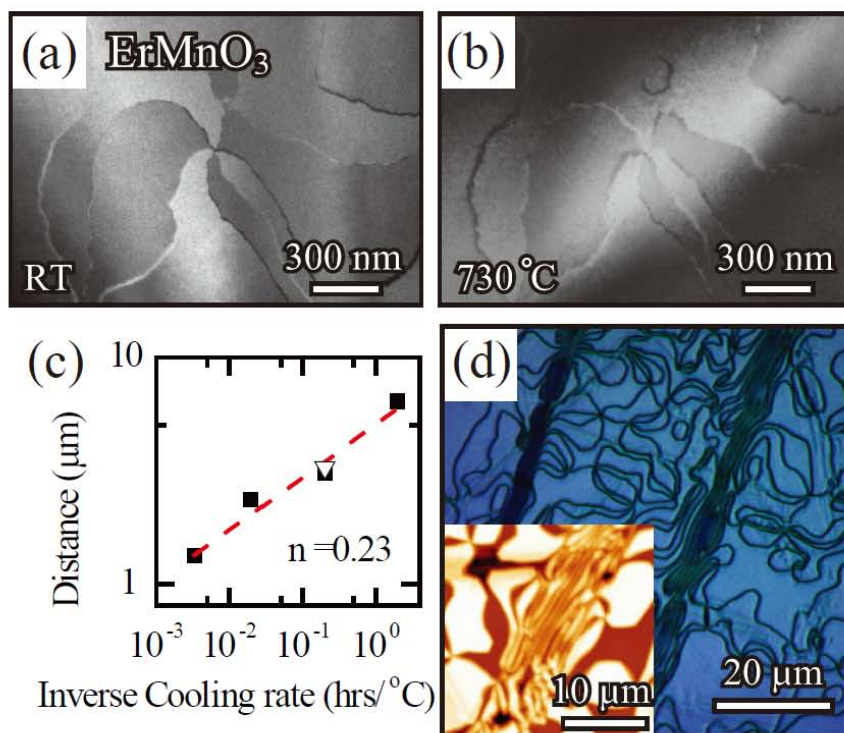


Figure 4

## Appendix IV.

### Collective magnetism at ferroelectric vortex domain walls

Yanan Geng, N. Lee, Y.J. Choi<sup>1</sup>, S-W. Cheong and Weida Wu

*Department of Physics and Astronomy and Rutgers Center for emergent materials, Rutgers University, Piscataway, NJ 08854 USA*

Topological defects are pervasive in complex matter such as superfluids, liquid crystals, earth atmosphere, and early universe<sup>1,2</sup>. They have been fruitful playgrounds for emergent phenomena<sup>3,4</sup>. Recently, vortex-like topological defects with six interlocked structural antiphase and ferroelectric domains merging into a vortex core were revealed in ferroelectric hexagonal manganites<sup>5</sup>. Numerous ferroelectric vortices are found to form a self-organized network<sup>6</sup>. The intriguing manganites do contain mutually-interacting magnetic ions, and thus it is imperative to find out the magnetic nature of the ferroelectric vortices and their network. Using cryogenic magnetic force microscopy in applied magnetic fields ( $H$ )<sup>7</sup>, we discovered that the alternating domain wall magnetizations around vortices can correlate over the entire vortex network. Furthermore, the magnetic configuration of the entire vortex network can be switched reversibly with changing  $H$ . The collective nature of the vortex-network magnetism appears originated from the presence of uncompensated magnetic moments at domain walls, the  $H$ -controllable chirality of magnetic domains, and the correlated organization of the vortex network. Our results not only open the possibilities of detecting chirality of spin order with the observation of domain wall magnetism, but also pave the way for nanoscale exploration of the magnetoelectric interplay in single-phase multiferroics.

---

<sup>1</sup> Present address: Department of Physics and IPAP, Yonsei University, Seoul 120-749, Korea

Multiferroics are materials with coexisting magnetism and ferroelectricity<sup>8,9</sup>. The cross-coupling between two ferroic orders can result in giant magnetoelectric coupling for potential applications<sup>10-13</sup>. Because formation of domains is the hallmark of any ferroic order<sup>14</sup>, it is of both fundamental and technological interests to visualize cross-coupled domains or walls in multiferroics. Hexagonal (*h*-) *RE*MnO<sub>3</sub> (*RE* = Sc, Y, Ho, ... Lu) are multiferroics with coexistence of ferroelectricity ( $T_C \approx 1200 - 1500$  K)<sup>15</sup> and antiferromagnetism ( $T_N \approx 70 - 120$  K)<sup>16</sup>. The ferroelectricity is induced by structural instability called trimerization<sup>17</sup>, which lifts presumably the frustration of antiferromagnetic interactions of Mn<sup>3+</sup> spins on triangular lattice. Indeed, a 120° antiferromagnetic order of Mn<sup>3+</sup> spin in the *ab*-plane sets in below  $T_N$ . Recently, an intriguing 6-state vortex domain structure in YMnO<sub>3</sub> is revealed by transmission electron microscopy, conductive atomic force microscopy and piezoresponse force microscopy (PFM) at room temperature<sup>5,18</sup>. Fig. 1a shows a typical room temperature PFM image of (001) surface of *h*-ErMnO<sub>3</sub> single crystal, where six alternating up (red) and down (blue) ferroelectric domains merge into vortex cores. The formation of 6-state vortices originates from the cyclic arrangement of 6 interlocked structural antiphase ( $\alpha, \beta, \gamma$ ) and ferroelectric (+/-) ground states (i.e.  $\alpha^+, \beta^-, \gamma^+, \alpha^-, \beta^+, \gamma^-$ )<sup>5,19</sup>. The intriguing network of vortex-antivortex pairs has a profound connection to graph theory, where 6-valent planer graphs with even-gons are two-proper-colorable<sup>6</sup>. Using second harmonic generation optics, it has been claimed that ferroelectric domain walls (DWs) in millimeter-size YMnO<sub>3</sub> tend to pin antiferromagnetic DWs, but free antiferromagnetic DWs also exist<sup>20</sup>. Thus, it is of great interest to find out the magnetic nature of vortex domains and walls. However, this has been an experimental challenge, particularly due to the lack of suitable high resolution imaging technique of antiferromagnetic domains or walls for *h*-*RE*MnO<sub>3</sub> at low temperatures (Supplementary discussion 1). To address this issue, we investigated the spatially-resolved magnetic structure of *h*-ErMnO<sub>3</sub> crystals with magnetic Er<sup>3+</sup> ions using a low-temperature magnetic force microscope<sup>7</sup>.

Figure 1b shows a MFM image ( $18 \times 18 \mu\text{m}^2$ ) of (001) surface of *h*-ErMnO<sub>3</sub> taken at the *same* location as the black box in PFM image (fig. 1a) at 5.5 K in 0.2 T out-of-plane magnetic field after 0.2 T field cooling from  $T > T_N$ . The MFM image is aligned with the PFM image using topographic features as alignment marks (supplementary fig. S1). Clearly, there are line features (width  $\sim 400$  nm) with alternating bright and dark color in MFM image, overlapping with ferroelectric DWs in the PFM image. The single peak profile of MFM signal (i.e. stray field gradient, supplementary fig. S2) suggests that local net moments at DWs are parallel to the *c*-axis. In addition, the alternating MFM signal at DWs correlate over the entire field of view, suggesting a collective nature of the DW magnetism. Since Mn<sup>3+</sup> spins in ErMnO<sub>3</sub> are 120°-ordered below  $T_N \approx 80$  K, no net moment is expected inside antiferromagnetic domains<sup>21</sup>. Naturally, these net moments at ferroelectric DWs come from the uncompensated moments at antiferromagnetic domain boundaries. Note that the MFM contrast of DWs is essentially constant in 0.02 – 0.9 T, which excludes the possibility of local susceptibility differences as the origin<sup>22</sup>. Therefore, our results provide compelling evidence that uncompensated moments are coupled to the interlocked structural antiphase and ferroelectric DWs interconnecting vortices,

which are truly multiferroic<sup>6</sup>. An example of one multiferroic vortex is highlighted by the green boxes in fig. 1a and b, and is shown in a perspective view in fig. 1c. The alternating orientations of uncompensated moments around a vortex core are illustrated by the arrows above the PFM image. This is similar to alternating ferroelectric polarization of domains around a vortex core, suggesting that there are two types of DWs, noted as DW<sub>I</sub> and DW<sub>II</sub>.

Previous micromagnetic analysis of antiferromagnetic DWs in YMnO<sub>3</sub> suggests oscillatory uncompensated magnetization of Mn<sup>3+</sup> spins across the antiferromagnetic-ferroelectric DW in the *ab*-plane due to in-plane anisotropy of Mn<sup>3+</sup> spins<sup>23</sup>, which is inconsistent with our MFM results of ErMnO<sub>3</sub>. Therefore, the observed uncompensated moments in ErMnO<sub>3</sub> likely come from Er<sup>3+</sup> spins. To confirm it, we took MFM images at the same location for various temperatures, as shown in fig. 2 and supplementary fig. S3. The DW contrast, defined as the difference between bright and dark DWs, decreases sharply for  $T < 20$  K, then slowly at higher temperature as shown in fig. 2g. We obtained a good fit (red curve in fig. 2g) of the temperature dependence of DW contrast using a simple model where the effective doublet ground state of Er<sup>3+</sup> is split by antisymmetric exchange fields from neighboring Mn<sup>3+</sup> spins<sup>24</sup>. It is believed that the effective exchange fields originate from Dzyaloshinskii-Moriya (DM) interactions because dipolar interactions from Mn<sup>3+</sup> moments are too weak<sup>24</sup>. However, dipolar interaction may be responsible for the additional  $RE^{3+}$  ordering below 10 K<sup>21,24</sup>. The doublet model has successfully explained bulk (i.e. domain)  $RE^{3+}$  magnetism probed by x-ray magnetic resonant scattering, neutron diffraction and Mössbauer spectroscopy<sup>24-26</sup>. The good fitting of our MFM data suggests that DM interactions are also responsible for the DW magnetism which is difficult to study with bulk probes. Indeed, the DW contrast diminishes at ~80 K in excellent agreement with  $T_N \approx 80$  K inferred from susceptibility data (inset of fig. 2g).

The DM interaction is the key ingredient for non-collinear spin orders which break inversion symmetry and induces ferroelectricity in many recently discovered multiferroics<sup>8,9</sup>. In multiferroic *h*-REMnO<sub>3</sub>, DM interactions between  $RE^{3+}$  and Mn<sup>3+</sup> spins are responsible for induced partial  $RE^{3+}$  antiferromagnetic order<sup>24-26</sup>. Therefore, the magnetic symmetry of  $RE^{3+}$  order follows that of Mn<sup>3+</sup> order. In zero or low magnetic field, the magnetic point group of 120° order of Mn<sup>3+</sup> spins in ErMnO<sub>3</sub> is  $P\bar{6}_3cm$ , i.e. B<sub>2</sub> (or  $\Gamma_4$ ) (ref. 21). Indeed, the Er<sup>3+</sup> order moments induced by DM interactions also respect B<sub>2</sub> symmetry (supplementary discussion 2 and fig. S4). Earlier studies suggest there are two types of interlocked structural antiphase and ferroelectric DWs which alternate around vortex cores<sup>5</sup>. Assuming atomically sharp Mn<sup>3+</sup> spin variation at DWs and single Mn<sup>3+</sup> spin chirality across DW, uncompensated  $RE^{3+}$  moments can be induced by DM interactions with abrupt structural distortion variation across two different DWs, as shown in fig. 3 (supplementary fig. S5 and discussion 3). In other words, two types of magnetic DWs originate from two types of interlocked structural antiphase and ferroelectric DWs assuming single Mn<sup>3+</sup> spin chirality.

Furthermore, our studies reveal that there are two DW states  $[(DW_I, DW_{II}) = (\uparrow, \downarrow) \text{ or } (\downarrow, \uparrow)]$  which can be controlled by field cooling sample through  $T_N$  with different magnetic field orientations (supplementary fig. S6). We define the DWs with dark (bright) color in MFM image, i.e. uncompensated moment parallel (anti-parallel) with the orientation of cooling magnetic field ( $H$ ) as  $DW_I$  ( $DW_{II}$ ). Note that there are two degenerate (anti-)chiral spin states of  $Mn^{3+}$   $B_2$  symmetry, which are related to each other by time reversal symmetry (supplementary fig. S7), and naturally lead to the two magnetic DW states. Therefore,  $H$ -controlled DW states indicate  $H$ -controlled anti-chiral spin domain states. It is possible that  $DW_I$  has a larger uncompensated magnetization than  $DW_{II}$  around  $T_N$  so that it is always parallel to cooling field. Unambiguous determination of local magnetization of DWs requires further investigation.

To probe the stability of the intriguing magnetic DW states, we performed MFM measurement at 5.5 K at the same location as in fig. 1e and fig. 2 with various magnetic field values after nominal zero field (0.2 T) cooling from  $T > T_N$ . For simplicity, we focus on magnetic field dependence of positive field (0.2 T) cooled “virgin” state, i.e.  $(DW_I, DW_{II}) = (\uparrow, \downarrow)$ . Similar behaviors were observed on the negative field (-0.2 T) cooled “virgin” state. Note that the magnetic moment of MFM tip follows external magnetic field with magnitude larger than the tip coercive field ( $|\mu_0 H_C| \approx 0.02$  T). So MFM signal at negative fields is reversed. As shown in fig. 4a-f and g-l, DW contrast changes sharply at 1.1 T and  $\sim 2.5$  T, suggesting two metamagnetic phase transitions, which is consistent with  $M(H)$  data taken on a crystal from the same batch (supplementary fig. S8a). For quantitative analysis, we define DW contrast as  $\text{sgn}(H) \cdot (\Delta f_I - \Delta f_{II})$ , where the sign function  $\text{sgn}(H)$  accounts for the switching of tip moment by magnetic field and  $\Delta f$  is MFM signal (change of resonant frequency of cantilever) at DWs. As shown in fig. 4m, for both ramping field orientation the DW contrast is practically constant when  $|\mu_0 H| < 1$  T, and changes its sign sharply at 1.1 T, indicating a switching of domain chiral state (supplementary fig. S11). Between 1.1 and 2.5 T, the DW contrast reaches a maximum before decreasing to zero at  $\sim 2.8$  T and varies little at higher magnetic field. Therefore, the DW states are stable in the presence of 1.0 T magnetic field at 5.5 K. The same behavior was reproduced in another location (supplementary fig. S10). More interestingly, we found that the DW contrast is reversible across the first transition, independent of  $H$  orientation as long as  $|H|_{\text{max}} < 2.5$  T. This suggests a remarkable reversibility of  $H$ -controlled domain chiral states. At higher  $H$ 's, the DW state will be switched if the applied field is anti-parallel to cooling field orientation (supplementary fig. S6). The field and temperature dependence of DW states (as well as domain chiral states) are summarized in supplementary fig. S10 (and fig. S11).

Fig. 4n shows an  $H$ - $T$  phase diagram constructed from a systematic  $M(H)$  data set (blue circles) and MFM data (red sphere). The second transition in our phase diagram is excellent agreement with previous studies on  $\text{ErMnO}_3$ , suggesting the high field phase is in  $P6_3cm$  ( $A_2$  or  $\Gamma_2$ ) magnetic symmetry<sup>21</sup>, which allows net magnetization and diagonal magnetoelectric coupling<sup>27</sup>. On the other hand, the first transition suggests that there is an additional intermediate phase characterized by DW magnetization (i.e. domain chiral states) switching, which has never been

reported. If our DW model is correct, the intermediate phase is also in B2 symmetry. Further investigation which can distinguish the two chiral domain states is needed to unambiguously identify the nature of the intermediate phase.

With uniquely correlating ambient PFM and low temperature MFM images, we identified unprecedented collective magnetism, i.e. alternating uncompensated magnetic moments at ferroelectric DWs interconnected through self-organized vortex network in  $h$ -ErMnO<sub>3</sub>. This collective magnetism at ferroelectric walls stems probably from an  $H$ -controllable chiral spin state over the entire sample. Our results also reveal the presence of an intriguing intermediate phase, characterized by reversible switching of DW moments and chiral spin states with  $H$ . Our work not only opens the possibility of probing domain chiral states through DW magnetism, but also paves the way for nanoscale exploration of cross-coupling between multiple orders, and nanoscale domain wall engineering for multifunctional applications.

### References

- 1 Chaikin, P. M. and Lubensky, T. C., *Principles of Condensed Matter Physics*. (Cambridge University Press, Cambridge, UK, 2000).
- 2 Fraisse, A. A., Ringeval, C., Spergel, D. N., and Bouchet, F. R., Small-angle CMB temperature anisotropies induced by cosmic strings. *Physical Review D* **78** (4), 043535 (2008).
- 3 Seidel, J. et al., Conduction at domain walls in oxide multiferroics. *Nat. Mater.* **8**, 229 (2009).
- 4 Mesaros, A. et al., Topological Defects Coupling Smectic Modulations to Intra-Unit-Cell Nematicity in Cuprates. *Science* **333** (6041), 426 (2011).
- 5 Choi, T. et al., Insulating interlocked ferroelectric and structural antiphase domain walls in multiferroic YMnO<sub>3</sub>. *Nature Materials* **9**, 253 (2010).
- 6 Chae, S. C. et al., Self-organization, condensation, and annihilation of topological vortices and antivortices in a multiferroic. *Proceedings of the National Academy of Sciences* **107**, 21366 (2010).
- 7 Park, S. et al., Microscopic evidence of a strain-enhanced ferromagnetic state in LaCoO<sub>3</sub> thin films. *Appl. Phys. Lett.* **95**, 072508 (2009).
- 8 Cheong, S. W. and Mostovoy, M., Multiferroics: a magnetic twist for ferroelectricity. *Nature Materials* **6** (1), 13 (2007).
- 9 Spaldin, N. A., Cheong, S.-W., and Ramesh, R., in *Physics Today* (2010).
- 10 Spaldin, N. A. and Fiebig, M., The Renaissance of Magnetoelectric Multiferroics. *Science* **309**, 391 (2005).
- 11 Eerenstein, W., Mathur, N. D., and Scott, J. F., Multiferroic and magnetoelectric materials. *Nature* **442** (7104), 759 (2006).
- 12 Ramesh, R. and Spaldin, N. A., Multiferroics: progress and prospects in thin films. *Nature Materials* **6** (1), 21 (2007).
- 13 Scott, J. F., Data storage - Multiferroic memories. *Nature Materials* **6** (4), 256 (2007).
- 14 Spaldin, N. A., Fiebig, M., and Mostovoy, M., The toroidal moment in condensed-matter physics and its relation to the magnetoelectric effect. *J. Phys.: Condens. Matter* **20**, 434203 (15pp) (2008).

- 15 Abrahams, S. C., Ferroelectricity and structure in the  $\text{YMnO}_3$  family. *Acta Crystallogr B* **57**, 485 (2001).
- 16 Koehler, W. C., Yakela, H. L., E.O., W., and Cable, J. W., A note on the magnetic structures of rare earth manganese oxides. *Phys. Lett.* **9**, 93 (1964).
- 17 Van Aken, B. B., Palstra, T. T. M., Filippetti, A., and Spaldin, N. A., The origin of ferroelectricity in magnetoelectric  $\text{YMnO}_3$ . *Nature Materials* **3**, 164 (2004).
- 18 Jungk, T., Hoffmann, Á., Fiebig, M., and Soergel, E., Electrostatic topology of ferroelectric domains in  $\text{YMnO}_3$ . *Appl. Phys. Lett.* **97**, 012904 (2010).
- 19 Mostovy, M. *Nature Materials* **9**, 188 (2010).
- 20 Fiebig, M., Lottermoser, T., Frohlich, D., Goltsev, A. V., and Pisarev, R. V., Observation of coupled magnetic and electric domains. *Nature* **419**, 818 (2002).
- 21 Yen, F. et al., Magnetic phase diagrams of multiferroic hexagonal  $\text{RMnO}_3$  (R= Er, Yb, Tm, and Ho). *J. Mater. Res.* **22**, 2163 (2007).
- 22 Israel, C., Wu, W., and Lozanne, A. d., High-field magnetic force microscopy as susceptibility imaging. *Applied Physics Letters* **89**, 032502 (2006).
- 23 Goltsev, A. V., Pisarev, R. V., Lottermoser, T., and Fiebig, M., Structure and Interaction of Antiferromagnetic Domain Walls in Hexagonal  $\text{YMnO}_3$ . *Phys. Rev. Lett.* **90**, 177204 (2003).
- 24 Fabrèges, X. et al., Magnetic order in  $\text{YbMnO}_3$  studied by neutron diffraction and Mössbauer spectroscopy. *Phys. Rev. B* **78**, 214422 (2008).
- 25 Nandi, S. et al., Nature of Ho Magnetism in Multiferroic  $\text{HoMnO}_3$ . *Phys. Rev. Lett.* **100** (21), 217201 (2008).
- 26 Salama, H. A. and Stewart, G. A., Exchange-induced Tm magnetism in multiferroic  $\text{h-TmMnO}_3$ . *J. of Phys.: Condens. Mat.* **21** (38), 386001 (2009).
- 27 Fiebig, M., Lottermoser, T., Kneip, M. K., and Bayer, M., Correlations between magnetic and electrical orderings in multiferroic manganites (invited). *J. Appl. Phys.* **99**, 08E302 (2006).

**Acknowledgements** We thank V. Kiryukhin for helpful discussion. The work at Rutgers is supported by NSF grant DMR-0844807 and DMR-1104484.

**Author Contributions** WW and SWC conceived and designed the experiment. SWC and NL grew and annealed  $\text{ErMnO}_3$  crystals. YJC characterized the magnetic properties. YG carried out PFM and MFM measurements and analyzed the data. WW and SWC wrote the manuscript. YG wrote the supplementary information. All authors contributed to planning and discussions.

**Author information** Reprints and permission information is available at [www.nature.com/reprints](http://www.nature.com/reprints). The authors declare no competing financial interest. Readers are welcome to comment on the online version of this article at [www.nature.com/nature](http://www.nature.com/nature). Correspondence and requests for materials should be addressed to W.W. ([wdwu@physics.rutgers.edu](mailto:wdwu@physics.rutgers.edu)).

## Figure Legends

**Figure 1 | Coupled FE and antiferromagnetic domain walls with alternating magnetic moments around multiferroic vortex cores.** a, Room temperature out-of-plane PFM image (33



$\times 36 \mu\text{m}^2$ ) taken on (001) surface of an  $\text{ErMnO}_3$  single crystal. Red and blue colors correspond to up and down ferroelectric domains, respectively. **b**, MFM image ( $18 \times 18 \mu\text{m}^2$ ) taken at 5.5 K with 0.2 T out of plane magnetic field at the same location as the black box in PFM image. The color scale ( $\Delta f$ ) is 0.4 Hz. **c**, zoom-in PFM image (upper panel) and MFM image (lower panel) with lower lift height (see method) at the green boxes in **a** and **b**. The arrows represent the orientation of uncompensated magnetic moments in the antiferromagnetic DWs. The color scale ( $\Delta f$ ) is 0.8 Hz.

**Figure 2 | The temperature dependence of the antiferromagnetic DW contrast.** **a**, PFM image at the same location as MFM images,  $\text{DW}_I$  ( $\text{DW}_{II}$ ) are labeled by 'I' ('II'). **b-f**, selected MFM images at various temperatures (warming) with 0.2 T magnetic field. (See supplementary fig. S3 for the complete data set) The color scales are noted at the left bottom of each image. **g**, Temperature dependence of the DW contrast ( $\Delta f_{II} - \Delta f_I$ ) of two DWs noted by green arrows in **a**. The red curve is a fitting curve based on a doublet model. The inset shows the derivative of DC susceptibility respect to temperature,  $dy/dT$ . The blue arrow indicates the anomaly at  $T_N$ .

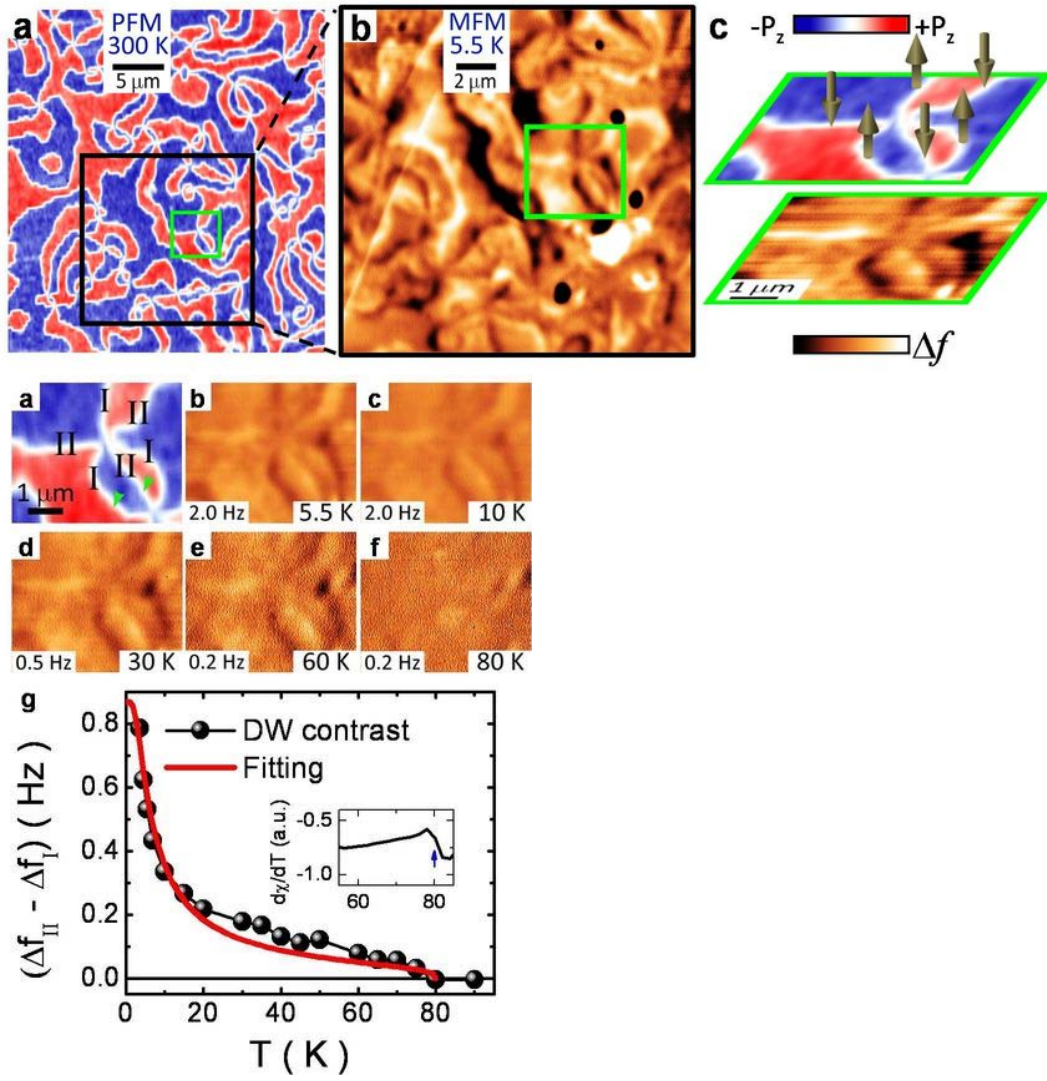
**Figure 3 | uncompensated RE moments at DW's in  $B_2$  phase.** **a**,  $\text{Mn}^{3+}$  spins configuration of  $B_2$  magnetic symmetry. Solid (dotted) green triangles represent  $\text{Mn}^{3+}$  trimers at  $z = c/2$  ( $z = 0$ ) layer.  $\text{Mn}^{3+}$  ions and spins are not shown in the rest cartoons for clarity. **b** and **c**, local distortion of type I and type II DWs in  $\text{ErMnO}_3$ , respectively. Yellow (white) circle corresponds to  $\text{Er}^{3+}$  ion distorting out of (into) paper. '+' ('-') denotes the induced  $\text{Er}^{3+}$  moment is out of (into) paper. **d**, Cartoon of spin configuration of  $\text{Er}^{3+}$  atomic planes in **b** and **c** near  $\text{DW}_I$  and  $\text{DW}_{II}$ , the arrows inside the red boxes represent uncompensated moments along the DWs.

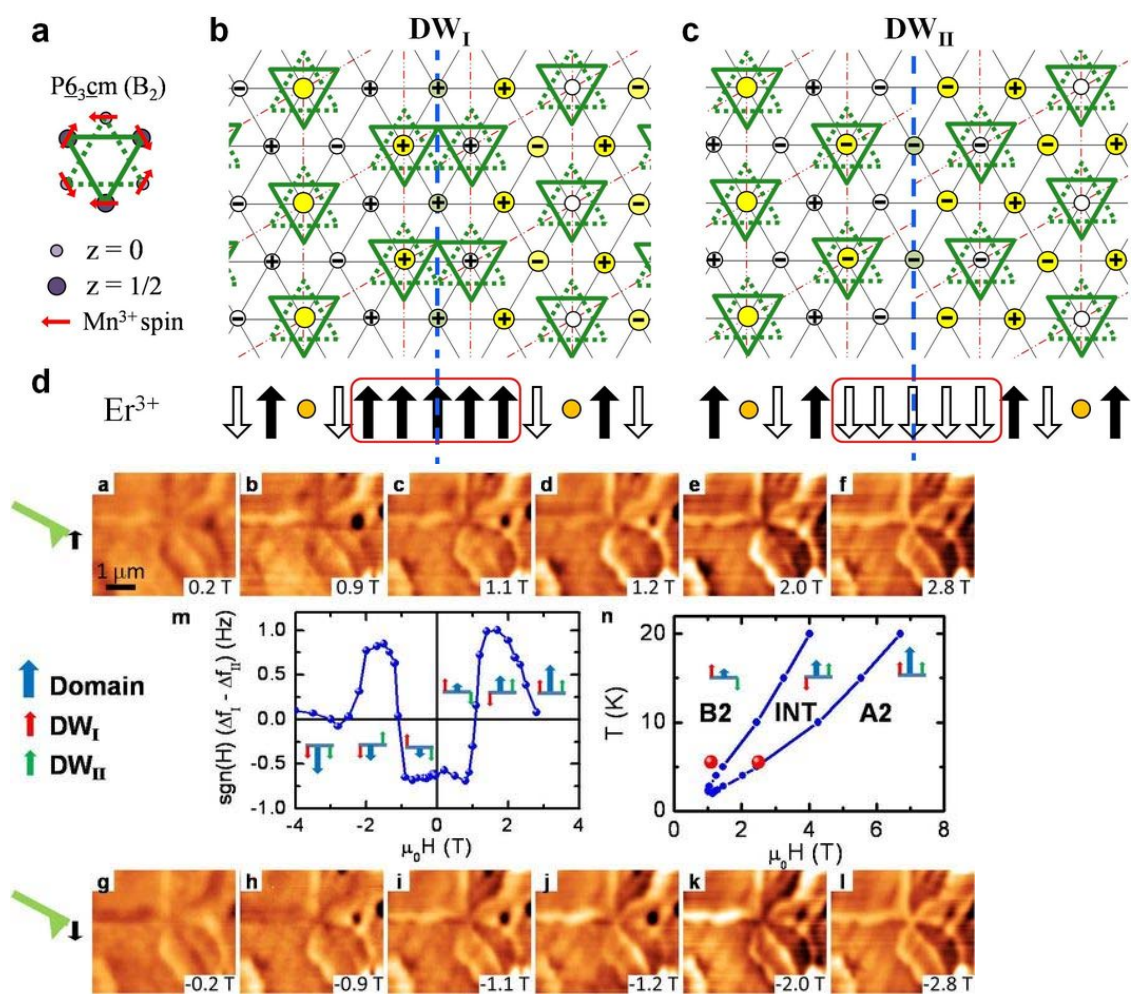
**Figure 4 | "Virgin" curves of the MFM images at 5.5 K and phase diagram.** **a-f** (**g-l**), MFM images with various positive (negative) magnetic fields after 0.2 T field cooling from 100 K to 5.5 K. Color scale: 2 Hz. **m**, Magnetic field dependence of domain wall contrast [ $\text{sgn}(H) \cdot (\Delta f_I - \Delta f_{II})$ ], the contrast difference between  $\text{DW}_I$  and  $\text{DW}_{II}$ .  $\text{sgn}(H)$  accounts for the reversal of tip moment at negative fields, as shown in the cartoons next to **a** and **g**. In the cartoon, the dark blue, red, green arrows represent the domain,  $\text{DW}_I$ ,  $\text{DW}_{II}$  moments, respectively. **n**, Magnetic phase diagram constructed from antiferromagnetic DW contrast (red spheres) and SQUID magnetization steps (blue curve).



### Method summary

Plate-like  $\text{ErMnO}_3$  single crystals with flat surfaces perpendicular to the  $c$  axis were grown using a conventional flux method with  $\text{Bi}_2\text{O}_3$  flux. A mixture of 80 mol % of  $\text{Bi}_2\text{O}_3$  and 20 mol % of  $\text{ErMnO}_3$  powders was heated up to 1260 °C in a platinum crucible, and cooled slowly with 2.5 °C/h rate. Two pieces from the same batch were heated again up to 1200 °C, and slowly cooled to 1130 °C with 15 °C/h. One piece is used in SQUID measurement, the other is used in PFM and MFM experiments. The specimen was glued to a sapphire substrate by Ag epoxy. Ambient PFM images were taken on bare (001) surface with a Multimode antiferromagnetic in conjunction with homemade circuits. 50 nm gold film was deposited onto sample surface by sputtering before MFM experiment to eliminate the electro-static interaction. MFM images were taken with a home-made VT-MFM, which is interfaced with a Nanoscope IIIa controller. MFM signal was taken in a frequency-modulated Linear mode, in which topography and MFM scan lines are interleaved. The lift height is 50 nm for all the MFM images except Fig. 1b (was 180 nm to avoid large topography features). During MFM experiment, the sample space was kept in cryogenic vacuum for high sensitivity. The alignment between PFM and MFM images is achieved by correlating topographic features.





## Appendix V.

### Magnetochromism in hematite: chameleonic rust

P. Chen,<sup>1</sup> N. Lee,<sup>2</sup> S. McGill,<sup>3</sup> S. -W. Cheong,<sup>2</sup> and J. L. Musfeldt<sup>1</sup>

<sup>1</sup>*Department of Chemistry, University of Tennessee, Knoxville, Tennessee 37996, USA*

<sup>2</sup>*Rutgers Center for Emergent Materials and Department of Physics & Astronomy,  
Rutgers University, Piscataway, New Jersey 08854, USA*

<sup>3</sup>*National High Magnetic Field Laboratory, Tallahassee, Florida 32310, USA*

(Dated: September 20, 2011)

Magnetoelectric coupling in materials like multiferroics, dilute magnetic semiconductors, and topological insulators has attracted a great deal of attention, although most work has been done in the static limit. Magneto-optical spectroscopy offers a way to investigate the dynamics of charge-spin coupling, an area where there has been much less effort. Using these techniques, we discovered that applied magnetic field changes the color of  $\alpha\text{-Fe}_2\text{O}_3$ , one of the world's oldest and most ubiquitous materials, with the system becoming more red in high fields. Of course, spin-orbit coupling naturally mixes charge and spin excitations, but the effect is amplified in hematite by the presence of the spin flop transition, which reorients magnetic order. The oscillator strength lost in the color band is partially transferred to the magnon side band, a process that also reveals a new exciton pattern induced by the modified exchange coupling. Analysis of the exciton pattern exposes  $C2/c$  monoclinic symmetry in the high field phase. These findings advance our understanding of the collective interplay between charge and magnetism, identify a field-tunable material for next-generation magneto-optical devices, and motivate fundamental research on other iron-based materials under extreme conditions and away from the static limit.

The interplay between charge, structure, and magnetism is at the heart of the rich tunability in transition metal oxides<sup>1-3</sup>. Color properties in particular reveal crystal field environments and electronic transition around and between metal centers<sup>4,5</sup>. At the same time, the optical properties of a material often display collective excitations like excitons and magnon sidebands. They are induced by exchange coupling and therefore very sensitive to variations in magnetic order<sup>6-8</sup>. When combined with external stimuli like temperature or magnetic field, optical spectroscopy can reveal transition mechanisms, local symmetry breaking, and microscopic insight into fundamental mixing processes<sup>9-11</sup>.  $\alpha$ -Fe<sub>2</sub>O<sub>3</sub> attracted our attention as a model antiferromagnet with large exchange couplings that result in well-separated excitations and experimentally-realizable critical fields for magnetic structure modification<sup>12-14</sup>. Hematite means “blood” in Greek and refers to the red color of the powdered mineral<sup>15</sup>. It is responsible for the captivating reddish landscape of the Grand Canyon, has been used for thousands of years in amulets and pigments and as the main source of elemental iron, and plays a central role in corrosion problems (as the main component of rust). At ambient conditions,  $\alpha$ -Fe<sub>2</sub>O<sub>3</sub> crystallizes in the rhombohedral corundum structure ( $R\bar{3}c$ )<sup>16</sup>. The system is antiferromagnetic below the Morin transition ( $T_M \sim 260$  K)<sup>17</sup>, with spins lying along the [111] axis of the trigonal unit cell (inset, Fig. 1a). Both temperature ( $T_M$ ) and magnetic field ( $B_{C\parallel} = 6.8$  T,  $B_{C\perp} = 16.0$  T)<sup>13,14</sup> drive a spin flop to the basal plane<sup>18</sup>, and in the high temperature/field phase,  $\alpha$ -Fe<sub>2</sub>O<sub>3</sub> is a weak ferromagnet<sup>19,20</sup>. Previous spectroscopic work revealed the electronic structure and identified the exciton and associated magnon sideband on the leading edge of the  ${}^6A_{1g} \rightarrow {}^4T_{1g}$  on-site excitation, although no fine structure was resolved<sup>21,22</sup>.

The successful preparation of high quality single crystals combined with access to high-resolution magneto-optical facilities motivated us to revisit the optical properties of this ancient material. We find that applied magnetic field drives a color change in  $\alpha$ -Fe<sub>2</sub>O<sub>3</sub> such that it appears more red in the high field phase. This chameleonic effect demonstrates that the Fe<sup>3+</sup> on-site excitations are intrinsically coupled to magnetic ordering. Of course, spin-orbit coupling naturally mixes charge and spin excitations<sup>23</sup>, but the effect is amplified by the presence of the spin flop transition. Analysis of the exciton behavior on the leading edge of the color band reveals  $C2/c$  monoclinic symmetry in the high field phase and more generally illustrates how exciton patterns can be used to elucidate magnetic symmetry. The discovery of magnetochromism in this model system extends our understanding of magneto-

electric in more complex iron oxides<sup>9,24–26</sup> where functionality derives from the entanglement of spin and charge channels.

Figure 1a displays the optical response of  $\alpha$ -Fe<sub>2</sub>O<sub>3</sub>. We assign the two strong, broad bands centered at  $\sim 11550$  and  $15300 \text{ cm}^{-1}$  as  ${}^6A_{1g} \rightarrow {}^4T_{1g}$  and  ${}^6A_{1g} \rightarrow {}^4T_{2g}$  on-site excitations<sup>21,22</sup>. These  $d-d$  excitations are formally forbidden although they appear in many oxides due to spin-orbit coupling, exchange interaction, and odd parity phonons that hybridize states and break inversion symmetry<sup>10,21,27</sup>. Low temperature reveals a great deal of fine structure on the leading edge of the  ${}^6A_{1g} \rightarrow {}^4T_{1g}$  band (Fig 1b). These strongly polarized features are collective excitations. Their properties are summarized in Table I. For the purposes of our discussion, the fundamental magnetic- and electronic-dipole excitations, M1 and E1, are most important. Interactions between four translationally inequivalent Fe<sup>3+</sup> sites in the magnetic structure give rise to Davydov splitting between the (M1 $\sigma$ , E1 $\pi$ ) and (M2 $\sigma$ , E2 $\pi$ ) exciton pairs<sup>28</sup>. These splittings are  $38.6$  and  $14.0 \text{ cm}^{-1}$ , respectively, an order of magnitude larger than in YCrO<sub>3</sub> ( $2 \text{ cm}^{-1}$ )<sup>29</sup> and Cr<sub>2</sub>O<sub>3</sub> ( $3.5 \text{ cm}^{-1}$ )<sup>30</sup>. This is a consequence of the larger inter-sublattice coupling energy in  $\alpha$ -Fe<sub>2</sub>O<sub>3</sub>. The feature labeled MS1 is assigned as the magnon sideband<sup>22</sup>. Based on the position, shape, and polarization behavior, we associate it with the M1 $\sigma$  exciton<sup>31</sup>. The intensity is stronger than that of M1 $\sigma$  because this electric dipole-allowed excitation involves pairs of ions and thus breaks the parity selection rule<sup>10,32</sup>. The magnon sideband frequency can be expressed as  $\omega = \omega_e + \omega_m$ <sup>33</sup>, where  $\omega_e$  is the exciton frequency, and  $\omega_m$  is the magnon frequency. We find  $\omega_m = 743.7 \pm 0.1 \text{ cm}^{-1}$  in excellent agreement with the magnon energy obtained by neutron scattering<sup>12</sup>. Other collective excitations including phonon sidebands and the two magnon sideband are also observed<sup>34</sup>.

We analyzed the magnon sideband selection rules<sup>35</sup> at different points in the Brillouin zone (Fig. 1c,d) and calculated the density of states using the magnon dispersion of Samuelsen<sup>28,36</sup>. The results are in good agreement with the measured absorption spectrum (Fig. 1e) and explain the directionally-dependent magnon sideband shape<sup>28</sup>. The exciton and magnon features display characteristic temperature dependence. As shown in Fig. 1f, expressing the magnon sideband frequency as  $\frac{\omega_m(T)}{\omega_m(0)}$  reveals high temperature softening, whereas the reduced frequency of the E1 $\pi$  exciton is relatively constant. The former compares well with a numerical calculation of the normalized sublattice magnetization ( $\frac{M(T)}{M(0)}$ ) using random phase approximation<sup>28</sup>. The discrepancy in the high temperature range is

because magnetization measures the thermal average population of magnons and is less sensitive to the zone boundary (A point) dispersion<sup>33,37</sup>. Similar effects are observed in  $\text{MnF}_2$ <sup>33</sup> and  $\text{Cr}_2\text{O}_3$ <sup>11</sup>.

Figure 2a,b,c displays the field-induced absorption difference spectra of  $\alpha\text{-Fe}_2\text{O}_3$  for different crystal orientations and magnetic field directions. The magnetochromic response reveals that the on-site excitations are intrinsically coupled to the microscopic spin structure. We can quantify the field-induced color change with the partial sum rule (inset, Fig. 2a,b,c)<sup>38</sup>. Oscillator strength changes ( $\Delta f$ ) show a first order transition at  $B_{C\parallel} = 6.6 \pm 0.2$  T when  $B \parallel [111]$ , and a broad transition at  $B_{C\perp} = 16.2 \pm 0.2$  T when  $B \perp [111]$ . These critical fields are easily assigned as field-induced spin flop transitions in agreement with magnetization<sup>13</sup> and ultrasonic attenuation measurements<sup>14,39</sup>. Importantly, the  $d-d$  on site excitations are in the visible range and responsible for the reddish color of  $\alpha\text{-Fe}_2\text{O}_3$ . As shown in the absorption difference plot, this system absorbs fewer photons in the red color range in high magnetic field (on the order of 2% less).  $\alpha\text{-Fe}_2\text{O}_3$  thus appears more red in the magnetically reoriented phase<sup>40</sup>. This color change is observed because the coherent spin transition amplifies the charge-spin interaction beyond what one might expect from traditional spin-orbit processes alone. The field-induced reduction of oscillator strength of the  ${}^6A_{1g} \rightarrow {}^4T_{1g}$  band is partially recovered in the magnon sideband (insets, Fig. 2a,b,c). Optical property changes driven by magnetic order reorientation have been observed in other functional materials including  $\text{FeCO}_3$  (color contrast at the 13 T spin-flop transition)<sup>7</sup> and  $\text{BiFeO}_3$  (color change at 20 T due to spin spiral quenching)<sup>9</sup>. Here, we report the discovery of such an effect in one of the world's oldest antiferromagnetic materials.

Magnon sideband formation is controlled by exchange coupled pairs<sup>32,41</sup>, and as a consequence, field-induced magnetic order reorientation will significantly impact the behavior. Strikingly, the magnon sideband displays a 27% increase in oscillator strength at 35 T compared to its zero field value (insets, Fig. 2a,b,c). Magnon sideband intensity is dependent upon (i) exciton + magnon joint density of states and (ii) collinearity of the magnetic structure<sup>8</sup>. It will decrease dramatically if spin collinearity is violated as in  $\text{RbMnF}_3$ <sup>8</sup> and  $\text{FeCO}_3$ <sup>7</sup>. Based on the observed intensity increase, we conclude that spin collinearity is conserved through the spin-flop in  $\alpha\text{-Fe}_2\text{O}_3$ . Figure 2d,g,i shows a close-up view of the magnon sideband excitation at selected magnetic fields. The field-induced frequency shifts are summarized in Fig. 2j,k,l, and like the oscillator strength, place the critical fields for spin-flop



at  $B_{C\parallel} = 6.6 \pm 0.2$  T and  $B_{C\perp} = 16.2 \pm 0.2$  T. Importantly, the magnon sideband softens by  $\sim 6$  cm $^{-1}$  through the 6.6 T transition. Assuming that the magnon dispersion does not change substantially<sup>36</sup>, we can estimate changes in the exchange constants ( $\frac{\Delta J}{J}$ ) using the least square method and a fit of the magnon density of states to the 35 T  $\sigma$ -polarized spectrum. The results show that ferromagnetic couplings J1 and J2 increase by  $\sim 15\%$  and  $8\%$  respectively, whereas antiferromagnetic couplings |J3| and |J4| decrease by about 1%. These results indicate larger direct exchange<sup>12</sup> and smaller superexchange in the high field phase.

Exciton behavior provides an incisive probe of Zeeman-splitting in  $\alpha$ -Fe $_2$ O $_3$ . As shown in Fig. 2j, the E1 $\alpha$  and E2 $\alpha$  excitons split into two components, each with total  $g$  values of  $3.77 \pm 0.1$ . This splitting is due to the removal of up- and down-spin sublattice degeneracies in the field<sup>42</sup>. The two sublattice model<sup>6</sup> allows us to evaluate  $g'$  of the excited state. We find  $g' = 2.08 \pm 0.03$  assuming a ground state single sublattice  $g$  of 2 for E1 and E2. Using this  $g'$ , we can back calculate<sup>6</sup> a magnon sideband  $g$  of 0.22, a value that is consistent with the lack of observed splitting in this feature up to  $B_{C\parallel}$ . These  $g$  values are typical for antiferromagnets<sup>6</sup>, demonstrating that spin-orbit coupling in the excited  ${}^4T_{1g}$  states is similar to that in MnF $_2$ , even though the exchange interaction is much larger.

Exciton behavior can also be used to reveal magnetic symmetry in the high field phase of  $\alpha$ -Fe $_2$ O $_3$ . At  $B_{C\parallel}$ , the Zeeman splitting disappears, and a new pattern emerges (Fig. 2j). This more complicated exciton pattern arises from the transition to a different magnetic ordering. Above  $B_{C\parallel}$ , lower symmetry lifts the degeneracy of the E1 $\alpha$  excitation and gives rise to a new peak at  $\sim 9748$  cm $^{-1}$ <sup>43</sup>. Two magnetic-dipole excitons, M1 $\sigma$  and M2 $\sigma$ , are also activated due to the new coordinate system (and selection rules) above 6.2 T. M1 $\sigma$  hardens by  $4.6$  cm $^{-1}$ , whereas M2 $\sigma$  softens by  $0.5$  cm $^{-1}$ . To explore the new symmetry of the high field phase, we make use of the observed exciton pattern and invoke two additional constraints: (i) the new magnetic order symmetry should be a subgroup of the original  $R\bar{3}c$  structure and (ii) spin collinearity is conserved above  $B_{C\parallel}$ . Several symmetry candidates emerge from this analysis<sup>44</sup>. They include  $P1$ ,  $P\bar{1}$ ,  $C2$ ,  $Cc$ ,  $C2/c$ ,  $R3$ ,  $R\bar{3}$ ,  $R32$ , and  $R3c$ . Only the  $C2/c$  monoclinic structure contains the necessary inversion center and  $C2$  rotational axis to meet the aforementioned criteria<sup>28</sup>. Both operations survive in the high field phase due to conservation of spin collinearity. This is in agreement with previous work of Tanabe *et al.*<sup>45</sup> that pointed toward a monoclinic structure, although they did not specify a specific symmetry group. Figure 3 summarizes these effects, schematically illustrating the entangle-



ment of electronic structure and magnetic order in  $\alpha\text{-Fe}_2\text{O}_3$  as revealed by magneto-optical spectroscopy.

Switching the applied field to the (111) plane, excitons display Zeeman-like splitting above 13 T (Fig. 2k,l). The peculiar appearance is due to removal of degeneracy of the spin component parallel to the field. The exciton pattern in the new magnetic order is consistent with the aforementioned group theory predictions for  $C2/c$  magnetic symmetry<sup>28</sup>, demonstrating that magnetic fields in different directions drive to identical high field phases in  $\alpha\text{-Fe}_2\text{O}_3$ . Finally, above  $B_{C\perp}$ , Davydov splitting of  $(M1\sigma, E1\pi)$  and  $(M2\sigma, E2\pi)$  decreases by  $\sim 8$  and  $2\text{ cm}^{-1}$ , respectively. This indicates that the inter-sublattice coupling energy is reduced compared to that in zero field.

Summarizing, we report the discovery of magnetochromism in one of the world's oldest and most ubiquitous antiferromagnetic materials,  $\alpha\text{-Fe}_2\text{O}_3$ . In addition to a field-induced color change due to the reorientation of magnetic order, the exciton pattern reveals  $C2/c$  monoclinic symmetry in the high field phase. This work advances our understanding of the interplay between charge and magnetism, identifies a strategy for the development of next-generation color change materials, and motivates fundamental research on other iron-based materials under extreme conditions and away from the static limit.

## Methods

High quality  $\alpha\text{-Fe}_2\text{O}_3$  single crystals were grown using the flux method. Most work on hematite has been carried out on samples of mineralogical origin, so the preparation of large crystals with high purity provides an important opportunity. X-ray shows no impurity phases and a single oxidation state. We employed five independent crystals of varying thicknesses and either (111) or  $(\bar{1}10)$  orientation for our optical properties work<sup>50</sup>. This combination allowed us to obtain complete results over the full frequency range of interest and optimal sensitivity to the small features on the leading edge of the  ${}^6A_{1g} \rightarrow {}^4T_{1g}$  on-site excitation. Spectra were collected using a Bruker Equinox 55 Fourier transform infrared spectrometer equipped with a microscope attachment ( $600\text{--}17000\text{ cm}^{-1}$ ;  $1\text{ cm}^{-1}$  resolution). Temperature control was achieved with an open-flow cryostat. Magneto-optical measurements were carried out at the NHMFL using the 35 T resistive magnet system ( $B \parallel [111]$ ,  $B \perp [111]$ ). We calculated the absorption coefficient  $\alpha(\omega)$  using a Glover-Tinkham analysis<sup>51,52</sup>. Traditional

peak fitting methods were employed as appropriate. Symmetry analysis was performed by group theory, and the shape of the magnon sideband was calculated numerically<sup>28</sup>.

- 
- <sup>1</sup> Imada, M., Fujimori, A. & Tokura, Y. Metal-insulator transitions. *Rev. Mod. Phys.* **70**, 1039-1263 (1998).
  - <sup>2</sup> Kivelson, S. A., Fradkin, E. & Emery, V. J. Electronic liquid-crystal phases of a doped Mott insulator. *Nature* **393**, 550-553 (1998).
  - <sup>3</sup> Cheong, S.-W. & Mostovoy, M. Multiferroics: a magnetic twist for ferroelectricity. *Nat. Mater.* **6**, 13-20 (2007).
  - <sup>4</sup> Kahn, F. J., Pershan, P. S. & Remeika, J. P. Ultraviolet magneto-optical properties of single-crystal orthoferrites, garnets, and other ferric oxide compounds. *Phys. Rev.* **186**, 891-918 (1969).
  - <sup>5</sup> Arima, T., Tokura, Y. & Torrance, J. B. Variation of optical gaps in perovskite-type 3d transition-metal oxides. *Phys. Rev. B* **48**, 17006-17009 (1993).
  - <sup>6</sup> Russell, P. G., McClure, D. S. & Stout, J. W. Zeeman splitting of narrow lines in crystalline MnF<sub>2</sub>, FeF<sub>2</sub>, and CoF<sub>2</sub>. Evidence for spin-wave excitations. *Phys. Rev. Lett.* **16**, 176-178 (1966).
  - <sup>7</sup> Eremenko, V. V., Litvinenko, Yu. G. & Myatlik, V. I. Attenuation of light absorption in antiferromagnetic FeCO<sub>3</sub> by a magnetic field. *JETP Lett.* **12**, 47-49 (1970).
  - <sup>8</sup> Eremenko, V. V. & Petrov, E. G. Light absorption in antiferromagnets. *Adv. Phys.* **26**, 31-78 (1977).
  - <sup>9</sup> Xu, X. S. *et al.* Optical properties and magnetochromism in multiferroic BiFeO<sub>3</sub>. *Phys. Rev. B* **79**, 134425 (2009).
  - <sup>10</sup> Sell, D. D., Greene, R. L. & White, R. M. Optical exciton-magnon absorption in MnF<sub>2</sub>. *Phys. Rev.* **158**, 489-510 (1967).
  - <sup>11</sup> Allen, J. W., Macfarlane, R. M. & White, R. L. Magnetic davydov splittings in the optical absorption spectrum of Cr<sub>2</sub>O<sub>3</sub>. *Phys. Rev.* **179**, 523-541 (1969).
  - <sup>12</sup> Samuelsen, E. J. & Shirane, G. Inelastic neutron scattering investigation of spin waves and magnetic interactions in  $\alpha$ -Fe<sub>2</sub>O<sub>3</sub>. *Phys. Status Solidi* **42**, 241-256 (1970).
  - <sup>13</sup> Foner, S. & Shapira, Y. Magnetic phase transitions in pure  $\alpha$ -Fe<sub>2</sub>O<sub>3</sub>. *Phys. Lett.* **29A**, 276-277 (1969).
  - <sup>14</sup> Shapira, Y. Ultrasonic behavior near the spin-flop transitions of hematite. *Phys. Rev.* **184**,

- 589-600 (1969).
- <sup>15</sup> Morrish, A. H. *Canted antiferromagnetism: hematite* (World Scientific Publishing Company, 1994).
  - <sup>16</sup> Pauling, L. & Hendricks, S. B. The crystal structures of hematite and corundum. *J. Am. Chem. Soc.* **47**, 781-790 (1925).
  - <sup>17</sup> Morin, F. J. Magnetic susceptibility of  $\alpha\text{Fe}_2\text{O}_3$  and  $\alpha\text{Fe}_2\text{O}_3$  with added titanium. *Phys. Rev.* **78**, 819-820 (1950).
  - <sup>18</sup> Shull, C. G., Strauser, W. A. & Wollan, E. O. Neutron diffraction by paramagnetic and antiferromagnetic substances. *Phys. Rev.* **83**, 333-345 (1951).
  - <sup>19</sup> Dzyaloshinsky, I. A thermodynamic theory of "weak" ferromagnetism of antiferromagnetics. *J. Phys. Chem. Solids* **4**, 241-255 (1958).
  - <sup>20</sup> Moriya, T. Anisotropic superexchange interaction and weak ferromagnetism. *Phys. Rev.* **120**, 91-98 (1960).
  - <sup>21</sup> Marusak, L. A., Messier, R. & White, W. B. Optical absorption spectrum of hematite,  $\alpha\text{-Fe}_2\text{O}_3$  near IR to UV. *J. Phys. and Chem. Solids* **41**, 981-984 (1980).
  - <sup>22</sup> Galuza, A. I., Beznosov, A. B. & Eremenko, V. V. Optical absorption edge in  $\alpha\text{-Fe}_2\text{O}_3$ : The exciton-magnon structure. *Low Temp. Phys.* **24**, 726-729 (1998).
  - <sup>23</sup> We do not expect large coupling in  $\text{Fe}^{3+}$ . The color change in  $\alpha\text{-Fe}_2\text{O}_3$  is observed because of the collective transition.
  - <sup>24</sup> Xu, X. S. *et al.* Charge order, dynamics, and magnetostructural transition in multiferroic  $\text{LuFe}_2\text{O}_4$ . *Phys. Rev. Lett.* **101**, 227602 (2008).
  - <sup>25</sup> Fontijn, W. F. J., van der Zaag, P. J., Feiner, L. F., Metselaar, R. & Devillers, M. A. C. A consistent interpretation of the magneto-optical spectra of spinel type ferrites (invited). *J. Appl. Phys.* **85**, 5100-5105 (1999).
  - <sup>26</sup> Gasparov, L. V. *et al.* Infrared and Raman studies of the Verwey transition in magnetite. *Phys. Rev. B* **62**, 7939-7944 (2000).
  - <sup>27</sup> Lohr, L. L. Spin-forbidden electronic excitations in transition metal complexes. *Coord. Chem. Rev.* **8**, 241-259 (1972).
  - <sup>28</sup> Materials and methods are available as supporting information online.
  - <sup>29</sup> Aoyagi, K., Tsushima, K. & Sugano, S. Direct observation of Davydov splitting in antiferromagnetic  $\text{YCrO}_3$ . *Solid State Commun.* **7**, 229-232 (1969).

- <sup>30</sup> van der Ziel, J. P. Davydov splitting of the  $^2E$  lines in antiferromagnetic  $\text{Cr}_2\text{O}_3$ . *Phys. Rev. Lett.* **18**, 237-239 (1967).
- <sup>31</sup> The intensity of  $\text{MS1}$  increases as that of  $\text{M1}\sigma$  when rotating polarizer from  $\pi$  to  $\sigma$  direction.
- <sup>32</sup> Halley, J. W. & Silvera, I. Odd-exciton magnon interaction and explanation of anomalous far-infrared absorption in antiferromagnetic  $\text{FeF}_2$ . *Phys. Rev. Lett.* **15**, 654-656 (1965).
- <sup>33</sup> Greene, R. L., Sell, D. D., Yen, W. M. & Schawlow, A. L. Observation of a spin-wave sideband in the optical spectrum of  $\text{MnF}_2$ . *Phys. Rev. Lett.* **15**, 656-659 (1965).
- <sup>34</sup> Based on the frequency shift and polarized results, the features centered at 9930, 10104 and 10289  $\text{cm}^{-1}$  have irregular shape and are possibly due to the coupling of  $E1$  with phonons<sup>53</sup>. The excitation at 10645  $\text{cm}^{-1}$ , 10787 and 10990  $\text{cm}^{-1}$  are the phonon sideband of  $\text{MS1}$  while the feature at 11100  $\text{cm}^{-1}$  is probably two magnons coupled with  $\text{M1}\sigma$ .
- <sup>35</sup> Lax, M. & Hopfield, J. J. Selection rules connecting different points in the Brillouin zone. *Phys. Rev.* **124**, 115-123 (1961).
- <sup>36</sup> Samuelsen, E. J. Spin waves in antiferromagnets with corundum structure. *Physica* **43**, 353-374 (1969).
- <sup>37</sup> Ashcroft, N. W. & Mermin, N. D. *Solid State Physics* (Brooks Cole, 1976).
- <sup>38</sup> Wooten, F. *Optical properties of solids* (New York, Academic Press, 1972).
- <sup>39</sup> The magnitude of critical field is determined by the direction of applied magnetic field and not sensitive to the light polarization direction. This is the evidence that applied magnetic field induces the spin-flop.
- <sup>40</sup> A reduction of oscillator strength is also observed at Morin transition<sup>21</sup>.
- <sup>41</sup> Tanabe, Y., Moriya, T., Sugano, S. Magnon-Induced Electric Dipole Transition Moment. *Phys. Rev. Lett.* **15**, 1023-1025 (1965).
- <sup>42</sup> Stager, C. V. Zeeman Effect of the R Lines in  $\text{Cr}_2\text{O}_3$ . *J. Appl. Phys.* **34**, 1232-1233 (1963).
- <sup>43</sup> An additional peak should split from  $E2\alpha$  but is not observed, probably because it is superimposed with  $E1\alpha$ .
- <sup>44</sup> Hermann, C. Tensors and crystal symmetry. *Z. Kristallogr.* **89**, 32-48 (1934).
- <sup>45</sup> Tanabe, Y. *et al.* Direct optical excitation of two and three magnons in  $\alpha\text{-Fe}_2\text{O}_3$ . *Low Temp. Phys.* **31**, 780-785 (2005).
- <sup>46</sup> We did this assignment by the similar intensity of excitons in  $\alpha$  and  $\sigma$  polarizations and magnetic field results.

- <sup>47</sup> Finger, L. W. & Hazen, R. M. Crystal structure and isothermal compression of  $\text{Fe}_2\text{O}_3$ ,  $\text{Cr}_2\text{O}_3$ , and  $\text{V}_2\text{O}_3$  to 50 kbars. *J. Appl. Phys.* **51**, 5362-5367 (1980).
- <sup>48</sup> Phillips, J. C. Critical points and lattice vibration spectra. *Phys. Rev.* **104**, 1263-1277 (1956).
- <sup>49</sup> Mills, R. E., Kenan, R. P. & Milford, F. J. Green's-function theory of ferrimagnetism, with an application to magnetite. *Phys. Rev.* **145**, 704-717 (1966).
- <sup>50</sup> We employed five thin, plate-like crystals of  $\alpha\text{-Fe}_2\text{O}_3$  for this work. In the (111) orientation, the available thicknesses were 18, 51 and 110  $\mu\text{m}$ . In the  $(\bar{1}10)$  orientation, the available thicknesses were 42 and 85  $\mu\text{m}$ . Exciton and magnon investigations were best carried out with thicknesses  $> 80 \mu\text{m}$ , whereas on-site excitations were followed with thicknesses  $< 50 \mu\text{m}$ .
- <sup>51</sup> Chen, P. *et al.* Optical properties of quasi-tetragonal  $\text{BiFeO}_3$  thin films. *Appl. Phys. Lett.* **96**, 131907 (2010).
- <sup>52</sup> Tinkham, M. *in Far Infrared Properties of Solids* (Plenum, New York, 1970).
- <sup>53</sup> Blanchard, M., Lazzeri, M., Mauri, F. & Balan, E. First-principles calculation of the infrared spectrum of hematite. *American Mineralogist* **93**, 1019-1027 (2008).

### Acknowledgements

This work was supported by the Materials Science Division, Basic Energy Sciences, U. S. Department of Energy (Contract Nos. DE-FG02-01ER45885 at UT (JLM) and DE-FG02-07ER46382 at Rutgers University (SWC)) and the National Science Foundation (DMR-0654118 at the NHMFL (SMG)).

### Author contributions

J.L.M. and P.C. conceived and designed the experiments. P.C. performed the experiments with assistance from J.L.M. and S.M.G. S.-W.C. and N.L. carried out the crystal growth and related analysis. P.C. and J.L.M. analyzed the data and wrote the paper. S.M.G., N.L., and S.-W.C. contributed to the manuscript.

### Competing and Financial Interests

The authors declare that they have no competing financial interests.

### Figure Legends

**Fig. 1.** **a**, (Color online) Absorption coefficient,  $\alpha(\omega)$ , of  $\alpha$ -Fe<sub>2</sub>O<sub>3</sub> in the range of on-site Fe<sup>3+</sup>  $d$ - $d$  excitations at 300 and 4.2 K. Inset: rhombohedral lattice<sup>47</sup> and low temperature four sublattice spin structure.<sup>18</sup> **b**, Close up view of the fine structure on the leading edge of the  ${}^6A_{1g} \rightarrow {}^4T_{1g}$  on-site excitation at 4.2 K in the  $\alpha$ ,  $\sigma$  and  $\pi$  polarizations. Inset: close-up view of the excitons. **c,d**, Irreducible representations of the exciton and magnon in the Brillouin zone of  $\alpha$ -Fe<sub>2</sub>O<sub>3</sub>. **e**, Comparison of the  $\sigma$ -polarized magnon sideband absorption spectrum with the calculated density of states (DOS). Inset: Calculated magnon DOS using optimized exchange constants  $J_1 = 7.6$  K,  $J_2 = 2.0$  K,  $J_3 = -27.7$  K, and  $J_4 = -22.2$  K.<sup>28</sup> The frequency channel width was taken to be the same as the spectral resolution (1 cm<sup>-1</sup>). The nature of the critical points in Brillouin zone are shown in the parenthesis.<sup>48</sup> **f**, Temperature dependence of E1 ( $\pi$ ) exciton and magnon sideband (MS1,  $\alpha$ ) peak positions, expressed as the ratio of  $\frac{\omega_e(T)}{\omega_e(0)}$  and  $\frac{\omega_m(T)}{\omega_m(0)}$ , respectively. The latter compares well with the calculated sublattice magnetization<sup>12,49</sup> using the same exchange constants listed above. Inset:  $\alpha(\omega)$  of the  $\sigma$ -polarized magnon sideband at different temperatures.

**Fig. 2.** (Color online) Absorption difference spectra [ $\alpha(B) - \alpha(B = 0 \text{ T})$ ] of  $\alpha$ -Fe<sub>2</sub>O<sub>3</sub> at 4.2 K for different crystal orientations and magnetic field directions: **a**,  $\alpha$ -polarization and  $B \parallel [111]$ , **b**,  $\sigma$ -polarization and  $B \perp [111]$ , and **c**,  $\pi$ -polarization and  $B \perp [111]$  at selected magnetic field 5, 10, 15, 35 T. The corresponding low temperature zero field absorption spectra are shown as gray solid curves for comparison. Insets: oscillator strength change in the range of the magnon sideband and  ${}^6A_{1g} \rightarrow {}^4T_{1g}$  on-site excitation as a function of magnetic field. Close-up view of the excitons (**d,e,f**) and magnon sidebands (**g,h,i**) in the  $\alpha$ -,  $\sigma$ -, and  $\pi$ -polarizations at selected magnetic fields. (**j,k,l**) Peak position vs. magnetic field for the exciton and magnon sideband features for the polarizations and field directions of interest.

**Fig. 3.** (Color online) Schematic illustration of the field-induced transition that alters the magnetic structure in  $\alpha$ -Fe<sub>2</sub>O<sub>3</sub>. The modified exchange constants impact the magnetic order, exciton pattern, and  $d$ - $d$  on-site excitation through various coupling processes.

### Tables

TABLE I: Properties of  ${}^6A_{1g} \rightarrow {}^4T_{1g}$  fine structure in  $\alpha\text{-Fe}_2\text{O}_3$  at 4.2 K. In the line notation, M represents magnetic dipole character, E is electric dipole and MS is magnon sideband. In the polarization notation,  $\alpha$  ( $\tilde{E} \perp c, \tilde{H} \perp c$ ),  $\sigma$  ( $\tilde{E} \perp c, \tilde{H} \parallel c$ ),  $\pi$  ( $\tilde{E} \parallel c, \tilde{H} \perp c$ ),  $\tilde{E}$  and  $\tilde{H}$  are the electric and magnetic vector of light,  $c$  is [111] axis of the crystal.  $f \equiv \frac{2e}{N_e \pi \omega_p^2} \int_{\omega_1}^{\omega_2} n \alpha(\omega, B) d\omega$ , here,  $N_e = 5$  is the number of electrons per Fe site,  $n$  is the refractive index,  $\omega_p$  is the plasma frequency,  $\omega_1$  and  $\omega_2$  are the frequency limits of integration.

Line	Polarization	Position ( $\text{cm}^{-1}$ )	f $10^{-10}$	Representation	
				$C_3$	R3C
M1	$\sigma$	9727.86	4.8	A	$\Gamma_2^+$
E1	$\pi$	9766.41	80	A	$\Gamma_2^{-46}$
	$\alpha, \sigma$		8.6	$C_1/C_2$	$\Gamma_3^-$
E2	$\pi$	9776.07	4.3	A	$\Gamma_2^{-46}$
	$\alpha, \sigma$		23	$C_1/C_2$	$\Gamma_3^-$
M2	$\sigma$	9790.10	2.5	A	$\Gamma_2^+$
MS1	$\alpha, \sigma, \pi$	10471.54	1400		





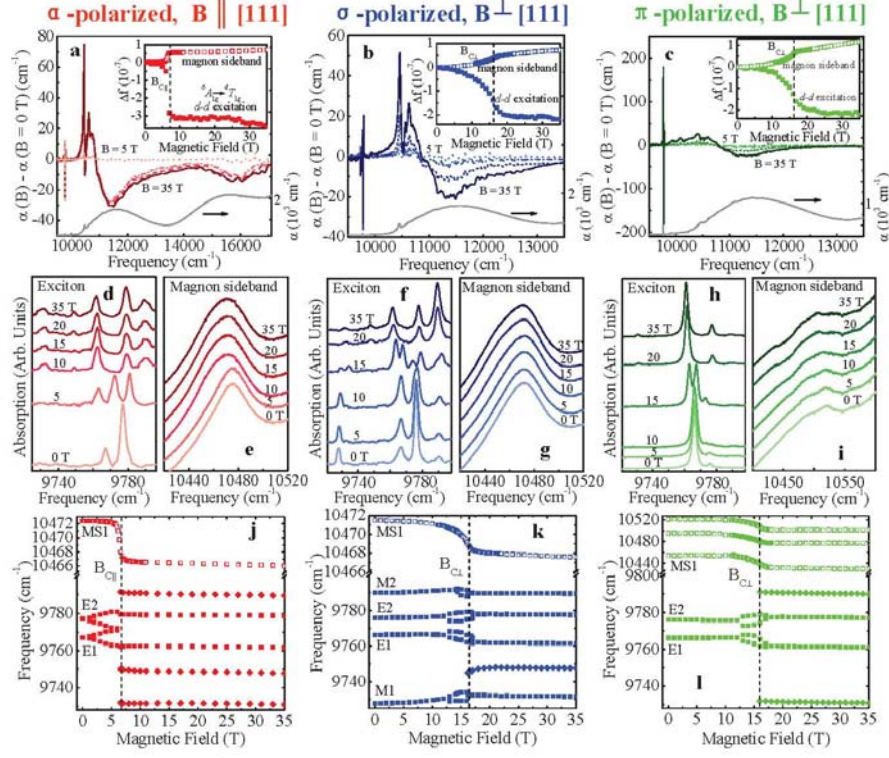


FIG. 2:

## Curriculum Vitae

NARA LEE

### Education

2005- Ph.D. May, 2012 Experimental Condensed Matter Physics  
Rutgers, the State University of New Jersey, New Brunswick, NJ  
Thesis Advisor : Prof. Sang-Wook Cheong

2002-2004 M.S. Theoretical Condensed Matter Physics  
Yonsei University, Seoul, Korea  
Thesis Advisor : Prof. Kyungsun Moon

1998-2002 B.S. Physics  
Yonsei University, Seoul, Korea

### Positions Held

2007-present Graduate Assistant  
Rutgers University Physics Department

2005-2007 Teaching Assistant  
Rutgers University Physics Department

2002-2004 Teaching Assistant  
Yonsei University Physics Department

### Publications

1. *Oxygen mediated magneto-electric coupling in LuMnO<sub>3</sub>*

P. Tong, Despina Louca, N. Lee, and S-W. Cheong

In preparation

2. *Tunable Large Ferroelectric Polarization in a Magnetism-Driven Ferroelectric*

N. Lee, Y. J. Choi, C. Veccini, L. C. Chapon, P. G. Radaelli, A. Bombardi, and S-W. Cheong

In preparation

3. *High-temperature superconductivity in a topological insulator*

Parisa Zareapour, Alex Hayat, Shu Yang F. Zhao, Anjan Reijnders, Mikhail Kreshchuk, Achint Jain, Daniel C. Kwok, Nara Lee, Sang-Wook Cheong, Zhijun Xu, Alina Yang, G. D. Gu, and Kenneth S. Burch

Submitted to *Science*

4. *Conduction of topologically-protected charged ferroelectric domain walls*

Weida Wu, Y. Horibe, N. Lee, S-W. Cheong and J. R. Guest  
Submitted to *Phys. Rev. Lett.*

5. *Magnetochromism in hematite: chameleonic rust*  
P. Chen, N. Lee, S. McGill, S-W. Cheong, and J. L. Musfeldt  
Submitted to *Phys. Rev. Lett.*

6. *Collective magnetism at ferroelectric vortex domain walls*  
Yanan Geng, N. Lee, Y. J. Choi, S-W. Cheong, and Weida Wu  
Submitted to *Nature Communications*.

7. *Direct observation of the proliferation of ferroelectric dislocation loops and vortex-antivortex pairs*  
S. C. Chae, N. Lee, Y. Horibe, M. Tanimura, S. Mori, B. Gao and S-W. Cheong  
Submitted to *Phys. Rev. Lett.*

8. *The topological  $Z_2 \times Z_3$  symmetry and  $Z_2$ -symmetry breaking in a ferroelectric*  
S. C. Chae, Y. Horibe, D. Y. Jeong, N. Lee, K. Iida, M. Tanimura and S-W. Cheong  
Submitted to *Nature Physics*

9. *Independent ferroelectric contributions and rare-earth-induced polarization reversal in multiferroic  $TbMn_2O_5$*   
N. Leo, D. Meier, R. V. Pisarev, N. Lee, S-W. Choeng, and M. Fiebig  
[arXiv:1112.1810v1](#)

10. *Piezoresponse force microscopy of domains and walls in multiferroic  $HoMnO_3$*   
Edward B. Lochocki, S. Park, Nara Lee, S-W. Cheong, and Weida Wu  
*Appl. Phys. Lett.* **99**, 232901 (2011)

11. *Mechanism of exchange striction of ferroelectricity in multiferroic orthorhombic  $HoMnO_3$  single crystals*  
N. Lee, Y. J. Choi, M. Ramazanoglu, W. Ratcliff II, V. Kiryukhin, and S-W. Cheong  
*Phys. Rev. B* **84**, 020101(R) (2011)

12. *Enhanced Superconducting  $T_c$  in the Immiscible System  $(La_{1.85}Sr_{0.15}CuO_4)_x(Lu_2Cu_2O_5)_{1-x}$*   
S. Park, C. L. Zhang, N. Lee, Y. J. Choi, S. Guha, and S-W. Cheong,  
*Phys. Rev. B* **83**, 220509(R) (2011)

13. *Fabrication and characterization of topological insulator  $Bi_2Se_3$  nanocrystals*  
S. Y. F. Zhao, C. Beekman, L. J. Sandilands, J. E. J. Bashucky, D. Kwok, N. Lee, A. D. LaForge, S-W. Cheong, and K. S. Burch  
*Appl. Phys. Lett.* **98**, 141911 (2011)

14. *Helical spin waves, magnetic order, and fluctuations in the langasite compound  $Ba_3NbFe_3Si_2O_{14}$*

C. Stock, L. C. Chapon, A. Schneidewing, Y. Su, P. G. Radaelli, D. F. McMorrow, A. Bombardi, N. Lee, and S-W. Cheong  
*Phys. Rev. B* **83**, 104426 (2011)

15. *Self-organization, condensation, and annihilation of topological vortices and antivortices in a multiferroic*

S. C. Chae, Y. Horibe, D. Y. Jeong, S. Rodan, N. Lee, and S-W. Cheong  
*PNAS* **107**, 21366 (2010)

16. *Cross-control of Magnetization and Polarization by Electric and Magnetic Fields with*

*Competing Multiferroic and Weak-ferromagnetic Phases.*

Y. J. Choi, C. L. Zhang, N. Lee, and S-W. Cheong,  
*Phys. Rev. Lett.* **105**, 097201 (2010). (Selected for a Viewpoint in *Physics*)

17. *Highly Aligned Epitaxial Nanorods with a Checkerboard Pattern in Oxide Films*

S. Park, Y. Horibe, T. Asada, L. S. Wielunski, N. Lee, P. L. Bonanno, S. M. O'Malley, A. A. Sirenko, A. Kazimirov, M. Tanimura, T. Gustafsson, and S-W. Cheong  
*Nano Lett.* **8**, 720 (2008)